Università degli Studi di Napoli
“Federico II”

Scuola Politecnica e delle Scienze di Base
Area Didattica di Scienze Matematiche Fisiche e Naturali

Dipartimento di Fisica “Ettore Pancini”

Laurea Magistrale in Fisica

Phase dynamics in spin-filter ferromagnetic Josephson Junctions

Relatori:

Prof. Francesco Tafuri
Dott. Davide Massarotti

Candidato:

Luigi Di Palma
Matricola N94000452

A.A. 2018/2019

Contents

List of Figures

Introduction

In a Josephson junction [1] (JJ) a supercurrent will flow between two superconductors separated by a barrier without any voltage drop fully depending on the phase difference between the macroscopic wave functions of the two superconducting condensates [1] [2] [3]. It is the only superconducting nonlinear circuital element [3] [4] and for these reasons, JJs are key structures for all low-power electronics applications including all types of superconducting qubits and a wide range of fundamental experiments [4] [5].
In the last years, a new class of Josephson devices, using ferromagnets as barriers, has been proposed. In these junctions, two forms of macroscopic order coexist (even if they are traditionally considered in conflict) generating unique properties for fundamental studies and applications.
In this work, we will consider a special type of S-F-S (superconductor-ferromagnet-superconductor) JJ, where the traditional metallic-like ferromagnet F is replaced by a tunnel-like ferro-insulator. In particular, our junction is composed of two superconducting electrodes of NbN separated by an insulator ferromagnetic barrier of GdN (SI$_f$S Josephson junctions). The properties of these devices vary as a function of the barrier thickness and we will focus on the study of the device with a barrier thickness of 3 nm. This is an intermediate regime that shows very remarkable properties, such as the presence of MQT (Macroscopic Quantum Tunneling) at low temperatures [6] and hints of triplet supercurrents [7] [8]. These characteristics are very interesting from a technological point of view and can be used in a wide range of low powers electronics including superconducting qubits.
All junctions have been fabricated at the Materials Science and Metallurgy Department of the University of Cambridge (UK).
A substantial part of my work is focused on the analysis of critical current fluctuations, the *switching current distributions* (SCD), that provides a powerful tool to investigate the electrodynamics properties of a Josephson junction and its interaction with the environment. I have compared the experimental switching current distributions with Monte Carlo simulations and these allow us to estimate some crucial parameters of the junction, such as

the damping factor Q and the capacitance C. The study that I have performed allows to investigate the behaviour of the device and it is the first step to develop real applications.
The thesis has been organized in the following way: in Chapter 1 I will give some hints on the quantum nature of the Josephson effect in junctions, analyzing the properties of devices with an insulator or metallic barrier, either if ferromagnetic or not. We will provide a simple model, the *RCSJ model* (Resistively and Capacitively Shunted Junction), that describes the electrodynamics of the majority of junctions in the presence of a direct current (DC).
In Chapter 2 we will extend the considerations on the I-V curves given in the first Chapter by including the effects of thermal fluctuations. We will investigate the switching current distributions and we will show how these curves can help us to provide a description of the electrodynamics parameters of the junction, such as capacitance and resistance.
In Chapter 3, we will describe the experimental set-up and the techniques used to perform low noise measurements.
The experimental data will be presented and discussed in Chapter 4. We will analyze the spin filtering properties of this junction starting from the $R(T)$ curve and the effects induced by the magnetic field. We will characterize the electrodynamics of the junction studying the switching current distributions and the interaction with the external environment.

Chapter 1

Introduction to superconductivity and Josephson effect

In this Chapter we will give some hints on superconductivity, providing the terminology that we will use. We will describe the main properties of a Josephson junction, starting from the well-known *SIS* junctions, where an insulator barrier is inserted between two superconducting electrodes.
We will investigate how these properties are modified in the presence of a ferromagnetic barrier, independently of being metallic or insulating, and which processes determine the electrodynamics of these junctions.

1.1 The phenomenon of superconductivity

Superconductivity is characterized by two fundamentals properties [9] [3]:

- The transition from finite resistivity to zero resistance below a threshold critical temperature T_c, which marks the transition from the normal to the superconducting state. As a consequence current can flow in a superconducting loop without any detectable decay below a threshold value $I_{critical}$ [1].

- The simultaneous change of magnetic susceptibility χ from a small positive paramagnetic value above T_c to $\chi = -1$, i.e. perfect diamagnetism below T_c. This effect was first observed by Meissner and Ochsenfeld in 1933, and is usually referred to *Meissner effect* [11]. The perfect diamagnetism occurs below a critical field $\vec{H}_c$.

[1] Measurements in a superconducting loop of Nb-Zr wires [10] showed that the current's decay time is about 100.000 years with a resistivity $\rho = 4 \cdot 10^{-25} \Omega \cdot m$

Superconductivity was discovered in 1911 by Kamerlingh Onnes [12]. In studying the electrical resistance of mercury at low temperatures, Kamerlingh Onnes found that, at about 4.2 K and in a range of about 0.01 K, the electrical resistance sharply dropped by several orders of magnitude to non-measurable values; cooling the metal below this critical temperature apparently led to a new resistance-less state, referred to as the superconducting state.
Since 1911, superconductivity has been found in more than 25 metallic elements and in more than one thousand alloys [11].

1.1.1 The London model

The first phenomenological model to explain the "superconductive state" was given by the London brothers (1935) [13]. Their theory assumes that in the superconducting state, the electronic density is made of two contributions, one from normal electrons and one from super-electrons which condense into a macroscopic quantum state [11].
Starting from the *Drude*'s model for a perfect conductor, they obtained two equations, *the London´s equations*, that describe both the perfect DC conductivity and the *Meissner effect*:

$$\frac{\partial \vec{J}}{\partial t} = \frac{n_s q^2}{m} \vec{E} \tag{1.1}$$

$$\nabla \times \vec{J} + \frac{n_s q^2}{mc} \vec{B} = 0 \tag{1.2}$$

as discussed in more detail in Appendix A. Here $\vec{J}$ is the superconducting current density, $\vec{E}$ and $\vec{B}$ are respectively the electric and magnetic fields within the superconductor, e is the charge of an electron, m is electron mass, and n_s is a phenomenological constant loosely associated with a number density of superconducting carriers [13].
In particular the eq. 1.2 defines a characteristic length :

$$\lambda_L = \sqrt{\frac{mc^2}{4\pi n_s e^2}} \tag{1.3}$$

along which the magnetic fields penetrates in the superconductor.

1.1.2 Ginzburg–Landau theory

The normal metal-superconductor phase transition can be well described and understood within the *Ginzburg-Landau* phenomenological theory, based on the general theory of second order transitions developed in 1930 by Landau. Ginzburg and Landau [14] introduced a macroscopic complex function, the *order parameter* $\psi(\vec{r},T) = |\psi(\vec{r})|e^{i\theta(\vec{r})}$, which characterizes the system:

$$\psi = \begin{cases} 0 \quad \text{for } T > T_c \\ \psi(\vec{r},T) \quad T < T_c \end{cases} \tag{1.4}$$

$\psi(\vec{r})$ at a given temperature T is related to the local number of the carriers in the superconductor by the relation:

$$n_{pairs} = |\psi(\vec{r})|^2 \tag{1.5}$$

The basic assumption of the Ginzburg-Landau theory is that the superconductor free energy density near the transition temperature can be expanded in the form [15] :

$$f_S(T,\psi,\vec{A}) = f_N(T) + \alpha(T)|\psi^2| + \frac{1}{2}\beta(T)|\psi^4|\frac{1}{2m^*}|(\vec{p} - \frac{e^*}{c}\vec{A})\psi(\vec{r})|^2 + \frac{\vec{B}^2}{8\pi} \tag{1.6}$$

where $f_N(T)$ is the free energy density in the normal phase ($\psi = 0$). The total free energy in the volume V of the sample is given by the space integral:

$$F_S(T) = \int_V f_S(T,\psi(\vec{r}),\vec{A}(\vec{r}))d\vec{r} \tag{1.7}$$

In eq. 1.6 the terms in $|\psi|^2$ and $|\psi|^4$ can be recognized as an expansion of the free energy up to second order in $\psi\psi^*$. The fourth term in the second member of 1.6 is written as if $\psi(\vec{r})$ represents a true quantum mechanical wavefunction for a particle of charge e^* and mass m^* in the presence of spatial gradients of the order parameter and magnetic fields.
We can obtain $\psi(\vec{r})$ minimizing the free energy $F_S(T)$ in respect to arbitrary variations of ψ^*. The variational calculation shows that the order parameter function ψ satisfies the *first Ginzburg-Landau* equation:

$$\frac{1}{2m^*}\left(\vec{p} - \frac{e^*}{c}\vec{A}\right)^2\psi(\vec{r}) + \beta|\psi(\vec{r})|^2\psi(\vec{r}) = -\alpha(T)\psi(\vec{r}) \tag{1.8}$$

Similarly, one can calculate the variation of free energy $F_S(T)$ with respect to arbitrary variations of the vector potential $\vec{A}$, obtaining an equation for the supercurrent density $\vec{J_s}$ [3]:

$$\vec{J_s}(\vec{r}) = |\psi(\vec{r})|^2\left(\frac{e^*\hbar}{m^*}\nabla\theta(\vec{r}) - \frac{e^{2*}}{m^*c}\vec{A}(\vec{r})\right) \tag{1.9}$$

This is known as the *second Ginzburg-Landau* equation: it shows that the phase $\theta(\vec{r})$ describes locally the motion of the center of mass of the superconductor's carrier.
For one dimensional model ($\vec{r} \equiv z$) and in the absence of the magnetic field $\vec{B}$, the eq. 1.9 can be written as:

$$\frac{\hbar^2}{2m^*}\frac{d^2\psi(z)}{dz^2} + \beta|\psi(\vec{r})|^2\psi(\vec{r}) = -\alpha(T)\psi(\vec{r}) \tag{1.10}$$

and the solution is:

$$\psi(z) = \psi_\infty tanh\bigg(\frac{z}{\sqrt(2)\xi_{GL}(T)}\bigg) \tag{1.11}$$

where $\xi_{GL} \equiv \hbar^2/2m^*|\alpha(T)|$ and ψ_∞ is the value of $\psi(\vec{r})$ in the superconductor bulk, in the absence of perturbation.
The coherence length ξ represents the range over which superconducting order is affected and specifically reduced by a local perturbation (for example the surface of superconductor) [2].

1.1.3 BCS Theory

A microscopic theory was developed first by Bardeen, Cooper and Schrieffer (BCS) in 1957 [17]. They supposed that in certain condition an effective attractive interaction between the electrons can be established. The electrons form pairs, called *Cooper pairs*, that have an effective mass $m^* = 2m_e$ and charge $e^* = 2e$. Because of this interaction, the ground state of the system changes such that it contains correlated pairs of electrons [9].
Different mechanisms have been proposed to explain the origin of superconductivity. In conventional superconductors, the attraction is generated by an indirect electron-electron interaction mediated by phonons, as suggested by Fröhlich [18]. This can be phenomenologically understood as follows: consider an electron moving in a lattice; as it is negatively charged, its movement exerts a force on the positively charged ions, which then slightly move towards the electron. Now the other electrons in the system may feel this movement, and follow the movement of the ions, i.e., towards the first electron. Thus, an effective attractive interaction is created, and with certain materials parameters and the average distance between the electrons, it can even beat the repulsive Coulomb interaction.
The first consequence of the presence of Cooper pairs is that the *normal Fermi sea* becomes unstable [19]. For the BCS theory all details are extensively given in textbooks. Here we limit to highlight a few details, which are

useful in the following. While in a normal metal small energy excitations are permitted, in a superconductor the spectrum has energy gap Δ, calculated in the appendix B (using the Bogoliubov-de Gennes equations):

$$E_k^0 = \sqrt{\left(\frac{\hbar^2 k^2}{2m}\right)^2 + \Delta^2} \tag{1.12}$$

where $\left(\frac{\hbar^2 k^2}{2m}\right)$ is the energy spectrum of a normal metal in *Free electron approximation*. Δ is a complex quantity and can be written as $\Delta = |\Delta|e^{i\theta}$.

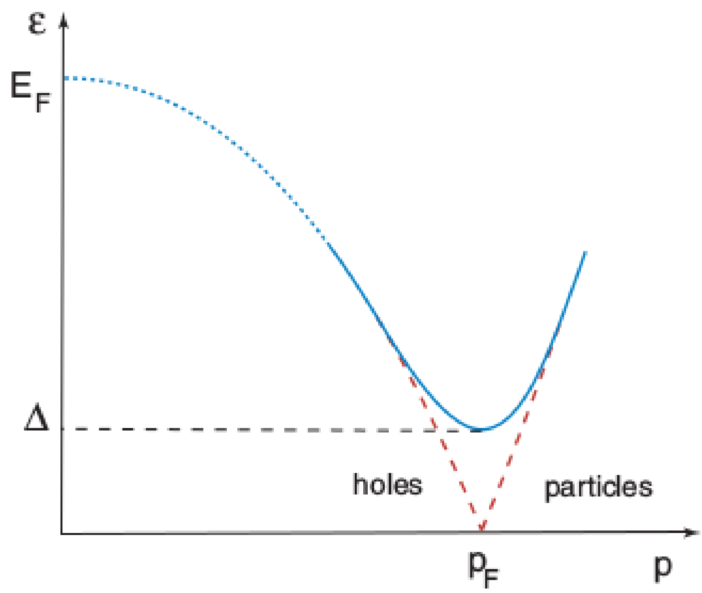

Figure 1.1: The BCS spectrum of excitations in a superconductor.

L.P.Gork'ov in 1959 showed that Δ is proportional to the order parameter ψ introduced in the Ginzburg Landau's theory [16].
The energy gap Δ decreases with increasing T, and is 0 above a critical temperature T_c: electrons with opposite spin become uncorrelated and the system behaves like a normal metal. The presence of the energy gap Δ has important consequence in the transport properties of the system: if the pairs have a center of mass $2\vec{q}$, such as when a current flows in the superconductor, Δ is in the form [2] [2]:

$$\Delta = |\Delta|e^{i2\vec{q}\vec{r}} \tag{1.13}$$

[2]We have seen in the previous section that the phase of the order parameter ψ is related to the motion of the Cooper pair 's center of mass

In this case the excitation energy is:

$$E_k = E_k^0 + \frac{\hbar^2}{m}\vec{k}\cdot\vec{q} \tag{1.14}$$

where $E_k^0 = \sqrt{\left(\frac{\hbar^2 k^2}{2m}\right)^2 + \Delta^2}$ is the excitation energy of the system in the absence of current. This equation shows that the gap goes to zero when:

$$q = \frac{m\Delta}{\hbar^2 k_f} \tag{1.15}$$

i.e there is a limit on the value of q and consequently, superconducting system cannot sustain a current up to $I_{critical}$.
The relation 1.14 is linear in $\vec{q}$: the *Landau superfluidity criterion* [20] ensure that the Copper pairs form a superfluid and the can flow with zero viscosity below $I_{critical}$.
It's important to define the *condensation energy of the system*, that is the difference in the energy of between the superconducting state and the normal state [2]. In the BCS theory at $T = 0$, this quantity is equal to:

$$\Delta E = E_N - E_S = \frac{1}{2}N(0)\Delta^2(T=0) \tag{1.16}$$

where $N(0)$ is the number of electrons at the Fermi energy $E_F \equiv 0$ The eq. 1.16 shows so that the superconducting state is energetically favorable respect to the normal metal state for $T < T_c$ and it's the key to explain the presence of a critical field H_c. When a magnetic field $\vec{H}$ is applied, the electrons spins tend to be aligned to $\vec{H}$: this mechanism breaks the pairs and the system goes to the normal state acquiring energy.
Then for the system is convenient screens the external field $\vec{H}$ with currents in order to have $\vec{B} = 0$ inside the superconductor, i.e perfect diamagnetism [11]. This is possible below a critical magnetic field H_c defined as :

$$\Delta E = E_N - E_S = \frac{H_c^2}{8\pi} \tag{1.17}$$

We can define a characteristic length

$$\xi_0 = \frac{1}{\pi}\frac{\hbar^2 k_F}{m\Delta_0} \tag{1.18}$$

called *BCS coherence length*: ξ_0 represents the average distance in real space between the two electrons of the Cooper pair [11]. At least, as pointed in appendix B, there is an uncertainty relation between the number of electrons that compose the system and the phase θ that characterizes the energy gap Δ [21]:

$$\Delta N \Delta\theta \leq 2\pi \tag{1.19}$$

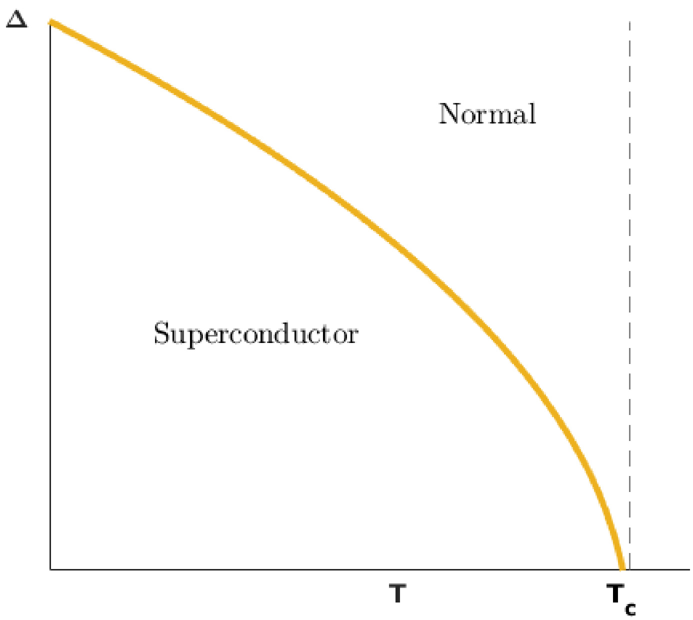

Figure 1.2: $\Delta(T)$ dependence in BCS theory

1.2 Josephson effect

In 1962 Brian D. Josephson predicted that a zero voltage electrical current could flow between two superconducting electrodes, separated by a thin insulator barrier [1]. This current is determined by the relation:

$$I_s = I_{critical} sin(\phi) \tag{1.20}$$

where $\phi \equiv \theta_R - \theta_L$ is the phase difference between the order parameters of the right (R) and left (L) superconducting electrodes and the *critical current* $I_{critical}$ is the maximum supercurrent that the junction can sustain.
He also predicted that if a voltage difference V is maintained across the junction the phase evolves with time according to the eq.:

$$d(\phi)/dt = 2eV/\hbar \tag{1.21}$$

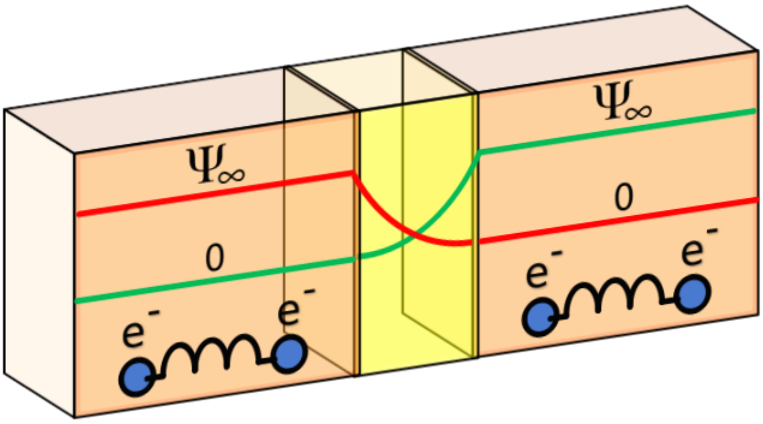

Figure 1.3: An example of a Josephson junction in BCS description. The red (green) line representes the order parameter Ψ of the left (right) superconducting electrode. As pointed above, Ψ_∞ is the bulk value of the order parameter that decreases to zero in the presence of the barrier

These effects, known as the dc and the ac Josephson effects respectively, have been fully confirmed by a great number of experiments. The first observation was made by Anderson and Rowell in 1963 [22].
The Josephson prediction was based on a microscopic theoretical analysis of the quantum mechanical tunneling of Cooper pairs through an insulator barrier layer, but it's now clear that the Josephson's effects are much more general and occur whenever two strongly superconducting electrodes are connected by a weak link [2]. To obtain the equations 1.20 and 1.21 one can consider a SIS junction (superconductor-insulating barrier-superconductor).
In an isolated superconductor, the minimum energy state would be one with N ($|\psi\rangle \equiv |N\rangle$) fixed electrons chosen so that the electron's charge cancels the positive ion cores's ones: this implies that the system is electrically neutral and have no electrostatic self-energy.
If a second isolated superconductor is present but far away from the first, it will also be in such a state with M electrons ($|\psi\rangle \equiv |M\rangle$) , with M chosen to preserve the electrical neutrality.
If the two electrodes are brought close enough together, the system could lower its energy by exchanging Coopers pairs[2]: in this case one can write the state of the system as :

$$|\psi\rangle = \sum_p c_p |N_L - p\rangle |N_R + p\rangle \tag{1.22}$$

The index p represents the number of pairs transferred from the left to the right. The Hamiltonian of the system is:

$$H = H_L + H_R + H_T \tag{1.23}$$

where H_R and H_L are the Hamiltonians of the right and left electrodes respectively and H_T describes the interaction between the two superconductors. We can adopt the simple model introduced by Anderson in 1963 [21].
We consider H such that the matrix element of H in the base $|N_L - p\rangle|N_R + p\rangle \equiv |N_L - p, N_R + p\rangle$ are:

$$\begin{aligned} \langle N_L - p', N_R + p'|H_R|N_L - p, N_R + p\rangle &= \delta_{p,p'} E_R \\ \langle N_L - p', N_R + p'|H_L|N_L - p, N_R + p\rangle &= \delta_{p,p'} E_L \\ \langle N_L - p', N_R + p'|H_T|N_L - p, N_R + p\rangle &= \begin{cases} -t & \text{for } p - p' = \pm 1 \\ 0 & \text{otherwise} \end{cases} \end{aligned} \tag{1.24}$$

where $t > 0$ is a real constant and represents the energy of binding.
This model is analogous to the *Tight Binding model* [11] for crystals.
The diagonalization of 1.23 shows that the ground state of the system is in the form:

$$|\psi\rangle = \int_0^{2\pi} e^{-iN\phi} \frac{d\theta}{2\pi} |\theta_L - \frac{\phi}{2}\rangle |\theta_R - \frac{\phi}{2}\rangle \tag{1.25}$$

with energy:

$$E = 2(E_0 - t cos(\phi)) \tag{1.26}$$

Here, N is the total number of the electrons of the system, θ_R and θ_L are the phase of the right and left superconducting electrode and ϕ is their difference. Eq. C.9 states that the system is the superposition of all possible states of phase with $\phi \equiv \theta_R - \theta_L$ fixed. Eq. C.2 shows that the system's energy is less than the energy of the superconductors isolated for $-\frac{\pi}{2} < \phi < \frac{\pi}{2}$.
The total current I passing through the junction can be calculated as:

$$I = \frac{d < \hat{N}_R >}{dt} - \frac{d < \hat{N}_L >}{dt} \tag{1.27}$$

where, using the *Ehrenfest theorem* :

$$\frac{d < \hat{N}_i >}{dt} =< [\hat{N}_i, \hat{H}] >= \frac{1}{\hbar} \partial_{\theta_i} E(\theta_i - \theta_L) \tag{1.28}$$

with $i \equiv R, L$. The last equality in the eq. 1.28 comes from the fact that in phase-space $\hat{N}$ is a differential operator.
Because $\frac{1}{\hbar}(\partial_{\theta_R} - \partial_{\theta_L}) = \frac{1}{\hbar}\partial_\phi$, considering 1.27 and 1.28, we get :

$$I = \frac{4t}{\hbar} \equiv I_{critical} sin(\phi) \tag{1.29}$$

Vinay Ambegaokar and Alexis Baratoff in 1964 [24] showed, starting from the microscopic model of the junction (see appendix C) in BCS approximation, that the $I_{critical}(T)$ has the form:

$$I_{critical}(T) = \frac{\pi}{2}\frac{\Delta(T)}{R_n} tanh\left(\frac{\Delta(T)}{2k_b T}\right) \tag{1.30}$$

known as AB relation. Here R_n is the normal resistance of the junction, as we will discuss in the next section. The eq. 1.30 shows that the critical current $I_{critical}$ depends on the energy gap $\Delta(T)$ and goes to 0 as $T \rightarrow T_c$.
Likewise eq. 1.21 can be calculate taking in number space (where $\theta_i \equiv \partial_{Ni}$) the difference between $< \frac{d\theta_L}{dt} > - < \frac{d\theta_R}{dt} >=< \frac{d\phi}{dt} >$. We have

$$i\hbar < \frac{d\theta_i}{dt} >=< [\theta_i, H] >= - < i\partial_{N_i} E >= -i\mu_i \Longrightarrow \tag{1.31}$$

$$< \frac{d\theta_L}{dt} > - < \frac{d\theta_R}{dt} >=< \frac{d\phi}{dt} >= -\frac{1}{\hbar}(\mu_L - \mu_R) = \frac{2eV(t)}{\hbar} \tag{1.32}$$

In the last equation, $\mu_{R,L}$ is the chemical potential of the right or the left superconducting electrodes and $V(t)$ is the potential's difference between the two sides of the Josephson junction.
Because the *Josephson effect* is a general property of weak links, one can analyze this effect using the order parameter $\psi(\vec{r})$ [2]. For example, Richard Feynman [25] proposed a phenomenological description of the *Josephson effect*, assuming that the superconducting condensates, with order parameters $\psi_1 = \sqrt{n_1}e^{i\phi_1}$ and $\psi_2 = \sqrt{n_2}e^{i\phi_2}$ overlap in the barrier and there is a coupling between the two systems.

1.2.1 Effect of magnetic field

Let's consider a junction with a magnetic field in the $\hat{y}-$ direction and the potential vector $\vec{A} \equiv |\vec{A}|\hat{x}$, as showed in fig. 1.4.
In each superconductors the *second Ginzburg-Landau equation* 1.9 is valid that could be written in the form:

$$\nabla\phi_{R,L} = \frac{2e}{\hbar c}\left(\frac{mc}{2e^2|\psi|^2}\vec{J}_s + \vec{A}\right) \tag{1.33}$$

Integrating the eq. 1.33 along the contours C_L and C_R one gets:

$$\phi_{Ra}(x) - \phi_{Rb}(x + dx) = \frac{2e}{\hbar c}\int_{C_R}(\vec{A} + \frac{mc}{2e^2|\psi|^2}\vec{J}_s\Big)\vec{dl} \tag{1.34}$$

$$\phi_{Lb}(x) - \phi_{La}(x + dx) = \frac{2e}{\hbar c}\int_{C_L}(\vec{A} + \frac{mc}{2e^2|\psi|^2}\vec{J}_s\Big)\vec{dl} \tag{1.35}$$

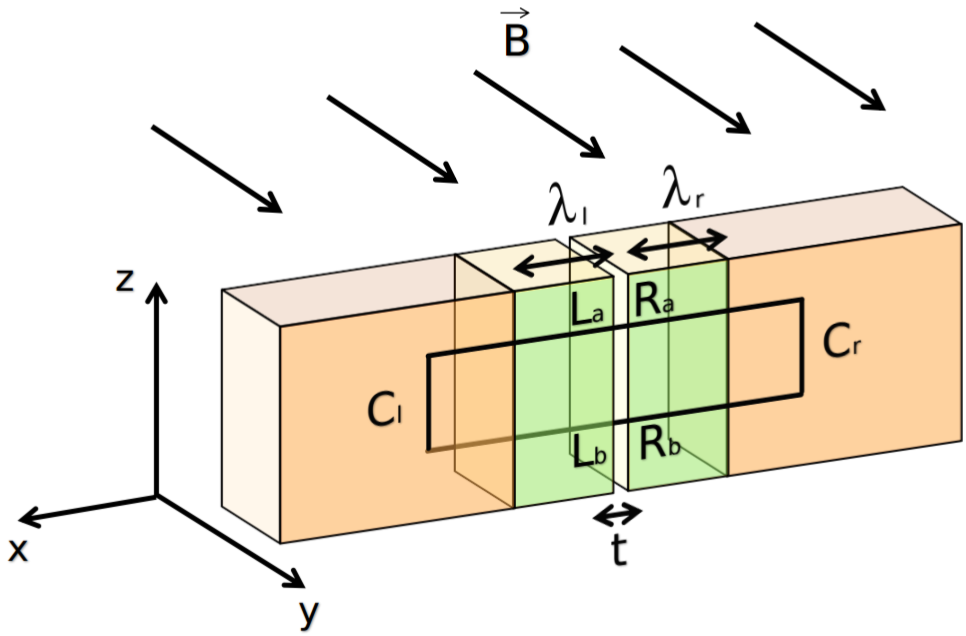

Figure 1.4: Contours of integration C_r and C_l used to derive the magnetic field dependence of the phase difference ϕ

Assuming that the thickness of the superconducting films are much larger than the London depths λ_L [4], one can extend the contours C_L and C_R outside the penetration region where the shielding current density $\vec{J_s}$ vanishes: far from the barrier $\psi(\vec{r})$ has the asymptotic value ψ_∞ (as discussed in the previous section) and the pair density $|\psi|^2$ is not reduced.
The portions of C_L and C_R in the penetration region can be chosen perpendicular to $\vec{J_s}$. In this way the second term in the integrals in eq. 1.34 and 1.35 doesn't give a contribution.
If the barrier thickness is small, one can write:

$$\phi(x + dx) - \phi(x) = \frac{2e}{\hbar c} \oint \vec{A}\vec{dl} = H_y(\lambda_R + \lambda_L + t)dx \tag{1.36}$$

The integration of this equation gives:

$$\phi = \frac{2e}{\hbar c} dH_y x + \phi_0 \tag{1.37}$$

where $d = (\lambda_R + \lambda_L + t)$ is the magnetic depth. In this way the supercurrent density can be expressed:

$$\vec{J_s}(\vec{r}) = \vec{J_1} sen(\frac{2e}{\hbar c} dH_y x + \phi_0) \tag{1.38}$$

This equation shows that the tunneling supercurrent is spatially modulated by the magnetic field. In the case of rectangular junctions, calculating the total current, one has:

$$I_1(\frac{\Phi}{\Phi_0}) = I_1 \left| \frac{sen(\pi \frac{\Phi}{\Phi_0})}{(\pi \frac{\Phi}{\Phi_0})} \right| \tag{1.39}$$

where $\Phi \equiv H_y L d$ is the magnetic flux through the junction and the $\Phi_0 \equiv \frac{hc}{2e}$ is the quantum flux. The maximum of the supercurrent exhibits a Fraunhofer pattern in function of the magnetic flux Φ [4]. The first observation of this effect was made by Rowell in 1963 [26].

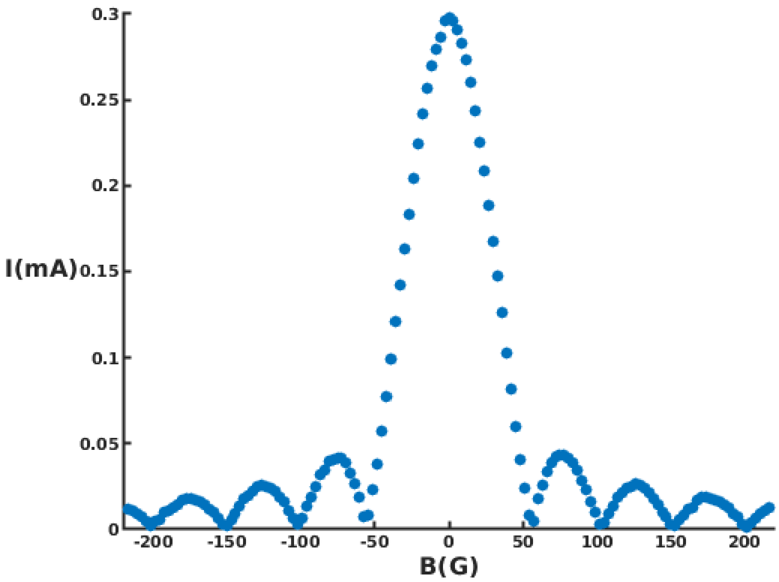

Figure 1.5: Fraunhofer pattern in conventional Nb/AlOx/Nb junction

1.3 Other type of weak links

In general other materials rather than insulator can be used as barriers in Josephson junctions: for example, we can employing semiconductors layers or metal.

In the last years, a new class of Josephson junction composed of ferromagnetic barriers between superconducting electrodes has been investigated [27]-[29]. The simultaneous presence of the macroscopic phase coherence of superconductors and the exchange interaction of ferromagnetic are of great interest in the study of fundamental questions on possible pairing states and for potential applications in a wide range of areas [7].

The existing literature focuses mostly on metallic super-conductor-ferromagnet-superconductor (*SFS junctions*) while the physics of ferromagnetic junctions with insulating barriers (*SI_FS junctions*), like the one in this work, is still relatively unexplored.
In this section we will be investigated the properties of the *SFS* and SI_fS junctions, analyzing the feature that a ferromagnetic barrier induces and comparing the difference between a metallic and an insulator weak link. This helps us to provide a full characterization of the NbN-GdN-NbN junction in the following sections.

1.3.1 SNS junctions

In an *SNS* device, the mechanism that leads the flow of a supercurrent through the barrier is quite different respect the case of tunnel junctions. Two main microscopic effects have to be considered: the *proximity effect* and *Andreev reflection* , which are in many ways related [9].
The *proximity effect* occurs when a layer of normal metal is interposed between two superconductors: a finite supercurrent can flow through such a junction. The effect lies in the fact that if a normal metal and a superconducting metal are brought into proper electric contact, some Cooper pairs will penetrate into the normal metal from the superconductor. Thus in the normal metals there arises a nonzero order parameter Δ, which exponentially decreases within the metal over a distance of the order of ξ_N. Hence, if the thickness of the normal interlayer is not very large, the order parameter will be different from zero throughout the normal metal, and a finite supercurrent may flow through the interlayer [5].
A microscopic argument to understand proximity effect has been given in terms of *Andreev reflection* [30].
Let's consider first a structure where a normal metal is brought in contact with a superconductor.
If an electron excitation, with energy lower than the gap ($E < \Delta$) hits the superconductor, it cannot enter because there are no available states for $E < \Delta$. However, if the contact is clean contact, the electron can't be reflected back [9].
What happens is an *Andreev reflection*: the electron reflects as a hole (an excitation below the Fermi sea with positive charge), and an extra Cooper pair (with a double negative charge) is formed inside the superconductor. This means that Andreev reflection carries charge current into or out of (in the inverse process, the hole is converted into an electron) the superconductor [9].
This process can be investigated using the *Bogoliubov-de Gennes equations.*

As pointed previously, in the metal, in which $\Delta(\vec{r}) = 0$, BdG eqs have the form B.16 with solution [9]:

$$\psi_{metal} = A\left[\begin{pmatrix} 1 \\ 0 \end{pmatrix} e^{ik_N^+ x} + r_{ee}\begin{pmatrix} 1 \\ 0 \end{pmatrix} e^{-ik_N^+ x} + r_{eh}\begin{pmatrix} 0 \\ 1 \end{pmatrix} e^{ik_N^- x}\right] \quad (1.40)$$

Here, A is a coefficient of normalization, while $|r_{ee}|^2$, $|r_{he}|^2$ represent the probability that the incident electron is reflected in an electron or a hole respectively. The expression 1.40 is obtained considering the *Free electrons approximation* for the metal, i.e $H_0 = p^2/2m$.
In the superconductor side, in BCS approximation, the solution is in the form:

$$\psi_{metal} = t_+\begin{pmatrix} u_0 e^{i\phi S} \\ v_0 \end{pmatrix} e^{ik_S^+ x} + t_-\begin{pmatrix} v_0 e^{i\phi S} \\ u_0 \end{pmatrix} e^{-ik_S^- x} \quad (1.41)$$

as discussed in Appendix C.
In the eq. 1.41 $|t_+|^2$ and $|t_-|^2$ are coefficients could be obtained requiring continuity of the functions and their derivatives at the surface points, for simplicity $x = 0$.
In the hypothesis of clean surface we have:

$$\begin{aligned} r_{ee} = 0, t_{+/-} = 0, |r_{eh}|^2 = 1 & \quad \text{for}|E| < \Delta \\ r_{ee} = t_- = 0, t_{+/-} = 0, |r_{eh}|^2 = \frac{E - \sqrt{E^2 - \Delta^2}}{E + \sqrt{E^2 - \Delta^2}} = 1 - |t_+|^2 & \quad \text{for}|E| > \Delta \end{aligned} \quad (1.42)$$

In the case of a *SNS* junction, the hole reflected from the left NS interface may find its way to the right interface, and reflect again into an electron state. Returning back to the left interface, this electron may again reflect, and so on. If the total phase acquired within a full cycle is a multiple of 2π, this results into a bound state.
One can study, as in the case of a single NS interface, the solution of eq. B.15 supposing the continuity of the functions and their derivatives at the interfaces points: this condition leads to bound states, known as *Andreev bound states*. The result of each cycle of Andreev reflections is a transfer of a Cooper pair between the superconductors:*Andreev bound states* can hence carry supercurrent. This is actually the mechanism of the Josephson effect through the normal metal.
Let us concentrate on the energy region $E < \Delta$. In the case short junction, i.e $L << \xi_0$ [5], the *Andreev bound states*:

$$E_\pm = \pm\Delta\, cos(\phi/2) \quad (1.43)$$

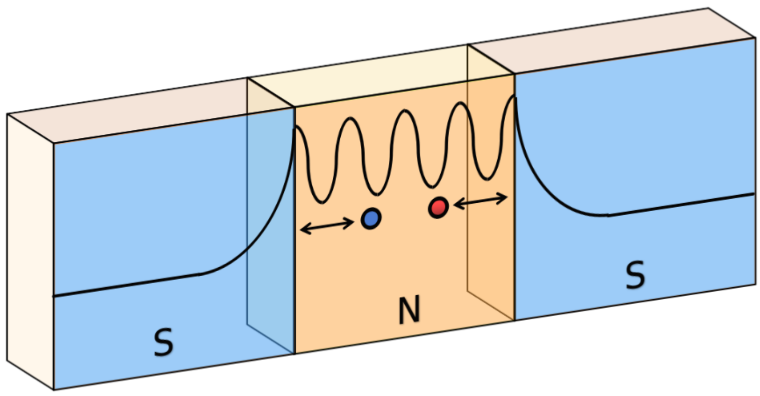

Figure 1.6: The Andreev bound state in *SNS* structure [9]. The black line represents the wavefunction of an electron responsible of Andreev reflections

In the same way, as shown in Section 1.2.1 , we can obtain the current from the total energy of the system :

$$I_S = \frac{2e}{\hbar} \sum_{\pm} \frac{\partial E_{\pm}}{\partial \phi} tanh\left(\frac{E_{\pm}}{2k_b T}\right) \tag{1.44}$$

In the case of presence some scattering at the interface, the bound state energies become

$$E_{\pm} = \pm\Delta\left(1 - \tau_p sin^2(\phi/2)\right) \tag{1.45}$$

and so, considering 1.44 we note that the dc Josephson relation $I_S = I_{critical} sin(\phi)$ is satisfied only in the case of small transmission or at high temperatures. In the other cases, the metallic barrier introduces the possibility of a new current-phase relation different respect to the conventional Josephson's one. In addition to the Andreev bound states, the *SNS* junction contains a continuum of states for energies $\Delta < |E|$ that don't contribute to the supercurrent [31] in the limit of short junctions.
In the long weak link limit, deviations from the sinusoidal trend in the supercurrent become sensitively stronger than in short weak links [32].
The normal branch is rather different respect the one observed in a tunnel junction: Andreev reflections produce electron-hole conversion at the interfaces in the high transparencies limit, contributing an excess current I compared with the normal state [33].

1.3.2 SFS junctions

Ferromagnetic materials are characterized by a spontaneous magnetization $\vec{M}$ due to the magnetic momentum orientation, which vanishes above a critical temperature known as *Curie temperature* T_{Curie}, at which the ferromagnet becomes a paramagnet. The spontaneous magnetization $\vec{M}(T)$ depends on the temperature.
The first phenomenological mechanism leading to ferromagnetism was proposed by Weiss in 1907 [34]. It is based on the assumption that the effective magnetic field acting on a magnetic moment is given by:

$$\vec{H}_{eff} = \vec{H} + \lambda\vec{M} \tag{1.46}$$

where $\vec{H}$ is the external magnetic field, λ is an appropriate constant, $\vec{M}$ is the magnetization, and the molecular field $\lambda\vec{M}$ provides the cooperative effect. Originally the Weiss constant λ was considered as a phenomenological constant that modulate the strength of interactions between the magnetic momentum of the system; the interpretation of λ in terms of microscopic quantum model appears later with the works of Heisenberg [11].
In the hypothesis of localized magnetic moments :

$$\vec{\mu} = -g\mu_B\vec{J} \tag{1.47}$$

the interaction energy of the magnetic moment with an applied magnetic field can be described by the Zeeman operator:

$$\mathcal{H} = -\vec{\mu}\cdot\vec{H} \tag{1.48}$$

Here, μ_B is the *Bohr magneton* and g is the gyromagnetic factor. Then, from the definition of magnetization $\vec{M}(T)$:

$$\vec{M}(T) = -\frac{1}{V}\nabla_{\vec{H}}F \tag{1.49}$$

where F is the free energy of the system and V is the ferromagnetic volume, one can show that in the *Weiss model*:

$$\vec{M}(T) = -\frac{N}{V}\mu_B\, tanh\left(\frac{\mu_B(\vec{H}+\lambda\vec{M})}{k_bT}\right) \tag{1.50}$$

The *Weiss model* explains importants property of a ferromagnetic such as the spontaneous magnetization and the presence of a critical temperature T_{Curie} [11].
The magnetization as a function of the magnetic field is hysteretic, as reported in fig. 1.7. In one dimensional approximation, initially the mag-

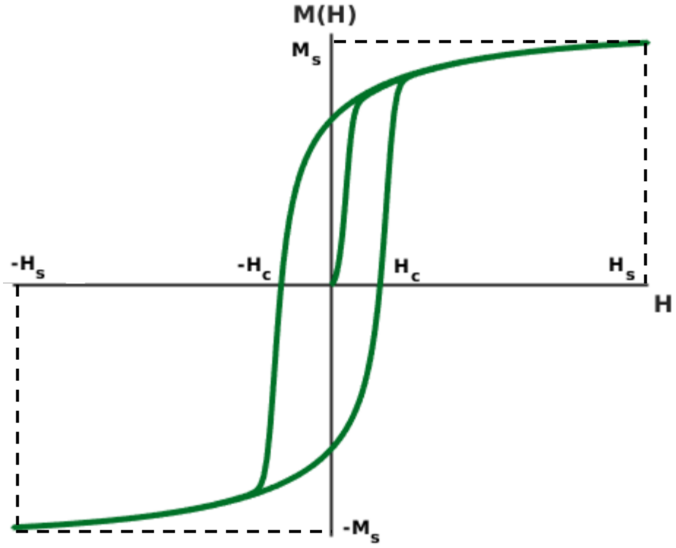

Figure 1.7: Magnetization hysteresis loop using *Matlab*. The plot is obtained making the path $H = 0 \rightarrow H_{max} \rightarrow -H_{max} \rightarrow H_{max}$

netization is zero in absence of magnetic fields. Turning the field on, the magnetization follows the first magnetization curve and saturates at the field H_s. Retracing back the magnetic field, the magnetization follows a different curve and becomes zero when the magnetic field reaches a value known as coercive field $-H_c$.
Then, it saturates at negative values in $-H_s$; returning to positive values of H, the magnetization is zero at H_c and reaches the asymptotic values at H_s. The final result is a hysteretic loop that depends on the direction of the spontaneous magnetization with respect to the crystallographic axes and gives a footprint of the crystallographic nature of the ferromagnet [35].

Fraunhofer pattern with a ferromagnetic barrier

One of the most important difference between a magnetic and a non-magnetic junction is the hysteretic nature of the *SFS* Fraunhofer pattern. Furthermore, the characteristic Fraunhofer pattern is horizontally shifted. These effects are due to the presence of the spontaneous magnetization M with a hysteretic behaviour. In fig. 1.8 we show for a fixed value of the magnetization M (in one-dimensional approximation) the corresponding value of

Ic(H), obtained starting from the equation:

$$I_{critical}(H) = I_{critical}^{max} \left| \frac{sin\left(\pi \frac{\phi_H + \phi_M}{\phi_0}\right)}{\pi \frac{\phi_H + \phi_M}{\phi_0}} \right| \tag{1.51}$$

Here ϕ_0 is the quantum flux, ϕ_H and ϕ_M are the fluxes due to the magnetic field and the magnetization of the barrier respectively and $I_{critical}^{max}$ is the critical current when the total flux is 0. Due to the hysteretic nature

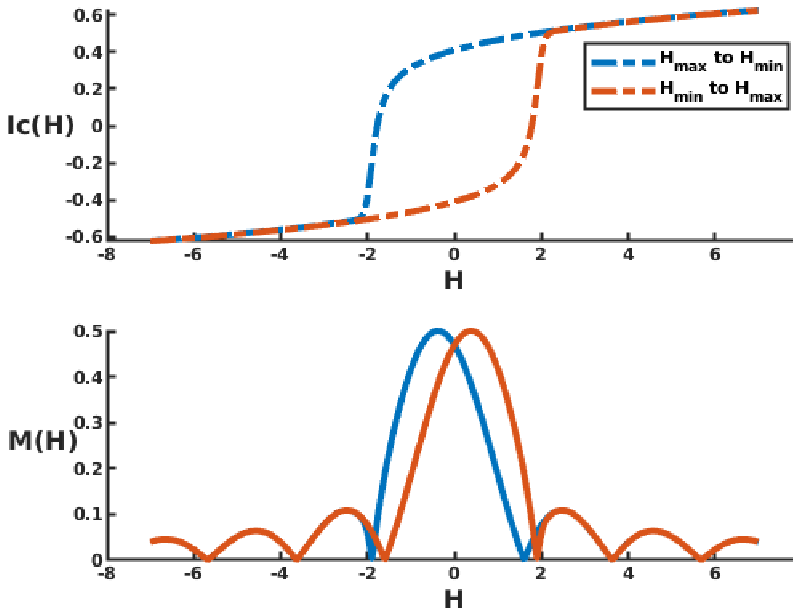

Figure 1.8: Frouhnofer pattern in a *SFS* junctions. The curves show that the hysteretic behaviour of the magnetization resulting in a hysteretic Frouhnofer pattern.

of the pattern, the junctions with ferromagnetic barrier are very interesting for engineering applications such as for the realization of cryogenic *RAM* [36].

Effects of ferromagnetic barrier on SNS transport properties

In normal metal barriers, due to the spin degeneracy of the energy levels, no spin effects occur with the *Andreev reflection*. However, in a junction with a metallic ferromagnet barrier there is an interaction that tries to align the electrons spin to $\vec{M}$: the electronic bands for up spins and down spins are shifted with respect to each other by an amount of $2E_{ex}$ as shown in fig 1.9.

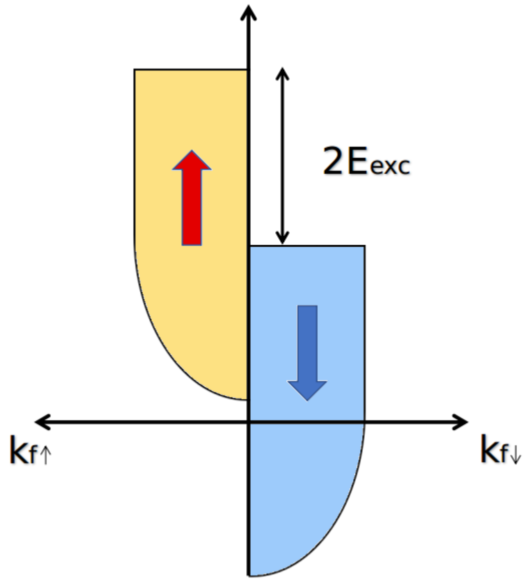

Figure 1.9: Energy band for spin up and down

In the *BCS* theory, the spins in a Cooper pair are antiparallel and so there is a competition between the formation of pairs and tendencies to align the spins to $\vec{M}$. This effect is known as *paramagnetic effect* and it's similar to what happens to Copper pair when a strong external magnetic field near H_c is applied [37]; now the role of the Zeeman interaction is played by the exchange interaction.
To model the spin splitting in the junction, one can consider the *Stoner model*[37], in which the motion of conduction electrons inside the ferromagnet can be described by an effective single-particle Hamiltonian with an exchange interaction while the influence of the magnetization of the ferromagnet on the orbital motion of conduction electrons is neglected [38]. Due to the paramagnetic effect and to the split of the energy band, a Cooper pair acquires a nonzero center of mass momentum $\vec{Q}$. To understand this, let's consider a Cooper pair, that in the BCS theory is in the singlet state:

$$|\psi\rangle = N\left(e^{i(\vec{k}_{F\uparrow}-\vec{k}_{F\downarrow})\vec{r}}|\uparrow\rangle|\downarrow\rangle - |\downarrow\rangle|\uparrow\rangle e^{-i(\vec{k}_{F\uparrow}-\vec{k}_{F\downarrow})\vec{r}}\right) \tag{1.52}$$

where N is a normalization factor.
As pointed above, the *paramagnetic effect* shifts the momenta at the Fermi energy E_F from $\vec{k}_F$ to: $\vec{k}_{F\uparrow} = \vec{k}_F + \vec{Q}/2$ for spin up and $\vec{k}_{F\downarrow} = \vec{k}_F - \vec{Q}/2$ for spin down.
Including this change in the eq.1.52 the resulting state is a mixture of singlet

$\Big(|\uparrow\rangle|\downarrow\rangle - |\downarrow\rangle|\uparrow\rangle\Big)$ and triplet spin states $\Big(|\uparrow\rangle|\downarrow\rangle + |\downarrow\rangle|\uparrow\rangle\Big)$ with zero spin projection on the direction of magnetization [37]:

$$\begin{gathered} e^{i(\vec{k}_{F\uparrow}-\vec{k}_{F\downarrow})\vec{r}}|\uparrow\rangle|\downarrow\rangle - |\downarrow\rangle|\uparrow\rangle e^{-i(\vec{k}_{F\uparrow}-\vec{k}_{F\downarrow})\vec{r}} \Longleftrightarrow \\ cos(\vec{Q}\vec{r})\Big(|\uparrow\rangle|\downarrow\rangle - |\downarrow\rangle|\uparrow\rangle\Big) + i\ sin(\vec{Q}\vec{r})\Big(|\uparrow\rangle|\downarrow\rangle + |\downarrow\rangle|\uparrow\rangle\Big) \end{gathered} \tag{1.53}$$

This state is called *FFLO* and takes the name from its discoverers Peter Fulde, Richard Ferrell, Anatoly Larkin and Yurii Ovchinnikov [39] [40].
Eq 1.53 shows that the Cooper pair's wavefunction in ferromagnetic barrier has an oscillatory behaviour over a length scale $\propto \sqrt{D/E_{ex}}$ [8], where D is the diffusion constant. This has important implication: combined with the Josephson effect it leads to the possibility of a so called π*-junction*, in which the two sides of the device has a phase difference of π. This effect depends on the length of the junction as shown in fig. 1.10 [37] and on temperature

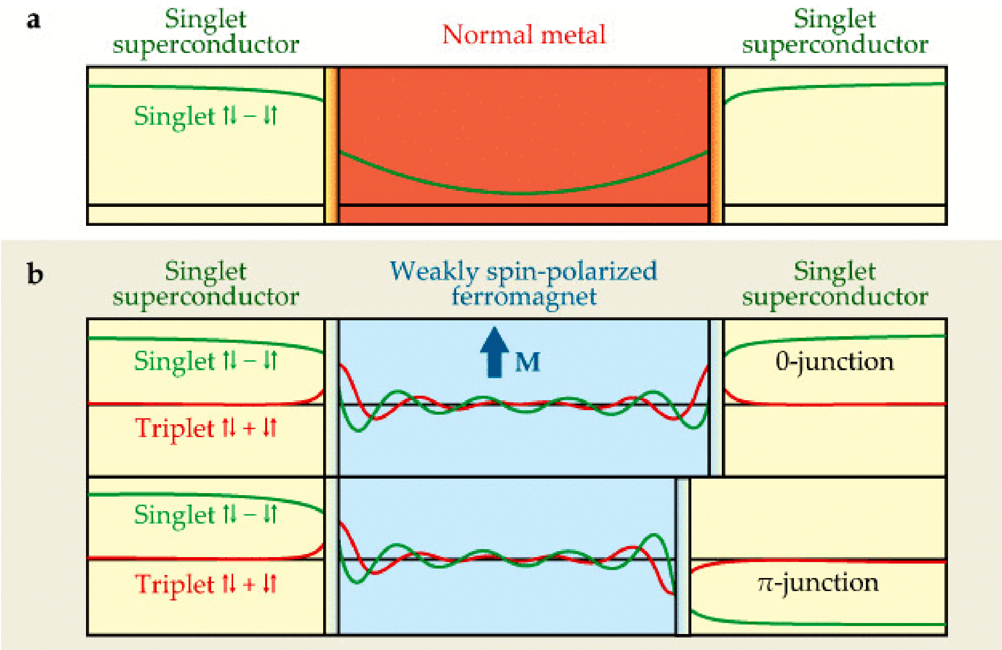

Figure 1.10: Comparison between *SNS* (a) and *SFS* (b) junction [37]. In figure (b) is also shown that different size of the ferromagnetic barrier can lead to a 0*-junction* or to π*-junction*

T. Fig. 1.11 (b) shows that the critical current density has a non-monotone behaviour in temperature with a cusp at the transition. This provides a useful experimental method to study the *0-*π *transition* [37].

Experimental confirms of the *FFLO state* have been found first by V. V. Ryazanov et al.(2001) [41] and T. Kontos et al. (2002) [42].

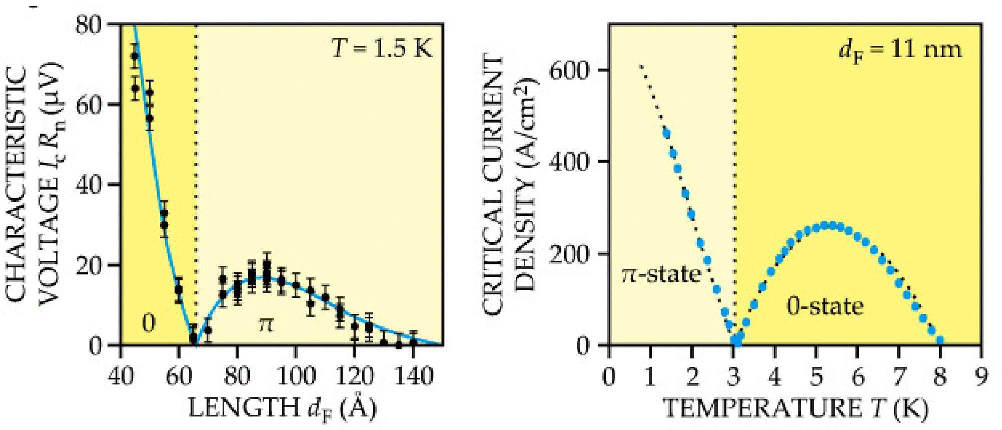

Figure 1.11: Evidence of $0-\pi$ transition varying T and the barrier length d_f [37]

1.3.3 SI$_f$S junctions

The NbN-GdN-NbN junction that we have studied in this work represents a new member of a class of SI$_f$S junctions, where I$_f$ insulator ferromagnetic barrier. Using a tunnel barrier e have most of the properties of a ferromagnetic barrier, with the advantage of the intrinsically non-dissipative nature of the tunneling process, useful to build low damping devices [43]. The presence of the ferromagnetic has two main effects: the junction acts like as **spin-filter** and **spin-mixing** as in *SFS* junction.

Spin-filtering In tunnel junctions, because there is a gap in the conduction band and valence band, the electron transport can only take place through quantum mechanical tunneling.
In WKB (Wentzel-Kramers-Brillouin) approximation [3] the conductance, in tunnel process, can be written as :

$$\sigma \propto e^{-\frac{2t}{\hbar}\sqrt{2mE}} \tag{1.54}$$

[3]The WKB approximation is a method for finding approximate solutions to linear differential equations with spatially varying coefficients. It assumed that the solution is in the form of an asymptotic series expansion $y(x) \sim \exp\left[\frac{1}{\delta}\sum_{n=0}^{\infty}\delta^n S_n(x)\right]$ with $\delta \to 0$. The coefficients $S_n(x)$ are obtained with the substitution of $y(x)$ in the differential equation.

where t is the barrier thickness, m is the effective mass of the electron and E is the effective barrier height. When the material goes through its ferromagnetic transition, however, the presence of exchange interactions leads to a spin asymmetry for the two spin channels: electrons of different spins, in fact, experience different barrier heights [8]:

$$\begin{cases} E_{\uparrow} = E_0 - \dfrac{h}{2} \\ E_{\downarrow} = E_0 - \dfrac{h}{2} \end{cases} \tag{1.55}$$

where h is the ferromagnet exchange field. In this way, we have different contribution to conductance σ for spins up and down [44]. Following Senapati et al. [8], one can define the *spin-filtering efficiency* P as:

$$P = \left| \frac{\sigma_{\uparrow} - \sigma_{\downarrow}}{\sigma_{\uparrow} + \sigma_{\downarrow}} \right| \tag{1.56}$$

In the *WKB* framework, one can show that this expression could be written [8]:

$$P \sim tanh\left(cosh^{-1}\left(\frac{R^*}{R} \right) \right) \tag{1.57}$$

where $R =$ is the resistance that the junction would have if it acts like a non-spin-filter junction and R^* is the effective one.
A first model of a SI$_f$S junction that considers the presence of *spin-filtering* and *spin-mixing* (that induces a non-zero Josephson triplet current) was developed by Bergeret et al. [45]. They modelled the tunnel junction as shown in fig. 1.12. The orange parts are the superconductor electrodes, the green parts are thin ferromagnetic layers with a finite exchange field acting on the spin of the conducting electrons and the blue part is a spin filter.
They assumed that the thickness of the barrier is smaller than the coherence length ξ_0 of the superconductors.
The Hamiltonian of the system can be written in the form:

$$H = H_R + H_L + H_T \tag{1.58}$$

where $H_{L,R}$ are BCS Hamiltonian of the left and right electrodes. H_T is composed of two terms: one that describes the tunnel in a conventional insulating barrier and another one that takes in account the effect of $\vec{M}$ on the spins tunneling.
They calculated the current through the junction like in the eq. D.4

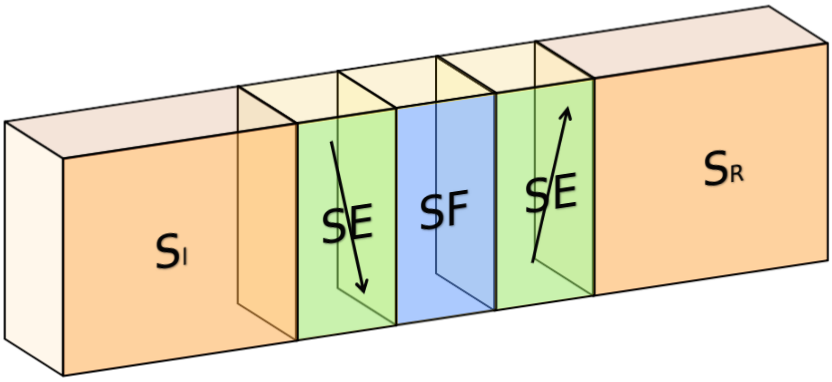

Figure 1.12: In the Bergeret et al. model [45] the device is represented as composed by five parts. The superconducting electrodes are painted in orange while the barrier has three elements. The blue region represents the spin-filter barrier while the green regions are layers with a finite exchange field pointing in an arbitrary direction.

In the case in which $\Delta = \Delta_R = \Delta_L$, Bergeret et al. showed that the characteristic voltage of the junction is in the form:

$$I_{critical} R_N = \frac{2\pi T}{e} \sum_{\omega_N > 0} r\left(f_s^2 + f_t^2 cos(\alpha) sin(\beta) \right) + f_t^2 sin(\alpha) sin(\beta) \qquad (1.59)$$

where:

- r is a parameter linked to the spin-filtering efficiency P

  $$r = \sqrt{1 - P^2} \qquad (1.60)$$

  So that for $r = 0$ we have the limit case of a fully polarized barrier and for $r = 1$ a non-magnetic barrier

- α and β are the angles between the exchange field of the L and R electrodes with respect to the z axis

- f_s and f_t are respectively are the amplitude of the singlet and triplet component. The are related to the anomalous Green function in frequency domain:

  $$f_{\pm} = \frac{\Delta}{\sqrt{\Delta^2 + (\omega_N \pm ih)^2}} \qquad (1.61)$$

  by symmetric and asymmetric combination.

If $h = 0$ the expression 1.59 reproduce the well-known Ambegaokar-Baratoff (AB) 1.30 formula for the critical current multiplied by a factor $r < 1$.

1.4 RSCJ Model

As we have previously mentioned, the Josephson phenomena occur in various kinds of structure and the different properties of these systems determine different I-V characteristics [4]. The Josephson systems, then, are important example in which the microscopic transport features can be investigated by measurements of macroscopic quantities, such as the current and voltage [4]. Many properties of the I-V characteristics in DC current can be studied considering the Josephson junction as equivalent circuit balanced by the equation:

$$I_{dc} = C\frac{dV(t)}{dt} + \sigma V(t) + I_{critical} sin\phi((t)) \tag{1.62}$$

where the term $C\frac{dV}{dt}$ is the displacement current through the barrier with a capacity C and $\sigma = 1/R$ is the conductance of the device. Here R may contain frequency-dependent contributions from the bias circuitry in addition to the intrinsic values of the junction [46] as we will discuss in the following Chapters. This model takes the name of *RCSJ model* (*Resistively and Capacitively Shunted Junction*) and can be obtained formally starting from the microscopic model of a Josephson junction as showed in appendix D.

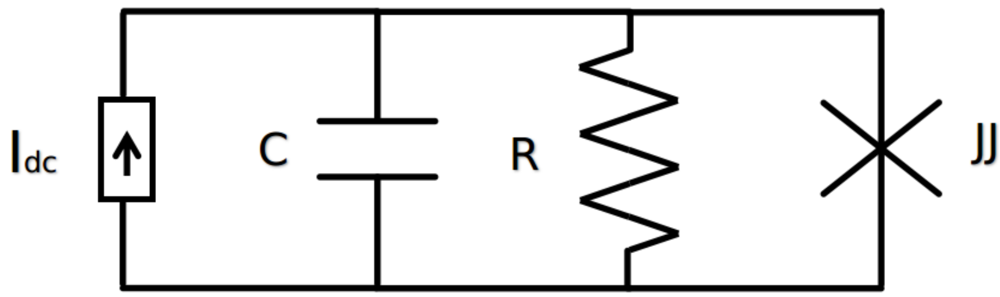

Figure 1.13: Equivalent circuit of a Josephson junction device

The eq. 1.62 is valid when the phase difference ϕ across the weak link has no spatial variations.
Using the *second Josephson equation* 1.21 , the expression 1.62 can be transformed in an equation for the phase ϕ:

$$I_{dc} = \frac{\hbar}{2e}C\frac{d^2\phi}{dt^2} + \frac{\hbar}{2e}\frac{1}{R}\frac{d\phi}{dt} + I_{critical} sin\phi((t)) \tag{1.63}$$

Eq. 1.63 can be considered as the motion's equation of a particle in a *tilted washboard potential* (see fig. 1.14) :

$$U(\phi) = -\frac{\hbar}{2e} I_{critical} cos(\phi) - \frac{\hbar}{2e} I_{dc}\phi \tag{1.64}$$

and subjected to a viscous force. In the case of $I_{dc} = 0$, for ϕ near the

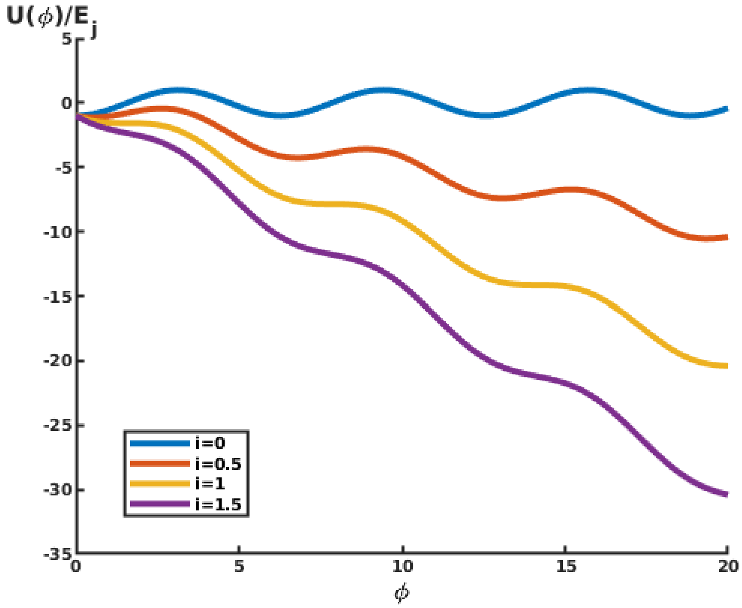

Figure 1.14: Washboard potential for the phase particle for different value of i. U(ϕ) is normalized on $E_j = \hbar I_{critical}/2e$

minimum, the eq.1.63 becomes:

$$\frac{d^2\phi}{dt^2} + \left(\frac{2e}{\hbar}\frac{I_{critical}}{C}\right)\phi = 0 \tag{1.65}$$

and the phase particle oscillates around the minimum of the potential well with the *plasma frequency*

$$\omega_p = \sqrt{\frac{2e}{\hbar}\frac{I_{critical}}{C}} \tag{1.66}$$

While the bias current I_{dc} is smaller than the critical current $I_{critical}$, the potential is tilted respect to the case in which $I_{dc} = 0$ but not enough to allow the particle to roll down the potential: the motion consists in oscillations around one of the minimum of potential. In this case:

$$\frac{d<\phi>}{dt} = 0 \Longrightarrow V = 0 \tag{1.67}$$

If $I_{dc} > I_{critical}$ the phase particle escapes from the washboard potential minimum and a finite V appears [2].
To study the property of eq. 1.63, it's convenient to introduce the variable [48]:

$$\begin{aligned} \tau &= \omega_j t \\ \frac{1}{Q} &= \frac{1}{\omega_j}\frac{1}{RC} \\ \omega_j &= \left(\frac{2e}{\hbar}\frac{I_{critical}}{C}\right)^{\frac{1}{2}} \\ i &= \frac{I_{dc}}{I_{critical}} \\ \eta &= \frac{1}{Q}\frac{dV}{d\tau} = \frac{V}{RI} \end{aligned} \tag{1.68}$$

where:

- i is the normalized current
- ω_j is the plasma frequency
- Q is the quality or damping factor of the junction that characterizes the strength of friction in the phase particle's motion
- η is the normalized voltage

In this way eq 1.63 becomes:

$$i = \frac{d^2\phi}{d\tau^2} + \frac{1}{Q}\frac{d\phi}{d\tau} + sin(\phi) \tag{1.69}$$

A very useful technique for a qualitative understanding of the behaviour of a Josephson system and the I-V characteristic is provided by the study of the eq. 1.69 in an appropriate phase space [48].
First, let's define the variable:

$$\frac{d\phi}{d\tau} \equiv Z \tag{1.70}$$

so that the eq. 1.69 can be transformed in an equivalent system of differential equations of the first order:

$$\begin{cases} \dfrac{d\phi}{d\tau} = Z \\ \dfrac{dZ}{d\tau} = i - \dfrac{1}{Q}\dfrac{d\phi}{d\tau} - sin(\phi) \end{cases} \tag{1.71}$$

The state of the system is represented at any time by a specific point in the Z, ϕ plane. As τ varies the point describes a trajectory in that plane depending on the initial conditions: for a fixed value of parameters i and Q, the system is represented by a set of possible paths.
A closed curve in the Z, ϕ plane corresponds to a periodic solution, while an equilibrium point has $d\phi/dt = 0$ and $dZ/dt = 0$.
Now ϕ appears in the sine function so that $\tilde{\phi} = \phi + 2n\pi$, with $n \in \mathbb{Z}$. So the phase space is a *cylindrical variety* [4]. There are two kinds of closed paths

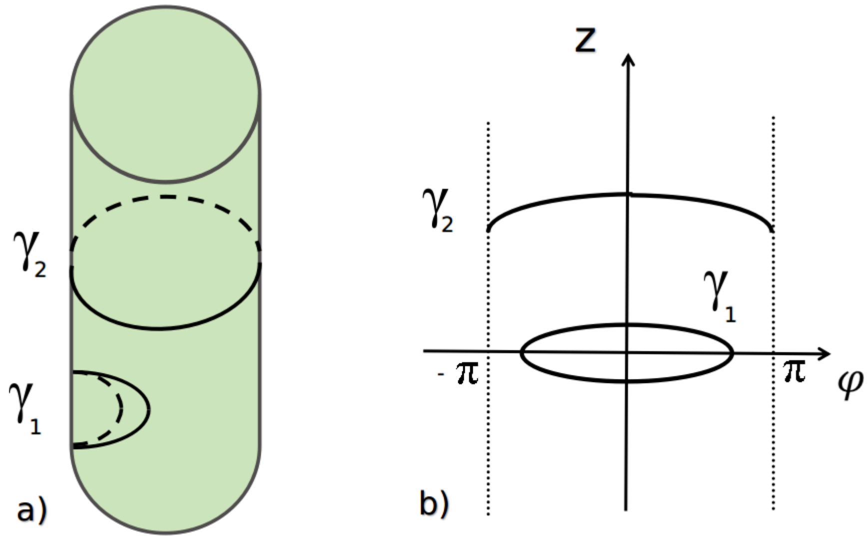

Figure 1.15: Representation of curves of first (γ_1) and second (γ_2) kind in a (a)Cylindrical phase space and (b) in is projection on the plane $z = const$

(corresponding to a two different solutions of the eq. 1.69 in that space):

- *closed paths of first kind* that encircle an equilibrium point. These correspond to oscillatory motion of the phase particle around the potential minimum. It can be shown that these types of solution have the mean value of the voltage equal to zero.

- *closed paths of the second kind* which go around the cylinder without encircling an equilibrium point. These describe the state of running of the phase particle down the potential.

As pointed by Stewart [49], in terms of parameters I and Q the solutions of the motion in the phase space can be summarized as follows:

- for $i > 1(I_{dc} > I_{critical})$ there is only a periodic solution of the second type with $< Z(\tau) > \neq 0$. Therefore the junction is in the finite voltage state.

- for $i < 1$ the behaviour depends on the particular value of Q. In a plane $i - Q$, a curve $i(Q)$ can be identified that divides the plane in two regions: in the first region there is a solution of the *first type*, in the second region coexists two solutions, one of the *first type* and one of the *second*. Therefore the states of zero and finite voltage are both possibles and the junction is in either one depending on the initial conditions. For example, let's consider fig. 1.16. The curve (a) is obtained placing $Q = 0.9$ while in the figure (b) $Q = 5$. In the first case only for $i > 1$ we have a finite voltage; in the case (b) we have also a finite voltage branch for $i < 1$.

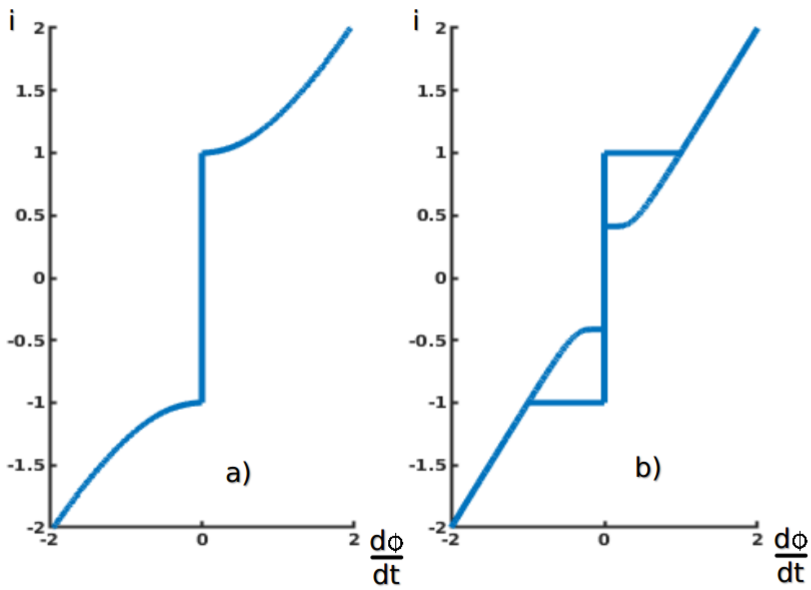

Figure 1.16: Example of (a) overdamped and (b) underdamped JJ. In figure (a) the damping factor $Q = 0.9$ while in the figure (b) $Q = 5$.

The dependence of the curve $i(Q)$ was evaluated numerically by several authors [49] [50] [51] . For Q greater than about 3 an excellent estimate of i is given by [49]:

$$i \simeq \frac{4}{\pi Q} \tag{1.72}$$

We can distiguish two main class of junctions depending on the value of the damping factor Q.

Overdamped Junctions

This correspond to the case in which the product $\omega_p C$ is small compared to the conductance $\sigma \equiv 1/R$, i.e $Q \leq 1$. This implies that the viscous drags dominates inertia [2]. The eq. 1.69 reduces to:

$$i = \frac{1}{Q}\frac{d\phi}{d\tau} + sin(\phi) \tag{1.73}$$

and has the analytical solution

$$\phi(\tau) = 2tan^{-1}\left[\left(\frac{i^2-1}{i^2}\right)^{-1/2} tan\left(\frac{\pi\tau}{T}\right) - i\right] \tag{1.74}$$

where T is the period.
From the 1.21, the DC voltage is proportional to the time average of $d\phi \ dt$, and the relation between the averaged voltage and the current could be shown to be:

$$\bar{V} = RI_{critical}\sqrt{i^2-1} \tag{1.75}$$

As shown in fig. 1.16 (a) as long as $i < 1$ ($I_{critical} < I_{dc}$) the averaged voltage is zero. A further increase of the driving current I_{dc} brings the junction to a finite voltage states without any overlap between the two possible states. Typical overdampend junctions are the ones with a metallic barrier, such as in SNS and SFS devices. The presence of a metallic barrier implies that the capacity C tends to 0: consequently $Q << 1$ and in these devices the IV characteristic is non hysteretic.

Underdamped Junctions

When C is large enough so that $Q > 1$, the I-V curves becomes hysteretic. The equation 1.69 is not analytically solvable. The fig. 1.16 (b) shows the I-V curve obtained numerically. Starting from $i = 0$ and $V = 0$ and increasing the current, no voltage drop develops until $i = 1$ is reached. At this point a switch to the finite voltage state occurs.
Reducing the current, the junction stays in the finite voltage state until i is reduced to the value $i(Q)$; then the system reaches the superconducting state. Typical underdamped junctions are the ones with an insulator barrier such as the SIS and SI_fS devices.

1.5 Quantum phenomena in Josephson junction

In the preceding discussions we have treated the Josephson Junction as a purely classical system, in which the phase difference ϕ across the junction and the charge $Q = CV$ were treated as classical variables which could be

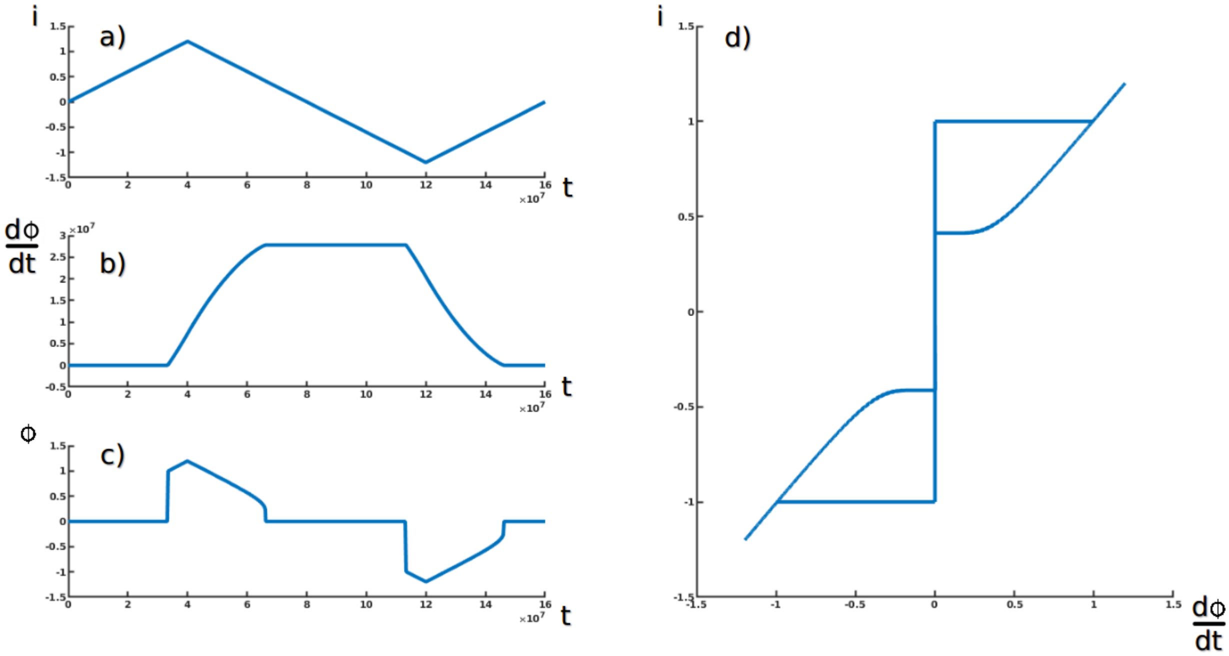

Figure 1.17: Underdamped junction with Q=5. This figure has been obtained solving 1.69 using a C algorithm. In the subplot (a), (b) and (c) we have the behaviour of i, $d\phi/dt$ and ϕ obtained in the function of t. In fig (d) we have represented i vs $d\phi/dt$

specified to arbitrary precision [2].
This is valid only if $E_j \gg E_C$, with $E_j = \hbar/2e$, when ϕ is well defined and Q has large fluctuations and the Josephson nature of the junction dominates [52]. When $E_j \ll E_C$, N is well defined, and ϕ has large quantum fluctuations; therefore, the charging nature of the capacitor is dominating. In this situation the junction is known as a Cooper-pair box [53].
Macroscopic quantum phenomenon can be observed in Josephson junctions if two conditions are satisfied. First the Coulomb charging energy for one electron $e^2/2C$ should be larger than temperature to avoid thermal smearing of the charge states of the superconducting island.
Second the tunnel resistance should be large enough to avoid averaging out by quantum fluctuations in the particle number. To be observable, the charging energy $e^2/2C$ must exceed the quantum uncertainty in energy $\hbar/\Delta t \sim \hbar/RC$ associated with the finite lifetime of the charge on the capacitor. Equating $e^2/2C$ to $\hbar/RC$ we find that the capacitance drops out and the condition becomes $R > R_0$ where R_0 is the resistance quantum $R_0 = h/2e^2 \simeq 12k\Omega$

[2].
When all these conditions are satisfied a fully quantum-mechanical description of the junction dynamics is necessary: we have to determine the form of the Hamiltonian.
In the classical regime, when $E_j \gg E_C$, we have schematized the dynamics of the system as the motion of a phase particle in a washboard potential 1.64. The Hamiltonian of this system could be written in the form:

$$H = \frac{Q^2}{2C} - E_j cos(\phi) - \frac{\hbar}{2e} I_b \phi \tag{1.76}$$

where I_b is the bias current. The quantum mechanics Hamiltonian can be obtained replacing the classical variables Q and ϕ with the operator $\hat{Q}$ and $\hat{\phi}$, that have in the phase space the representation [9]:

$$\hat{Q} \equiv 2e\frac{\partial}{\partial \phi} \text{ and } \hat{\phi} \equiv \phi \tag{1.77}$$

Chapter 2

Thermal effects on a Josephson junction

In the first Chapter we have reviewed the fundamentals properties of a Josephson junction, starting from the well known SIS devices to the non-conventional SI_fS ones. These considerations hold as long as the effects due to thermal fluctuations are negligible: when thermally activated processes are taken into account, the dynamics of the junctions can be strongly modified from the simple picture described in the first Chapter [2].
Experimentally, we can study the influence of thermal effects on the junction through the measurement of both I-V curves and switching current distributions (SCD) as a function of T. SCD help us to provide a full characterization of the electrodynamic parameters of the junction, such as the damping factor Q, and the incidence of the various processes responsible for the phase dynamics of the system [54].
In this Chapter we describe the effects of thermal fluctuations and their influence, strongly dependent on the damping factor Q. We focus our analysis on systems in the moderately damping regime, i.e $1 < Q < 10$, because our NbN-GdN-NdN junction, as we will demonstrate in the following Chapters, falls in this category of junctions.
These considerations will be very useful to provide a characterization of the non-conventional NbN-GdN-NbN system in the following Chapters.
The study of thermal effects on Josephson systems is of great importance for a comprehension of the interaction between the environment and the junction, aspects that we have to consider to develop technological devices [53].

2.1 Influence of thermal noise on the I-V characteristics

The effects of thermal fluctuations can be introduced by adding a Johnson noise current term to the bias current in the eq. 1.63. This represents the noise due to resistive flow of quasiparticle current described by the term V/R in the *RCSJ* model.
This term introduces a small stochastic perturbation in the motion of the phase particle and the problem is thus entirely equivalent to the Brownian motion in the washboard potential 1.64 [54].
The Johnson current noise can be represented by a Gaussian signal with mean and autocorrelation given by [55]:

$$< I(t) >= 0 \text{ and } < I(t+\tau)I(t) >= \frac{2k_bT}{R}\delta(\tau) \tag{2.1}$$

For stationary processes, it isn't important at which points in time we begin our observation; in other words, there is *translational symmetry in time* [56].
The first equation reflects the fact that phase particle motion is Brownian.
The second equation shows that $I(t)$ is independent of $I(t^*)$ for $t \neq t^*$. The *central limit theory* implies that the probability distribution for $I(t)$ is a Gaussian with a width determined by $A \equiv 2k_bT/R$ [56]
Eq. 2 in 2.1 can be determined considering the *Wiener-Khintchine* theorem:

$$< I(t+\tau)I(t) >= \int_0^\infty d\omega P(\omega) cos(\omega\tau) \tag{2.2}$$

This theorem states that the power spectrum and the correlation function are reciprocal Fourier transforms of each other. [4] In the case of quasiparticle current, the power spectrum is given by [57] :

$$P(\omega) = \frac{|e|}{\pi} I\left(\frac{\hbar\omega}{|e|}\right) coth\left(\frac{\hbar\omega}{2K_bT}\right) \tag{2.3}$$

that reduces to the expression:

$$P(\omega) = \frac{2k_bT}{\pi R} \tag{2.4}$$

in the hypothesis of $T >> \hbar\omega/k_b$ and frequency independent conductance.
It's important to note that eq. 2.4 is independent of $\hbar$: this testifies the fact that the fluctuations are now classical and P is just the Johnson noise associated with the resistor R.
Inserting eq. 2.4 in 2.2 one obtains the expression 2 in eq. 2.1
The Johnson current can be well approximated by a sequence of independent pulses of random sign and magnitude as shown in fig. 2.1.

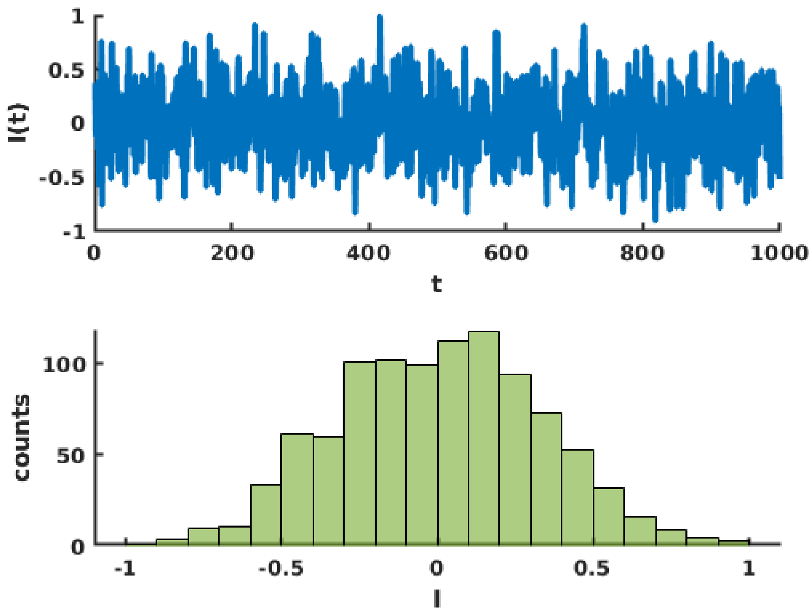

Figure 2.1: Simulation of Johnson noise. The figure (a) shows the behaviour of I(t) starting from eqs. 2.2. In figure (b) the extracted values I obtained with a Gaussian random generator have been collected in histograms

2.1.1 I-V curves

Including the Johnson noise term we can rewrite the eq. 1.69 [58]:

$$i = \frac{d^2\phi}{d\tau^2} + \frac{1}{Q}\frac{d\phi}{d\tau} + sin(\phi) + i_n \tag{2.5}$$

where i_n is the normalized Johnson current with autocorrelation:

$$< i(t+\tau)i(t) >= 2\pi k_B T/QI_{co}\Phi_0\delta(\tau) \tag{2.6}$$

To study the effects of thermal noise we are going to focus on *moderately-damped* regime (i.e $1 < Q < 10$). The underdamped and overdamped case could be considered as limits of the moderately damping case [55], as we will show in the following considerations. In figure 2.2 we have shown four I-V curves, computed at different normalized temperatures $\Gamma \equiv 2k_bT/\Phi_0 I_{critical}Q$ with Q=3. Each of these curves illustrates a qualitatively different situation. In the absence of noise, $\Gamma = 0$, the zero-voltage state or *0 state* is stable at all bias levels less than the critical current ($i_{s0} = 1$) and the voltage state or *1 state* is stable at all bias levels greater than a minimum value designated i_{r0}.
For $\Gamma = 0.2$, the bias i_s at which the junction switches from the 0 state to the

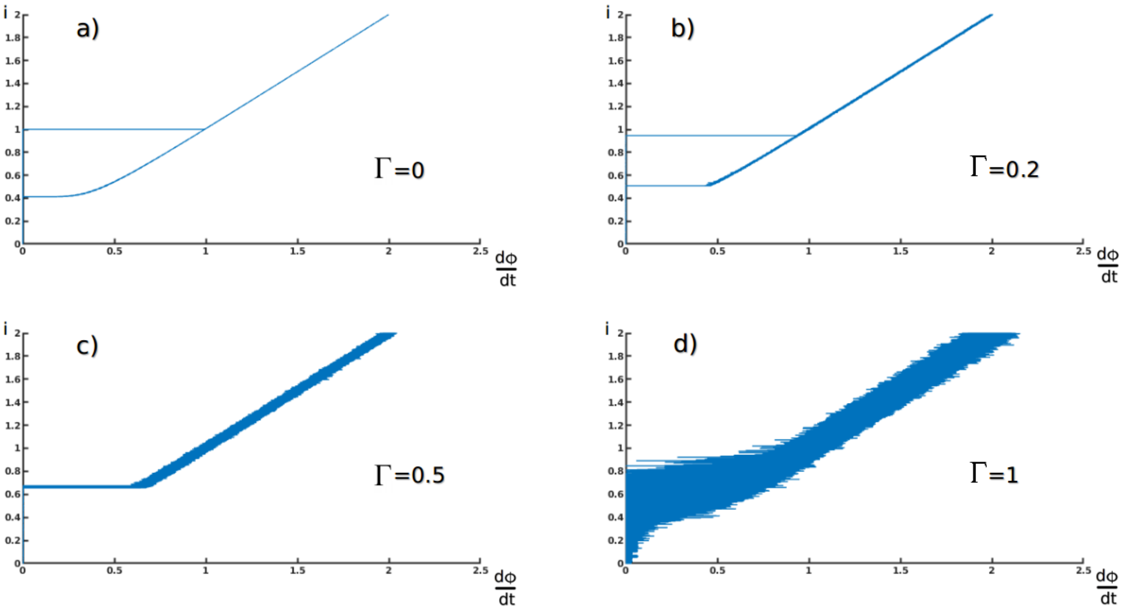

Figure 2.2: Noise affected curve in the RSJ model with Q=3 simulated using a C algorithm for different value of Γ

1 state is reduced below the current i_{s0} and the bias i_r, at which the junction returns to the 0 state is raised above i_{r0}. In the same manner, we will refer to I_{c0} to indicate the critical current in the absence of fluctuations and I_c to the switching current in the presence of thermal noise. This definition will be useful in the following Chapters

At a higher temperature, $\Gamma = 0.5$, the hysteresis shown in fig. 2.2(a) and 2.2(b) disappears and the I-V curve simply shows a plateau at a bias level i_e Finally, for $\Gamma = 1$, the thermal noise disrupts the I-V curve: the effects are so strong that typical I-V characteristic is completely modified.

To understand the difference with respect to the case with $\Gamma = 0$ let's consider the basins of attraction in state space of the eq. 1.69. By definition, the basin of attraction of a given attractor is the region of state space that includes all sets of initial conditions leading to a motion on the attractor [55]. If the system is initially within this central basin, a thermally induced escape can take the system to an adjacent minimum either ϕ or $-\phi$ [62].

In the case in which $i < i_{r0}$, near the region of the central basin there are only O-state basins of attraction in state space. In this case, the system escapes to an adjacent minimum and remains in the 0-state, as shown in fig. illustrated in fig. 2.3 (a) [55].

For $i < i_{r0} < 1$ the 0-state and 1-state attractors coexist, and the topology of state space takes the form illustrated in fig. 2.3 (b) for Q=3 and $i = 0.5$.

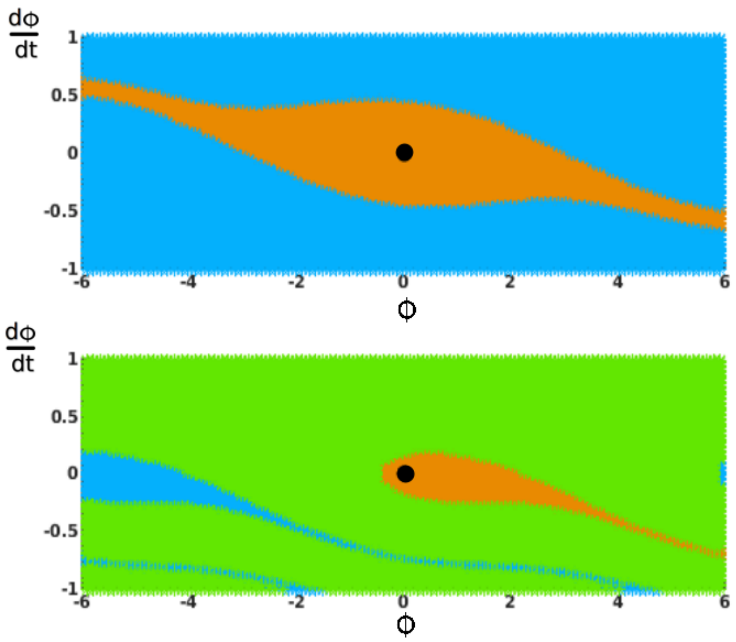

Figure 2.3: Basins of attraction of 1.69 in the case of (a) $i = 0.02$ and (b) $i = 0.5$. The black point represents the state (0,0). The orange regions are the basins of 0-state with minima in $\phi = 0$. The blue regions are the basins of 0-state with minima in $\phi \neq 0$.The green regions are the basins of 1-state

Because the blue region of 1-states attractor separates the basins of adjacent 0-state attractors, an escape event can't event to take the system directly from the basin of one potential minimum to that of a neighbouring minimum. The escape from the 0 state necessarily takes the system into the basin of the 1 state [55]. If the temperature is sufficiently low, the thermal fluctuations cannot induce a retrapping of the phase particle and it begins to accelerate toward the 1 state [55].
Instead, when the temperature is sufficiently high, thermal fluctuations can induce retrapping of the particle and the junctions switch back and forth between the zero-voltage state and the quasiparticle branch giving rise to the I-V curves (c) in fig. 2.2 [55]. This state is called *phase diffusion* [62].
The escape rate Γ_E from a minimum can be calculated within the theory of Kramers [59]:

$$\Gamma_E = a_t \frac{\omega_a}{2\pi} exp(-\frac{\Delta U_E}{k_b T}) \tag{2.7}$$

where ΔU_E is the height of the energy barrier from a washboard potential minimum to the adjacent maximum, $a_t = (1 + 1/4Q)^{1/2} - 1/2Q$ is a damping-dependent prefactor [60] and the quantities ω_a and ΔU_E are all current dependent:

$$\omega_a = \omega_p \left(1 - (I/I_{critical})^2 \right)^{1/4} \tag{2.8}$$

$$\Delta U_E \simeq \frac{4\sqrt{2}}{3} E_j \left(1 - (I/I_{c0}) \right)^{3/2} \tag{2.9}$$

Similar, one can define the rate of retrapping Γ_R for the inverse process, from the 1-state to 0-state.
This process cannot be treated within the theory of Kramers because the 1 state is a dynamic non-equilibrium state.
Ben-Jacob et al. [61] have obtained an analytic form for Γ_R:

$$\Gamma_R = \frac{I - I_{R0}}{I_{c0}} \omega_p \, exp\left(-\frac{E_j Q^2 (I - I_{R0})^2}{2 k_b T I_{c0}} \right) \tag{2.10}$$

where $I_{R0} \equiv i_{r0}$ is the retrapping current.
Eqs. 2.7 and 2.10 are valid in the limit of $k_b T \ll E_j$ [55]. It's important to note that in eqs. 2.7 and 2.10 are dominated by the exponential factor that can change by many orders of magnitude with small changes of the quantity in the exponent [55]. In underdamped junctions, with $Q > 10$, Γ_R is dominated by the factor $exp(-Q^2)$ and retrapping is negligible: the I-V curve is hysteretic and shows a similar behaviour to the moderate case with $\Gamma = 0.1$ as in fig. 2.2 (a). In overdamped junctions $Q < 1$ retrapping has an important role for each temperature T: the I-V curve is non-hysteretic, as in fig. 2.2 (c). The time-averaged voltage across the junction is nonzero and can be estimated as [55]:

$$< v >= \frac{1/\Gamma_R}{1/\Gamma_E + 1/\Gamma_R} v_1 \tag{2.11}$$

where v_1 is the voltage in 1-state in absence of noise.
We conclude that the main effect of thermal noise is to reduce the hysteresis of the I-V characteristics such as at low temperature a moderately damped junction behaves like an underdamped one while at sufficiently high temperatures the phase dynamics is similar to the one in overdamped junction [62].

2.2 Switching current distributions

The effects of thermal noise on a Josephson junction can be analyzed also by the studying of the switching current distributions.

In the last section, we have considered the effects of the thermal noise on the I-V characteristics in a moderately-damped regime. We have schematized the thermal fluctuations by a source of random current i_n, and consequently the value i at which the junction switches is stochastic.
In this Section we analyze the current distributions starting from the eqs. 2.7 and 2.10.
The density of probability $p_E(I)$ of a switch in the current range I and $I + dI$ can be calculated as follow. If the escape events are supposed to be independent, the probability of a switch in the time interval dt:

$$dP(1; dt) = \Gamma_E dt \tag{2.12}$$

and similarly the probability of no switch in the time interval dt is:

$$dP(0; dt) = 1 - \Gamma_E dt \tag{2.13}$$

Then the probability of no switch in the interval I+dt is

$$P(0; t + dt) = P(0; t)dP(0; dt) = P(0; t)(1 - \Gamma_E dt) \tag{2.14}$$

that can be written in the form:

$$\frac{P(0; t + dt) - P(0; t)}{dt} = -\Gamma_E P(0; t) \tag{2.15}$$

In the limit of $dt \to 0$ we can integrate the last equation and obtain:

$$P(0; t) = exp\left(-\int_{t=0}^{t} \Gamma_E dt\right) \tag{2.16}$$

If we write the probabilities as a function of the bias current:

$$P(0; I) = exp\left(-\int_{0}^{I} \frac{\Gamma_E}{dI'/dt} dI'\right) \tag{2.17}$$

The density of probability p_E can be calculated deriving 2.17 respect to I :

$$p_E(I) = \frac{\Gamma_E I}{dI/dt}\, exp\left(-\int_{0}^{I} \frac{\Gamma_E}{dI'/dt} dI'\right) \tag{2.18}$$

By definition:

$$P(0; I) = exp\left(-\int_{0}^{I} \frac{\Gamma_E I}{dI'/dt} dI'\right) = 1 - \int_{0}^{I} p_E(I')dI' \tag{2.19}$$

Inserting 2.19 in 2.18 one obtains;

$$p_E(I) = \frac{\Gamma_E I}{dI/dt}\left(1 - \int_0^I p(I')dI'\right) \tag{2.20}$$

Similarly we can compute the expression for the p_R.

First one can observes that in eq. 2.21

$$p_E(I) = \frac{\Gamma_E\, I}{dI/dt}\left(1 - \int_0^I p(I')dI'\right) \tag{2.21}$$

for small currents, $\Gamma_E \ll \Gamma_I \equiv dI/dt$ so $p(I)$ is small.
When the current is increased toward the current I_{EI}, at which $\Gamma_E = \Gamma_I$, the first quotient 2.21 increases. Therefore as the current increase, the numerator of the second quotient begins to reduce from 1 to 0. We conclude that to have an escape $\Gamma_E \simeq \Gamma_I$.
In the following Sections we use the term *escape* to describe any (possibly short-lived) escape from the instantaneous 0-state to the 1-state. Instead, the term *switch* is used to describe an experimentally measured switch to the running state [62].
In the study of I-V curves, we have pointed out that the behaviour of underdamped and overdamped junctions can be considered as limits of the moderately damping case at low and high temperatures respectively. These considerations are still valid in the analysis of the switching current distributions and so we focus our attention on moderately damping junctions.
The effect of thermal fluctuations allows us to identify three different regimes in these junctions [62]: *thermal regime*, *phase diffusion regime* and *high temperature regime*.
The study of the switching current distributions in moderately damped case is particularly important for the analysis of the NbN-GdN-NbN junction [53], as we will discuss in the last Chapter.

2.2.1 Thermal regime

At low temperatures, before a certain value T^*, Γ_R is small and retrapping is negligible as in underdamped case. This can be seen in fig. 2.5 where we have shown the behaviour of Γ_E, Γ_R and Γ_I at $T = 0.3K$: when $\Gamma_I \simeq \Gamma_E$, a necessary condition to have a switch, $\Gamma_R \to 0$ and every switch events determine an escape of the phase particle. The density of probability reduces to:

$$p_S = p_E = \frac{\Gamma_E\, I}{dI/dt}\left(1 - \int_0^I p(I')dI'\right) \tag{2.22}$$

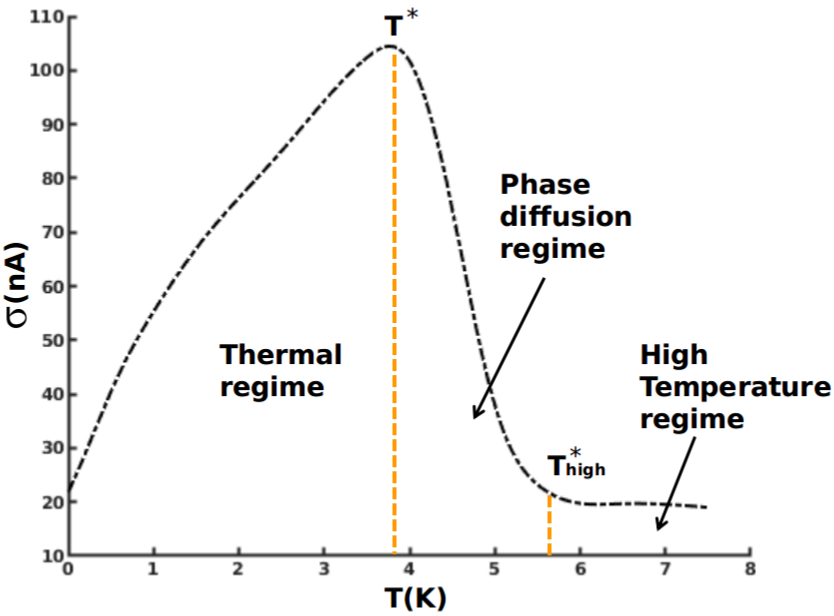

Figure 2.4: Distribution width vs T in NbN-GdN-NbN junction

In this regime the width of the distribution goes as $\sim T^{2/3}$ and the skewness[1] is around -1.
This is valid till the temperature T^* is reached: above T^* the width of distributions starts to fall as we will discuss in the *phase diffusion regime*.
In the fig 2.5 we also represent three switching current distributions at the same temperature: in green we have the one obtained starting from the eq. 2.21, the second in light blue is the experimental distribution in the NbN-GdN-NdN junction and the dark red is the Monte Carlo simulated distribution.
The distribution p_E, is in good agreement with the experimental results, confirming that for low T retrapping is negligible.

2.2.2 Phase diffusion regime

As the temperature increases, the current I_{EI}, at which $\Gamma_E \simeq \Gamma_I$ decreases and retrapping cannot be neglected. Above T^* the width departs from the thermal regime behaviour and starts to fall, as we see in the fig. 2.4. In other words, counter-intuitively the switching process in less stochastic than that

[1]The skewness is the ratio of the third moment about the mean to the standard deviation gives a simple one-parameter description of the shape of the distribution; a symmetrical distribution has zero skewness

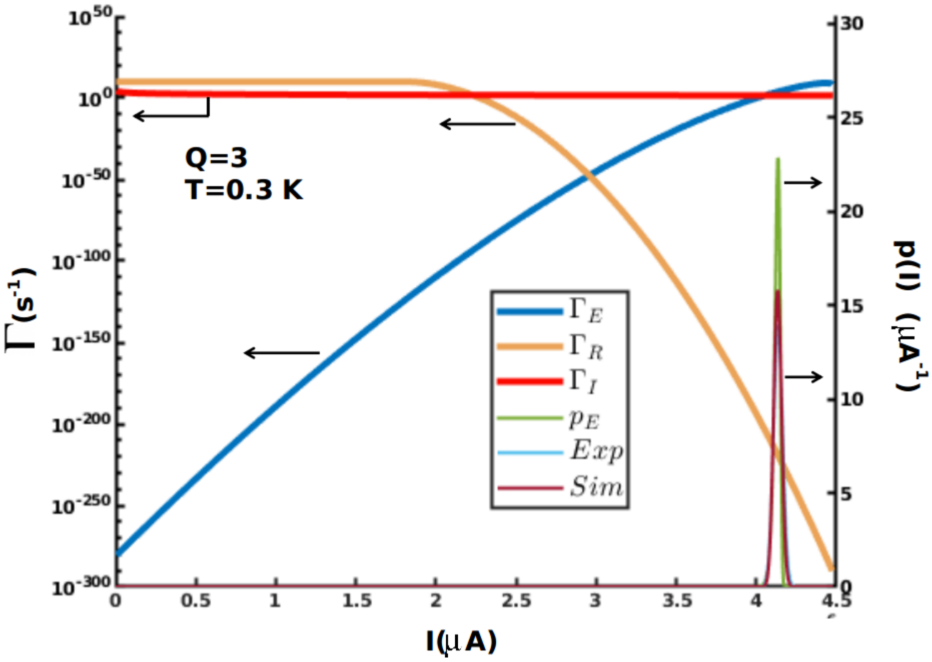

Figure 2.5: Variation in characteristic rates with current at $T = 0.3K$ for Q=3. The green distribution is the underdamped case (p_E). The dark red is Monte Carlo simulated distribution while the light blue's one (that is completely overlapped by the dark red curve) is obtained experimentally. The arrows indicate for each curve the respective y-axis

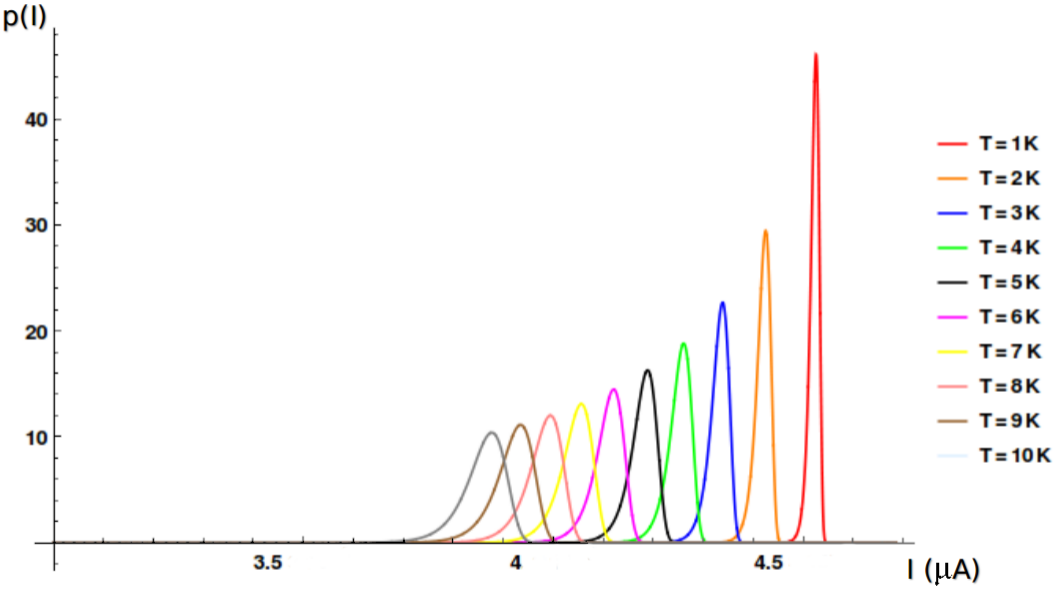

Figure 2.6: Switching current distributions from eq. 2.22 at different T

a lower temperature [60].
The skewness becomes progressively less negative until a positive value is reached [62]. This can be seen in fig. 2.7 where the experimental distribution (in light blue) is more symmetric and has smaller width respect to the underdamped distribution p_E (in green). This curve fails to replace to match the experimental data, while the Monte Carlo simulation (in dark red curve) is in a good agreement with them.
In fig 2.7 we have also represented the behaviour of Γ_E, Γ_I and Γ_R. Respect to the thermal regime case, a switching event occurs when $\Gamma_E \simeq \Gamma_R$, i.e $I \simeq I_{ER}$: for $I < I_{ER}$, $\Gamma_E \ll \Gamma_R$ and when the phase particle starts to go down the washboard potential, it's immediately retrapped.

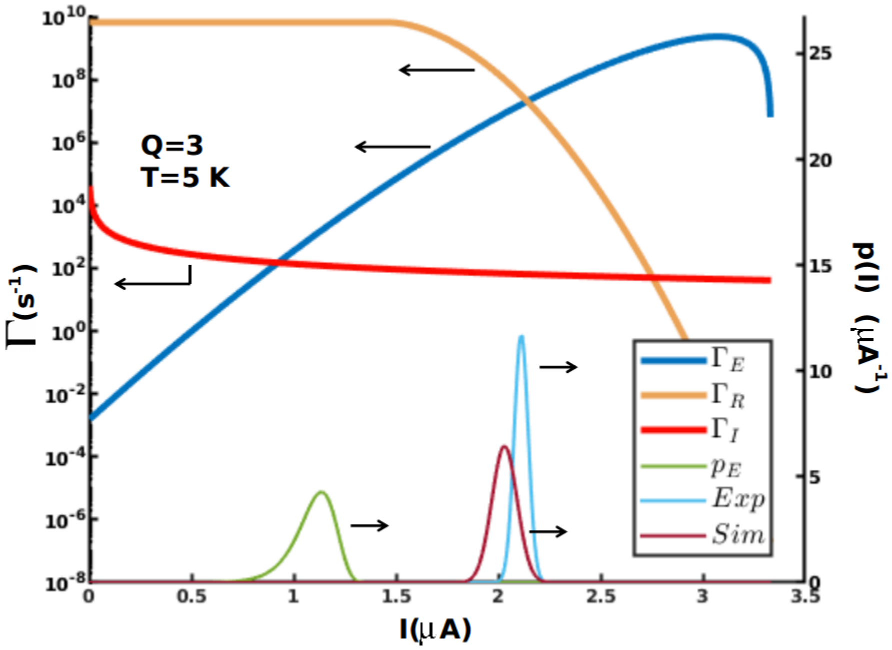

Figure 2.7: Variation in characteristic rates with current at $T = 5K$ for Q=3. As in fig. 2.5, the green distribution is the underdamped case (p_E). The dark red is Monte Carlo simulated distribution while the light blue's one is obtained experimentally. The arrows indicate for each curve the respective y-axis

2.2.3 High temperatures regime

Above a certain temperature T^*_{high} the expectation value of mean, width and skewness begins to level out [63] [64], as observed experimentally by Franz et al [65].

This corresponds to the situation in which the phase particle escapes and is retrapped several times in a minimum of the potential.

2.2.4 Dependence on Q

Considering the eq. 2.10, we see that rate Γ_R depends exponentially on the damping factor Q: small variations of this parameter determines important changes in the probability of retrapping.
These effects become particularly important in the moderately damping case, where we can identify three different regimes depending on the value of the temperature T.
In figure 2.8 we represent the dependence on Q of the width in simulated switching current distributions. We see that an increase of Q determines a greater value of T^* and $\sigma(T^*)$. This can be understood considering the expression of Γ_R 2.10: for greater Q retrapping becomes to be important for higher temperatures because of $\Gamma_R \propto exp(-Q^2/T)$. Consequently, T^* increases and σ gets higher value, having a greater range to increase as $T^{2/3}$. Below the respectively T^*, in fact, we can see that all the curves increases in the same manner: this reflects the fact that for $T < T^*$ the switching current distributions follows the underdamped distributions $p_E = p_S$, that depends very weakly by the damping factor Q.
Above $T > T^*$, we have a clear depends on Q: σ decreases smoothly for small Q than for high ones.

2.2.5 Dependence on rate

The fig. 2.9 we have shown the variation with current-ramp rate of the width of distributions. We can see that a decrease in the current-ramp rate corresponds determines a decrease of the maximum and a shift to $T = 0$ of T^*. Also T^*_{high} moves to the left and the width saturates with a lower value at a greater rate.

Our results are in agreement with the prediction of Fenton et al. [62] in their works

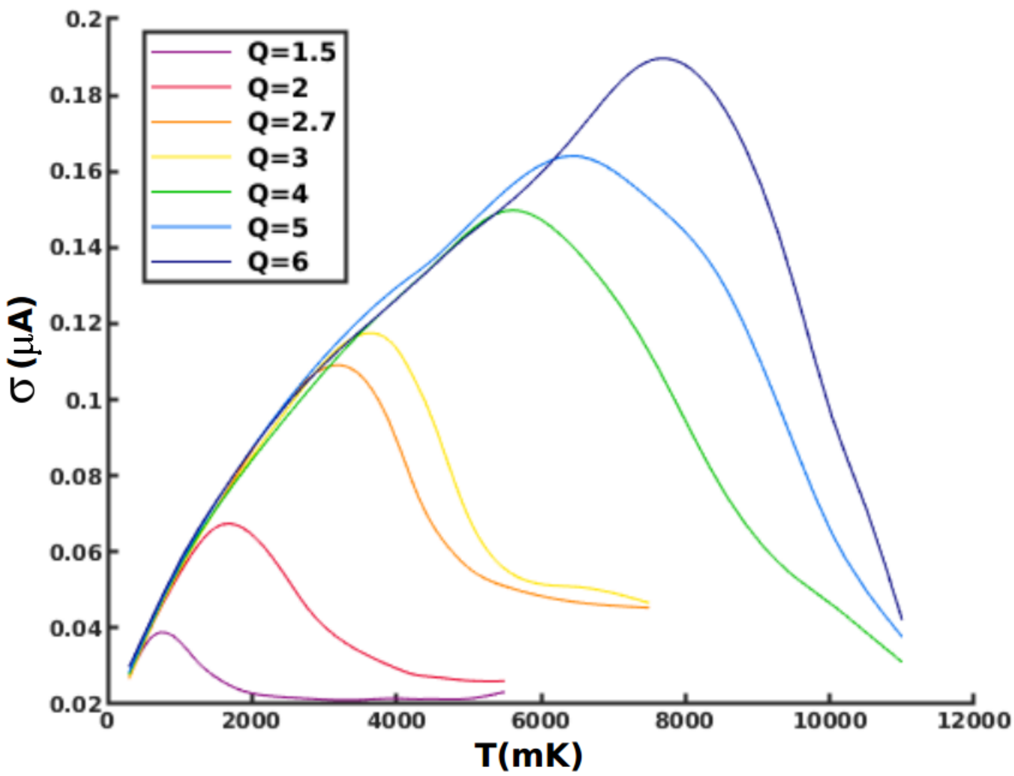

Figure 2.8: Dependence of the width from Q. This curves have been obtained with Monte Carlo simulations, as we will discuss in the last Chapter

2.3 Quantum regime

When the temperature T is sufficiently low the phase particle can escape from potential the potential minimum at ϕ_0 by tunneling through the potential barrier, as shown in figure 2.10.
This process, known as MQT (Macroscopic Quantum Tunneling), involves a macroscopic number of particles and thus its probability should be inherently small.
For making estimates we can use the *WKB approximation*:

$$\psi(\phi) \propto exp\left(i\int \lambda(\phi)d\phi\right) \tag{2.23}$$

where $\phi(\phi)$ is the solution of the eq. 1.76 The probability of transmission becomes [66]:

$$P \sim \omega_a \, exp\left(-E_c^{-1/2}\int_{\phi_0}^{\phi}\sqrt{U_j(\phi') - E d\phi}\right) \tag{2.24}$$

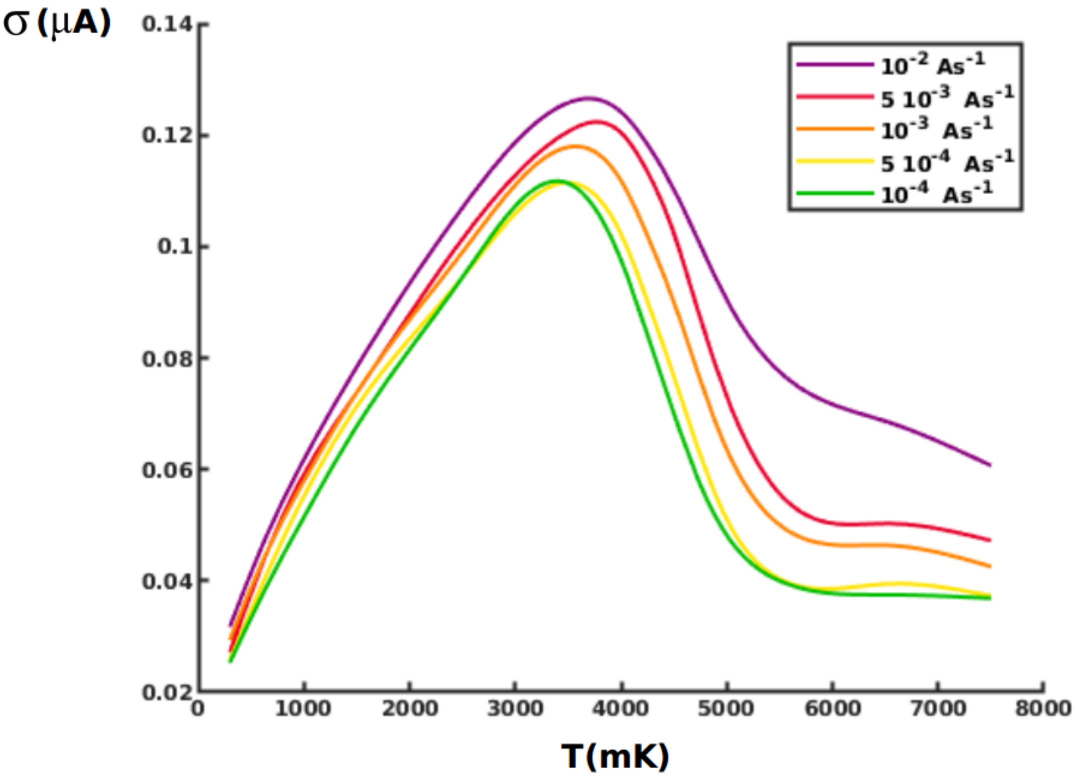

Figure 2.9: Dependence on rate of the switching current distributions. This curves has been obtained with Monte Carlo simulations, as we will discuss in the last Chapter

where ϕ and ϕ_0 are the turning points satisfying $E = U(\phi)$. For zero current, the phase particle tunnels from $\phi = 0$ to $\phi = \pi$. Writing $\hbar\omega_p = (E_j E_C)^{1/2}$ we can present the probabilty as :

$$P \sim \omega_p \; exp\bigg(-2\pi E_B/\hbar\omega_p\bigg) \tag{2.25}$$

where $E_B \sim 2E_j$ is the barrier height. The crossover temperature is given by $T_{cr} \approx \hbar\omega_p/2\pi$.
For typical value of $\omega_p \approx 10^{11}$, this correspond to $T \approx 100$ mK.
In the presence of moderate level of dissipation, Caldeira and Legget [67] have shown that the escape in quantum regime is, in the first order in Q:

$$\Gamma_q = a_q \frac{\omega_p}{2\pi} exp\bigg(-7.2\frac{\Delta U}{\hbar\omega_p}\bigg(1 + \frac{0.87}{Q}\bigg)\bigg) \tag{2.26}$$

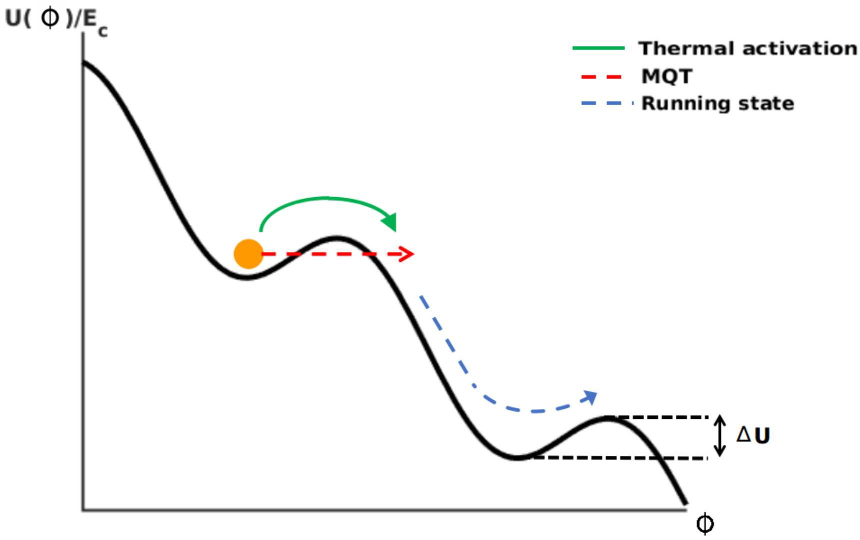

Figure 2.10: Phase dynamics of a Josephson junctsion

where ΔU is the barrier height, as in the thermal limit, Q is the damping factor and a_q can be approximated as:

$$a_q \simeq \left(120\pi 7.2\Delta U/\hbar\omega_p\right)^{1/2} \tag{2.27}$$

The reality of MQT and the predicted crossover temperature has been demonstrated definitively by Martinis et al. [68].
In their work they introduce an *escape temperatures* T_{esc} which is defined through the relation:

$$\Gamma = \frac{\omega_p}{2\pi} exp\left(-\frac{\Delta U}{k_b T_{esc}}\right) \tag{2.28}$$

We can analyze the limit of high and low temperature. We find that in thermal escape regime the eq. 2.7 reduces:

$$T_{esc} = \frac{T}{1 - p_t} \tag{2.29}$$

where:

$$p_t = \frac{ln a_t}{\Delta U/k_b T} \tag{2.30}$$

We see that this expression depends linearly on T.
Vice-versa, one can show that the in the quantum regime, when $T \to 0$, T_{esc} goes as:

$$T_{esc} = \frac{\hbar\omega_p}{7.2k_b}\frac{1}{1 + 0.87/Q}\frac{1}{1 - p_q} \tag{2.31}$$

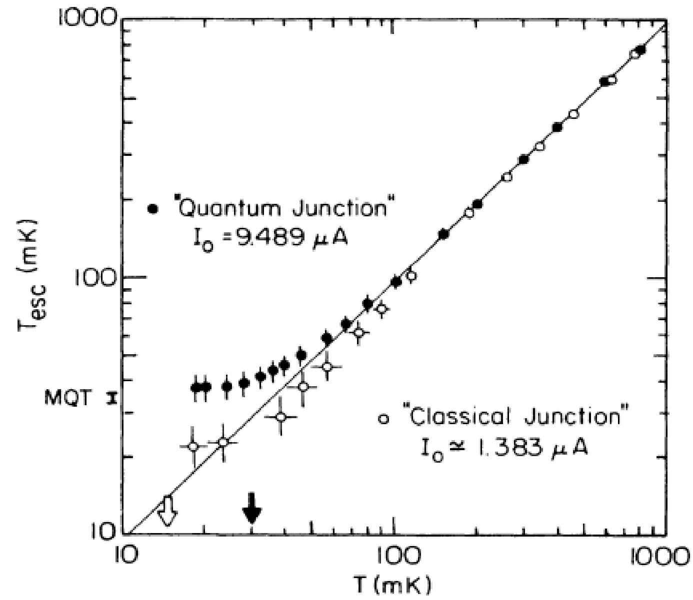

Figure 2.11: T_{esc} vs T for the high ("quantun junction") and low values ("classical junction") of I_0 with arrows indicating $Tcross$ [68].

where:

$$p_q = (lna_q)/\left(7.2\Delta U/\hbar\omega_p\right)\left(1 + 0.87/Q\right) \tag{2.32}$$

The experimental measurements are in very good agreement with the theory. They have evaluated the expression 2.28 in the case of a Nb based *SIS* junction. The results are shown in figure 2.12: we can see that for T above 100 mK the expected behaviour of the eq.2.29 is obtained. At temperatures below 25 mK , T_{esc} becomes independent of temperature, with a value in great agreement with the prediction of the theory of Caldeira-Legget[67].
In quantum regime the temperatures behaviour of the switching current distributions changes [53]: I_{mean} is constant in temperature while in thermal regime his values decreases by increasing T. Similarly, below the crossover temperature the width of the switching distributions is independent on T.
In 2015 Massarotti et al. [6] demonstrated the occurrence of MQT in NbN-GdN-NbN junction below a T_{cross} =70 mK. This phenomenon occurs because the junction's properties, such as the spin-filtering and the presence of low dissipation, drive in the appropriate window of junction parameters to observe MQT. In fig. 2.12 we can see the width dependence on the in the NbN-GdN-NbN junction: we can see the typical moderately damping behaviour in thermal regime and a saturation, as expected by the theory

Caldeira-Legget[67], below T_{cross}. The presence of the macroscopic supercon-

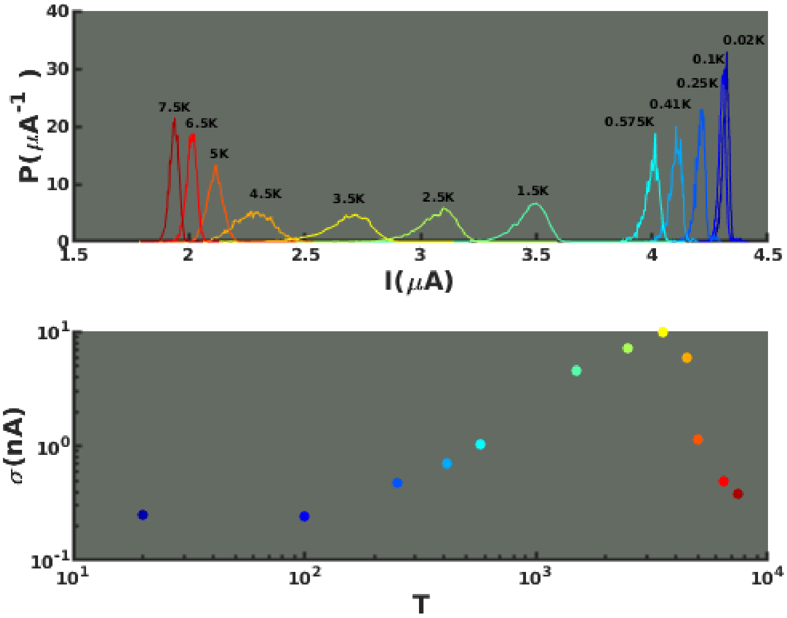

Figure 2.12: Distributions and widths vs T in NbN-GdN-NbN junction. As the temperature decreases below T_{cross}=70 mK the I_{mean} and the width of distributions becomes constant

ducting coherence allows the use of superconducting circuits as realizations of quantum bits, qubits [52] and in this sense demonstration of macroscopic quantum phenomena in spin filter devices gives promise for their application in quantum hybrid circuits [6].

Chapter 3

Experimental setup

This Chapter deals with the experimental set-up and the measurements techniques employed in this work to analyze our SI_fS junctions in a temperature range from room temperature down to 300 mK. We will especially focus on the description of the cooling system, of the filtering system, of the electronic-rack and of the measurements techniques, which allow to perform high precision and low noise measurements.

3.1 Cryogenic System

The study of superconducting phenomena is performed at low temperatures with the use of cryogenic systems, designed to minimize the effects of noise and to ensure the thermalisation of the samples. In our work we have performed most of measurements in a temperature range from a few hundred millikelvin up to some degrees kelvin, using an evaporation cryostat Oxford Instruments HelioxVL, immersed into a ^4He bath.
The dewar is composed of an internal chamber of 79 cm deep and an external one, which is at very low pressure of about 10^{-5}-10^{-3} mbar in order to decouples the cryogenic liquid from the environment. The dewar is equipped with a first screen of cryoperm, a nichel and aluminium alloy, and with a second one in lead, in order to shield the sample stage from external magnetic fields.

The sample is glued to a chip holder, bonded with Al wires and is subsequently mounted on the cryostat, ensuring electrical connection with the cryostat lines and room temperatures electronics.
The cryostat is closed using a brass cylinder, forming an inner vacuum chamber (IVC). A grease layer ensures a perfect closing of the IVC. This chamber is pumped down to a pressure of 10^{-2} mbar, using a rotative pump *Adixen PASCAL 2015sd*, shown in figure 3.1.

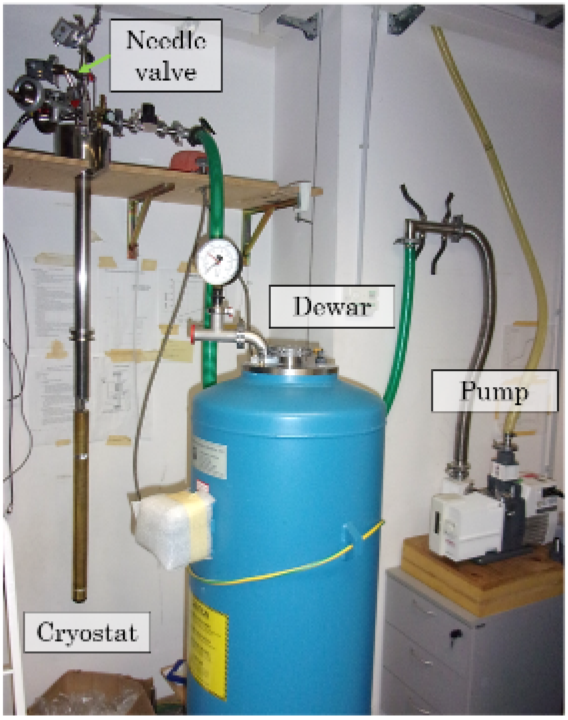

Figure 3.1: View of the experimental set-up

The cooling down from room temperatures to 300 mK is characterized by several stages:

- **From room temperature to 4.2 K** The cryostat is immersed in the ^4He bath in the *Dewar* and reaches the temperature of 4.2K via thermalization with the liquid. This process is ensured by the small amount of helium gas previously introduced in the *IVC*.

- **From 4.2K temperature to 2 K** A capillary draws liquid ^4He from the bath to a dump in the cryostat called *1K-pot*. Using a rotative pump *Adixen PASCAL 2015sd*, we remove the more energetic molecules reducing the temperature below 2K. The pumping is regulated with a *needle valve* that adjusts the 1K pot chamber pressure.

- **From 2K temperature to 300mK** The base temperature is reached using ^3He, contained in a closed circuit in the cryostat.
  This circuit crosses the 1K pot, so that the ^3He is in thermal contact with the *1K pot* dump. When the temperature of the 1K pot goes below 2.0K, the ^3He starts to liquefy and drops in the ^3He *pot*, another dump thermally anchored to the sample.

Finally, similarly to the previous step, we can lower the temperature to 300mK pumping on the ^3He bath with a zeolite pump, called *sorption pump* or *SORB*, that absorbs ^3He molecules, if its temperature is lower than 30K.
The different parts of the cryostat are shown in figure 3.2.

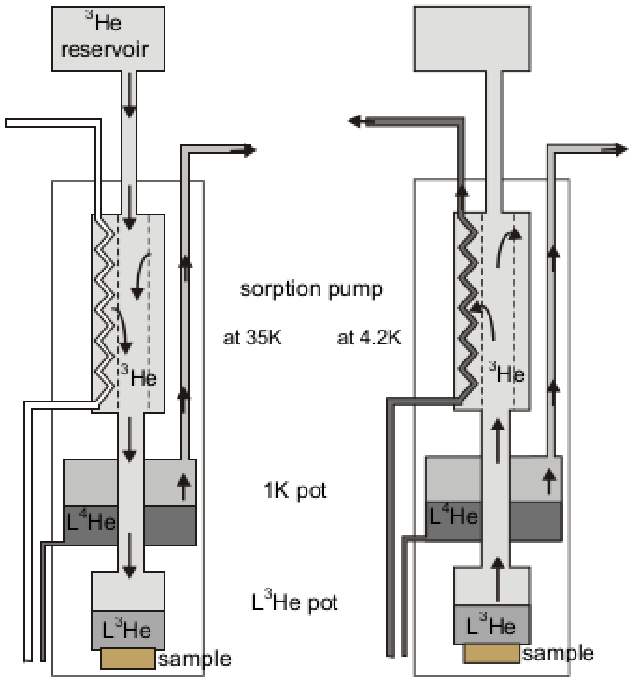

Figure 3.2: Sketch of the ^3He system during the condensing phase (a) and at the base temperature (b)

The system has three diode thermometer that monitor the temperature of the *SORB*, the *1K pot* and of the ^3He *pot*. Moreover, temperatures of the sample stage and of the sorb can be regulated indipendently by using two different heaters placed at the ^3He *pot* and at the *1K-pot*, respectively. We need to ensure that the junction is at the temperature which we want to measure, waiting sufficient time to provide a perfect thermalization of the sample. Previous analysis on the experimental setup have demonstrated that in this condition the error on the measured temperature is of the order of 1 %.

3.2 Electronic setup

We perform four-contact measurements to exclude from the overall measured resistance the contributions due to the connecting wires. The junction

is bonded to the chip holder through aluminum wires. We use manganin cables for the voltage lines that connect the instruments to chip holder. This material is widely used in cryogenic measurements thanks to its low thermal conductivity (at low temperature, it is two orders of magnitude lower than the copper one) that helps in reducing the heat load to the refrigerating system [81]. The current lines, instead, are made of low resistance materials to avoid excessive heating. In particular we use niobium-titanium (NbTi) cables in the points that reach low temperatures (as *1K* and ^3He *pot*), because this material becomes superconducting below about 10K. The rest of current cables are made by copper wires, because this material has a low resistance compared to other materials.
Overall, electrical lines resistance is about 100 Ω for current-carrying lines and about 200 Ω for voltage lines.

3.2.1 Filtering system

The experimental study of Josephson systems leads to the measurement of currents of the order of micro-Ampere or less and voltage about micro-Volt; consequently we need high resolution measurement setup and very low noise environment. The noise depends on several factors such as the temperature, the electronic instruments and the properties of the sample just to mention a few. The most effective way to filter noise in cryogenic system is to use several filtering stages at different temperatures [81]. This strategy is needed to progressively filter the signal and to obtain an efficient cooling of the filters themselves [81].
Our system is equipped with two stages of filters: a low pass RC-circuits with a cut-off of about 1 MHz, installed at the *1K-Pot* stage and two copper powder filter stages with typical cut-off frequencies of about few GHz, installed at the *1K-Pot* stage and at the ^3He *pot* stage.

RC filter The first filtering stage is composed for each measurement line by a 100 Ω resistor and two 1nF capacitors in parallel configuration, anchored to the *1K-Pot* stage . Everything is then enclosed in a copper box to allow good thermalization. From the values of the resistors and capacitors a cut-off frequency of 1.6MHz is obtained. The main advantage of this type of filter is the possibility of filtering a different lines in a small volume. The disadvantage is the loss in attenuation at high frequencies due to the parasitic capacitance of the resistors.

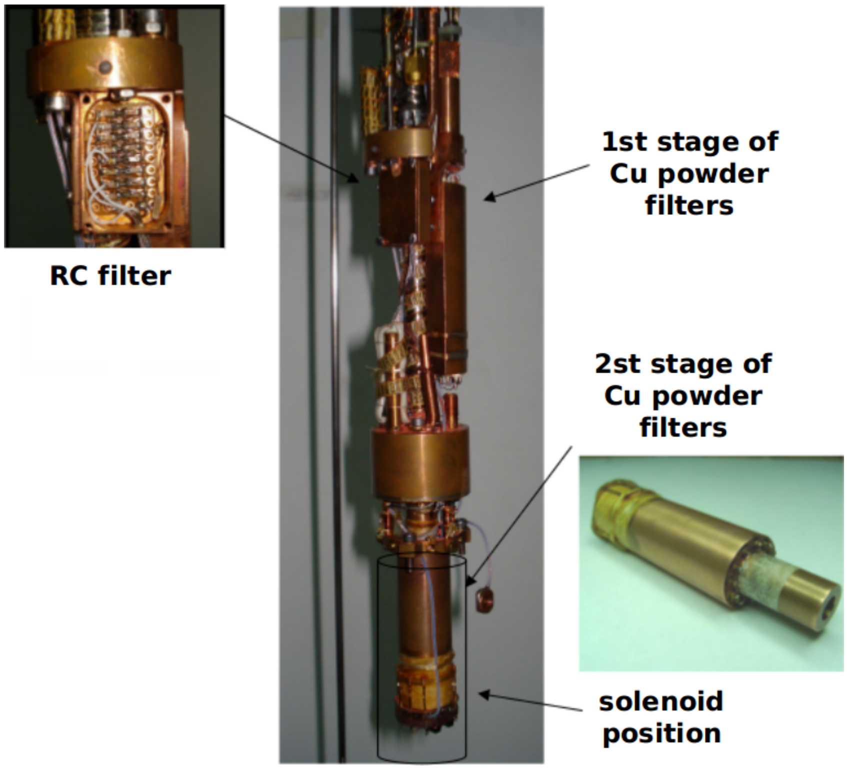

Figure 3.3: Filters mounted on the Heliox ^{3}He system. The position of the coil is also indicated.

Cu powder filters The copper powder filters were first described by Martinis et al. [55] and they are used in experiments requiring the highest level of filtering [81]. They are realized with a spiral coil of insulated wire inside a tube filled with metal powder with a grain size that can go from 5 to 30 μm. The cut-off frequency is in the range of few GHz.
The improvement that this type of filter introduces is shown in the fig.3.4 where we report an IV curve of $YBCO$ based sample at 0.3 K measured with and without Cu powder filters. As we can see, the reduction in electronic noise brings an increase in the measured critical current of about 35 % [81].

3.3 Experimental measurements

We have performed measurements of the I-V characteristic, the resistance as a function of temperature and switching current distributions (SCD) that allow us to reconstruct the electrodynamics properties of the NbN-GdN-NbN Josephson junction will be shown in Chapter 4. The following instruments

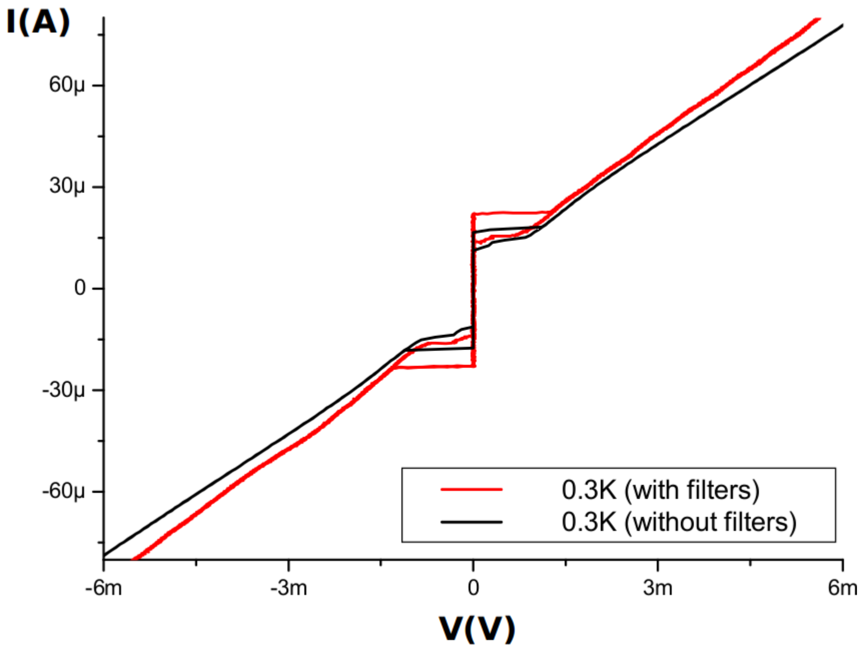

Figure 3.4: I-V characteristics of the same YBCO based junction measured with Heliox system equipped with filters (red curve) and without filters (black curve) at 0.3 K [81]

are used to perform most of the transport measurements reported in the next Chapter:

- *LeCroy Wave Runner 6100A* oscilloscope
- SR570 Standard Research Systems preamplifier
- *Agilent 33120A waveform generator*;
- *EG&G Princeton Applied Research 5210* lock-in amplifier;
- Source Meter *Keithley 2400* used as a current generator to produce magnetic fields
- Nanovoltmeter *Keithley 2182* used in R(T) measurements.

3.3.1 Current-voltage characteristics

The current-voltage characteristic (IV) allows to investigate some fundamentals properties of the junction. To obtain this curve we use an *Agilent 33120A* that generates a voltage triangular waveform with a peak-to-peak V_{pp} amplitude at low frequency, of the order of 10 Hz. The current flowing through the device is:

$$I_{bias} = \frac{V_{pp}}{R_{shunt} + R_{line} + R_{junction}} \simeq \frac{V_{pp}}{R_{shunt}} \tag{3.1}$$

and this corresponds to an effective current polarization if R_{shunt} is chosen to be much larger than the resistances of electrical lines and the junction.
The error on the generated voltage is 0.1% V_{pp} from the instrument specifications [70] and similarly for the generated current.
The voltage signal generated is showed on the oscilloscope *WaveRunner 6100A*, so as the current in the JJ, pre-amplified by the *SR570 Preamplifier*. The measured voltage drop on the junctions electrodes V is amplified by an operational amplifier with a 500 gain and measured on the oscilloscope. This instrument records a number of 100 curves and make an average of the measured signal in order to reduce noise effects.
The oscilloscope is connected to the computer, where we saved all the measurements. In fig. 3.5 we show a scheme of the electronic set-up. While we

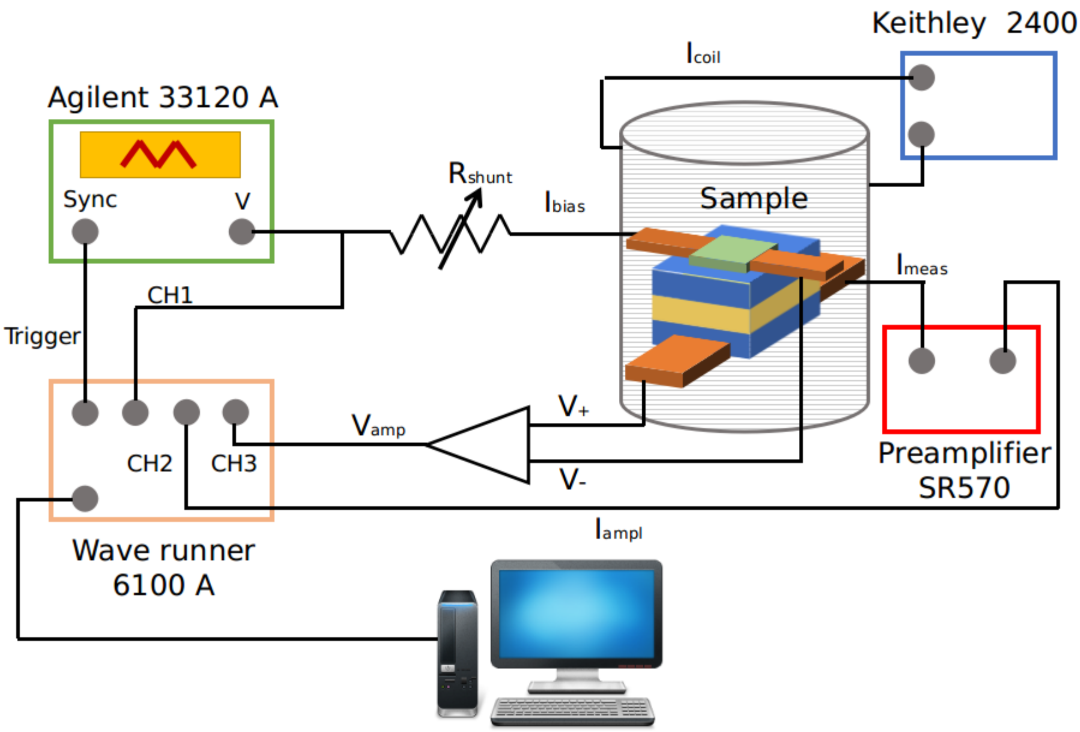

Figure 3.5: Electronic set-up configuration for I(V) measurements

have a good control on the bias current, the measured voltage is obvsiouly affected by the effects of noise. The experiments and the analysis performed over time on our experimental setup suggest that a reliable estimation of the error in the measured voltage can be given analyzing the noise range in the I-V curves as shown in fig. 3.6 and is about 1 % of the measured value. This estimation comes from the ratio between the error bar and the signal amplitude.

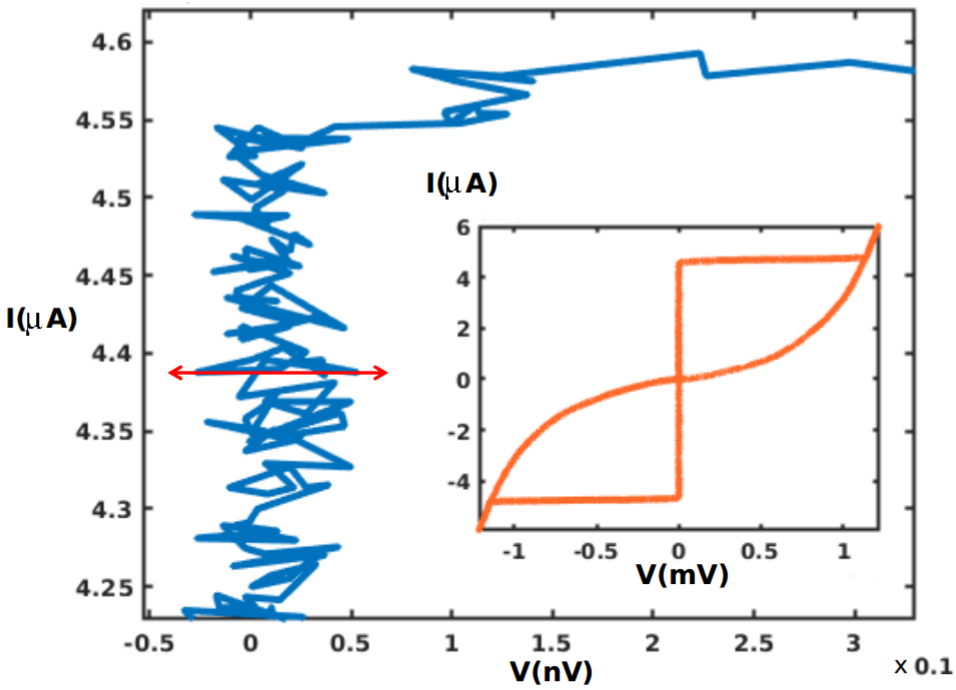

Figure 3.6: Error bar in a typical measured I(V). In particular we have reported in the inset the I(V) curves of the NbN-GdN-NbN junction at 0.3 K. The blue line is a zoom of the I(V) curve .

3.3.2 Switching current measurements

The experimental setup used to measure switching current distributions is analogous to the I-V one. Measurements have been performed by choosing a voltage threshold fixed to $\pm 100\mu V$. This value is smaller than the energy gap and sufficiently large to avoid the voltage fluctuations due to the thermal noise.

When the threshold voltage occurs, indicating a switch to the normal state, the corresponding bias current is recorded by the oscilloscope. This operation is repeated 5000 times in order to obtain an histogram of the switching events.

3.3.3 R(T) measurements

Some properties of a Josephson junction, such as the transition temperature T_c and the spin filter efficiency can be well analyzed starting from the $R(T)$ curve. We have performed this measurement generating a sinusoidal waveform with root-mean-square amplitude $V_{rms} = 100 \pm 1mV$ at 11.123 Hz. The amplified voltage drops between the two superconducting electrodes V and is read by *EG&G Princeton Applied Research 5210* lock-in amplifier, which allows high accuracy AC measurements. This instrument integrates the voltage curve taking as reference the signal waveform generator, over a period of time ten times larger than the signal one. In this way only the signal at the same frequency of the lock-in reference is preserved by integration while the other signal components are reduced close to zero. The amplitude (in rms) of the survived signal is read by the *Nanovoltmeter Keithley 2182* and divided by the bias current.
The lock-in allows also to measure the phase difference $\Delta\phi$ between the voltage drop on the junction V and the reference signal V_{pp} ; we required a $\Delta\phi \sim 0$ or π, because this value typically ensures a non-reactive coupling in the sample, which could be due to inhomogeneities or non-metallic contacts. The resistance error is about the 0.5 % considering the instrument specification [72]. In fig. 3.7 we show a scheme of the electronic set-up for the R(T) measurements.

3.3.4 Measurements in magnetic fields

Measurements of transport properties as a function of magnetic field have been performed by using a niobium-titanium coil, which is superconducting below a critical temperature of about 10 K. A copper wire inside a thermal insulating twist provides thermal contact between the coil and the 1K-Pot, so that the coil is always at about 2 K and additional Joule dissipation due to the current flow in the coil does not heat the sample stage.
We use a *Source Meter Keithley 2400* as a current generator to feed the superconducting coil.
The error on the generated current is about 0.1 %, as declared in the instrument specifications [71]. The instruments setup is similar to those described in fig. 3.5: for each value of the magnetic field we acquired the I(V) characteristic, with a step ΔI_{coil}. The *Fraunhofer pattern* is obtained applying a magnetic field from zero to an upper value (virgin curve); after that, we applied a field from a positive value to a negative value (down curves), and return (up curves). In this case the error of the value of magnetic field is

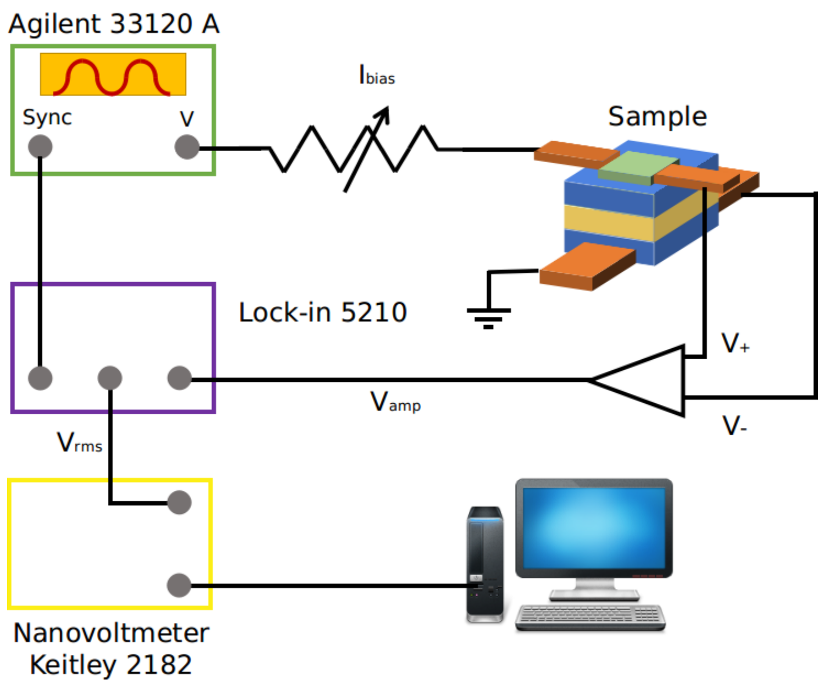

Figure 3.7: Electronic set-up configuration for R(T) measurements

about the step-field used and can be calculated starting from the ΔI_{coil} value:

$$\Delta H(G) = 3\Delta I_{coil}(mA) \tag{3.2}$$

3.4 Samples scheme

In this work, we have analyzed unconventional Josephson junctions with an insulating ferromagnetic barrier of 3 nm, gadolinium nitride (GdN), between two niobium nitride (NbN) superconducting electrodes.
Our junction was fabricated at the Materials Science and Metallurgy Department of the University of Cambridge (UK) by optical lithography from trilayer NbN-GdN-NbN films prepared by DC reactive magnetron sputtering at room temperature. A 5 nm MgO buffer layer was deposited on a SiO_2 substrates before the deposition of the trilayers. [43]
The GdN barrier was prepared in an Ar gas atmosphere containing 8% N_2, whereas NbN layers were prepared with 28 % N_2 [43].
The junction area, in a square geometry, was defined by selective reactive etching of the top 100 nm NbN layer in CF4 plasma. The error on the electrodes thickness is ±10 nm. A layer of sputtered SiOx was patterned using the lift-off method to provide an electrically isolated contact window on top

of the 7×7 μm^2 junctions.
While the NbN base layer acted as the bottom contact, a Nb wiring layer was patterned to achieve the top contact [43]. In figure 3.8 a sample with its

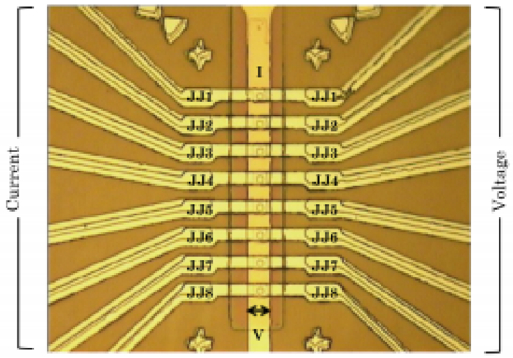

(a) Front view on the microscope

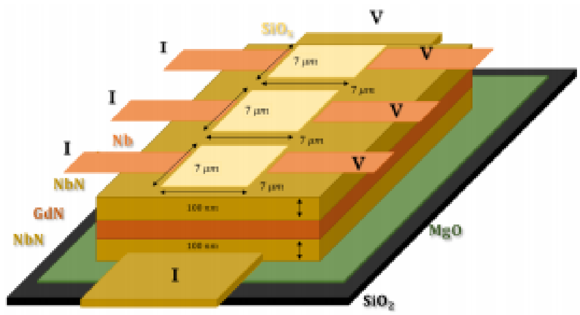

(b) Tranverse sketch of the samples

Figure 3.8: In (a): front view of the samples; in (b): a transverse sketch of the samples, which highlights dimensions and structure of the measures junctions [6]

typical dimensions and its contacts scheme is shown.

Chapter 4

Experimental results

In this Chapter, we condense all the experimental results with the final aim of a detailed characterization of the electrodynamic properties of the NbN-GdN-NdN junction with a barrier thickness of 3 nm. We will analyze the spin-filter properties of this device starting from the $R(T)$ measurements. We will report the dependence of the critical current on the magnetic field and on the temperature, respectively $I_c(H)$ and $I_c(T)$,and we will describe of the junctions electrodynamics by studying the switching current distributions curves, making a comparison with the simulated ones.

4.1 R(T) analysis

In fig. 4.1 we show the measurement of resistance as a function of the temperature. The junction has a semiconducting behaviour from room temperature down to about $T \simeq 35$ K, where the resistance starts to decrease. This is due to the onset of ferromagnetism in gadolinium nitride, which is reported to have a bulk Curie temperature of about 60 K [73]. Below the Curie temperature, the spin-dependent splitting of the band structure causes a spin polarization in the incoming charge current [74], because spin-up and spin-down electrons experience different effective barrier heights, and one channel is partially suppressed.
The resistance falls to zero at a temperature of about 12 K, when the electrodes become superconducting.
As we have anticipated in the first Chapter, the spin filter efficiency can be written as:

$$P \sim tanh\left(cosh^{-1}\left(\frac{R^*}{R}\right)\right) \tag{4.1}$$

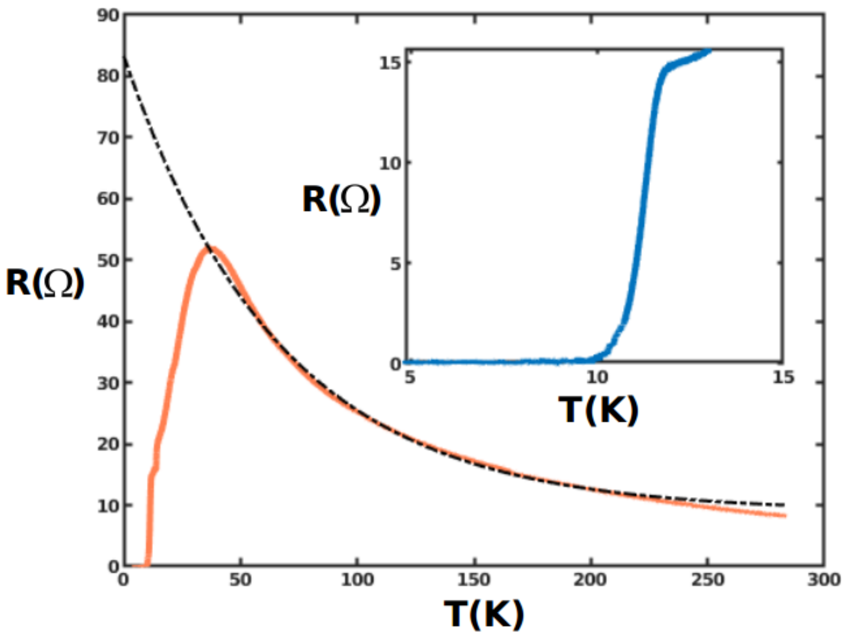

Figure 4.1: Resistance versus temperature curve measured on spin filter NbN/GdN/NbN JJ. The black dashed line is a fit of the experimental data for temperatures higher than ≈35 K by using a decaying exponential function. The inset shows a zoom of the NbN superconducting transition, at about 12 K.

where R^* is the resistance that the junction would have if it acts like a non-spin-filter junction and R is the measured one and depends on the thickness of the barrier. A practical indirect way to estimate the spin-filtering efficiency P is to compare the semiconductor-like device resistance R^* (resistance in absence of spin-filtering) with the junction resistance R at a fixed temperature $T_c < T < T_{Curie}$.
R^* can be extrapolated by fitting the experimental curve above T_{Curie} with a simple decaying exponential function (dashed black line in fig. 4.1). In this way we have we have estimated $P = 95\%$ at 15 K, that is in good agreement with the previous analysis on this junction [43] with 3 nm barrier.

4.2 I$_c$(T) curves

The I-V characteristics of the junction provide a first method to investigate its fundamental properties. In fig. 4.2 we have reported the I(V) curves in a temperatures range between 0.3 K and 7.5 K, measured according to the protocols described in Chapter 3. We can see that an increase in the temperature determines a reduction of the critical current and the hysteresis,

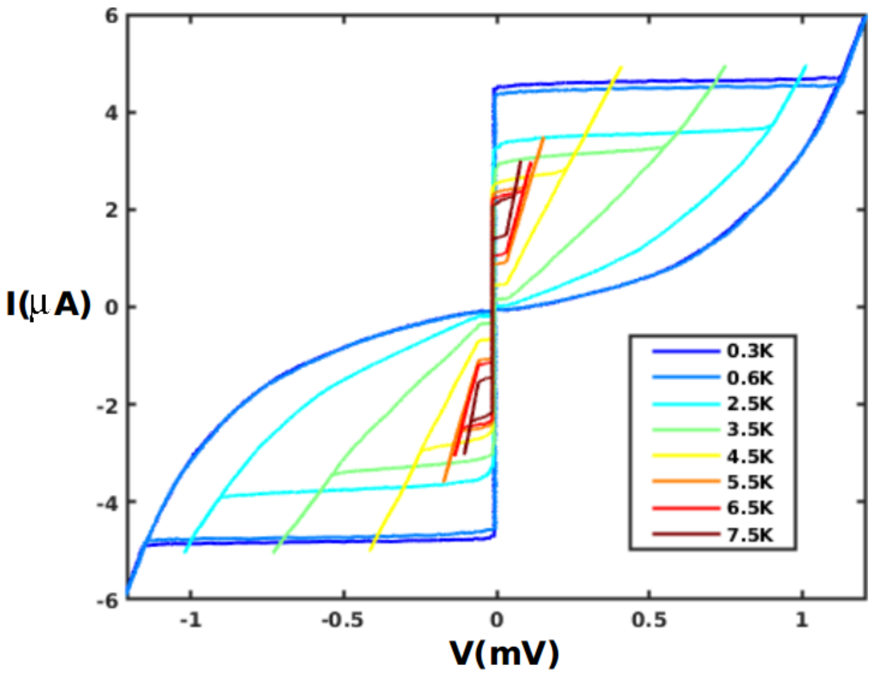

Figure 4.2: IV characteristics of NbN-GdN-NbN junction at different temperatures

as expected from the considerations of the second Chapter.
Following ref. [43] we can quantify the hysteresis in temperature defining the function:

$$H_y = \left(\frac{I_c - I_R}{I_c} \right) \tag{4.2}$$

where I_c is the critical current affected by the thermal fluctuations and I_R is the retrapping current. The curve $H_y(T)$ is shown in fig. 4.3. The result is in good agreement with previous analysis on this type of junction [43]. Moreover, it turns out that hysteresis is very large, above 95 % below 1 K, thus indicating very low values of the retrapping current at low temperatures.
The IV curves help us to have a first estimation of I_c as a function of the temperature T, as shown in fig. 4.4 where we have compared the behaviour of the experimental points with the theoretical curve predicted by the AB(Ambegaokar and Baratoff) relation. I_c(T) shows a clear unconventional temperature dependence, with an absolute magnitude much lower than predicted by the *AB relation* [45].
We can distinguish three different regimes:

- From $T = 300mK$ to $T = 5K$ the critical current decreases faster than what predicted by the *AB relation*

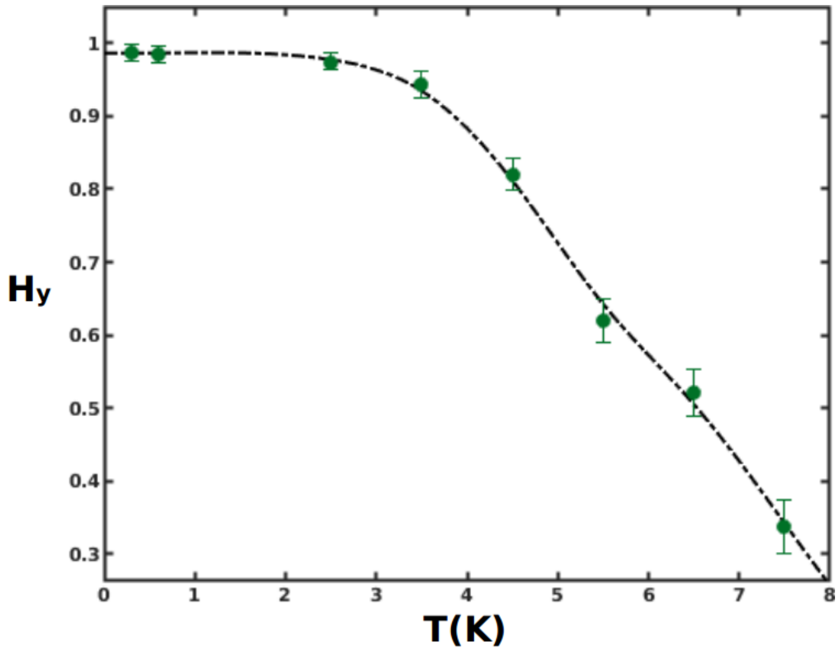

Figure 4.3: Hysteresis in the IV characteristics as a function of the temperature for the spin filter Josephson junction. The line is a guide for the eye

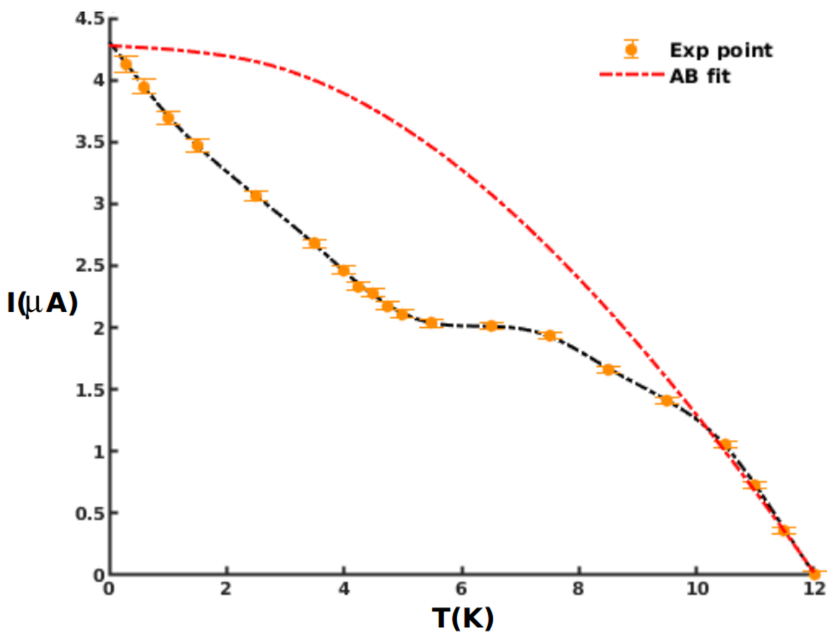

Figure 4.4: Orange points represent the Ic(T) values with their errors. The black dashed line is a guide for the eyes. The red dashed line is the AB fit following [8]

- From roughly $T = 5K$ to $T = 9K$ a plateau occurs
- Above $T = 9K$ the critical current decreases with a slope consistent with the AB predictions.

As pointed by Caruso et al. [7], this behaviour does not have any analogy in literature and cannot be explained by any of the common theories on ferromagnetic Josephson junctions. The peculiar trend of the I_c suggests that something far from the conventional superconductivity happens in this device.

4.3 Fraunhofer pattern analysis

The ferromagnetic nature of the GdN determines important magnetic features in the transport properties of the junction.
First, we have magnetic hysteresis in the Frohunofer pattern due to the presence of the intrinsic magnetization of the barrier, as discussed in the first Chapter. In fig. 4.5 we have reported the Fraunhofer pattern of the NbN-GdN-NdN junction at $T = 0.3$K. These curves have been obtained changing in step of 2.5 ± 0.1 G the magnetic field and recording for each step the critical current.
In these measurements we never reached the saturation field, and we only moved on the linear branch of the magnetization. We can observe that the first minima in the pattern are not effectively zero: this could be due to a non-uniform current distribution in the system, as in *SIS* junctions with structural imperfections of the barrier or to the presence of higher harmonics in the current phase relation [7].
The study of the Fraunhofer pattern provides a useful tool to investigate the effects of magnetic field on the unconventional behaviour of $I_c(T)$. As pointed out in ref. [6] the presence of a remnant magnetic field can change significantly the behaviour of I_c(T), and the plateau we observe at intermediate temperatures might be due to residual or trapped magnetic field. In order to overrule this possibility, we have measured I_c(H) curves at different temperatures, and collected their principal maxima, regardless of their position. The temperature dependence of I_c(H) maxima confirms the I_c(T) curves obtained from I−V(T) curves measured before magnetizing the sample, as shown in fig. 4.6. This allows us to exclude any effect due to barrier magnetization [6].

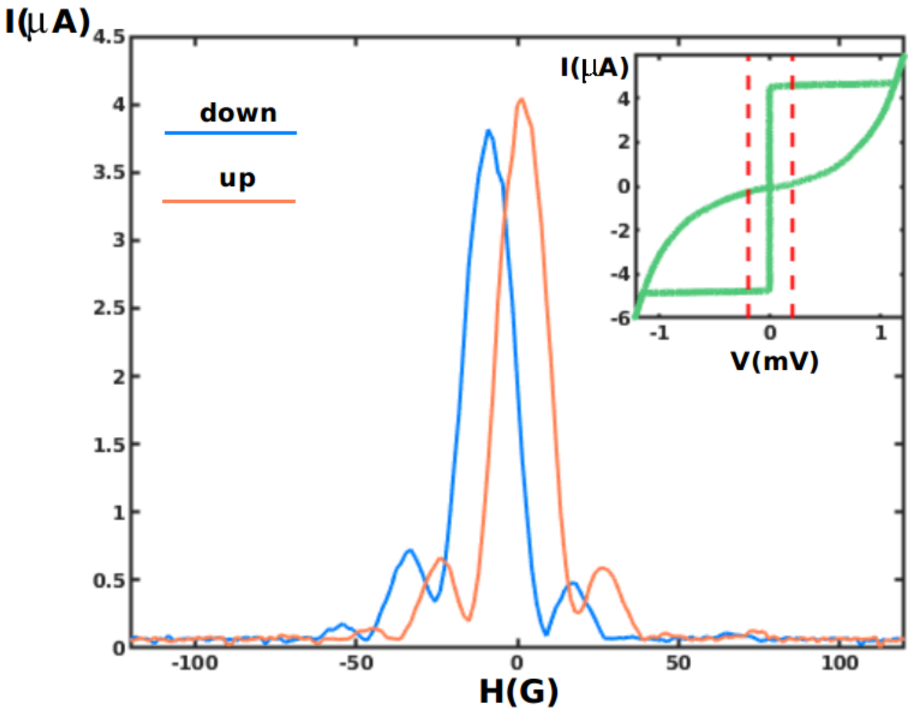

Figure 4.5: Critical current versus magnetic field plot for $T = 0.3K$ in NbN-GdN-NbN junction. The blue curve has been obtained starting from $H = 200G$ to $H = -200G$. Vice-versa for the orange curve. The inset represents the IV characteristics for the junction at 0.3 K. The red dashed lines are the threshold at $V = \pm 200\mu V$

4.4 Experimental Switching current distributions

In the underdamped JJs the measures of the switching current distributions as a function of temperature is a key tool to evaluate in detail dissipation in the junctions [6]. This method represents the direct tool to investigate the dynamics of the junction allows to provide the electrodynamic characterization which is not accessible otherwise [6].
The experimental measurements have been performed in a range of temperatures between 0.3 K and 7.5 K at $H = 0\ G$. For each temperature, we have measured the switching current distribution following the procedure described in Chapter 3 and we have calculated the first three central momenta: the mean switching current I_m, the standard deviation σ and the skewness μ. These parameters provide distinctive fingerprints of the different dissipation processes involving the dynamics of the junction and the comparison with

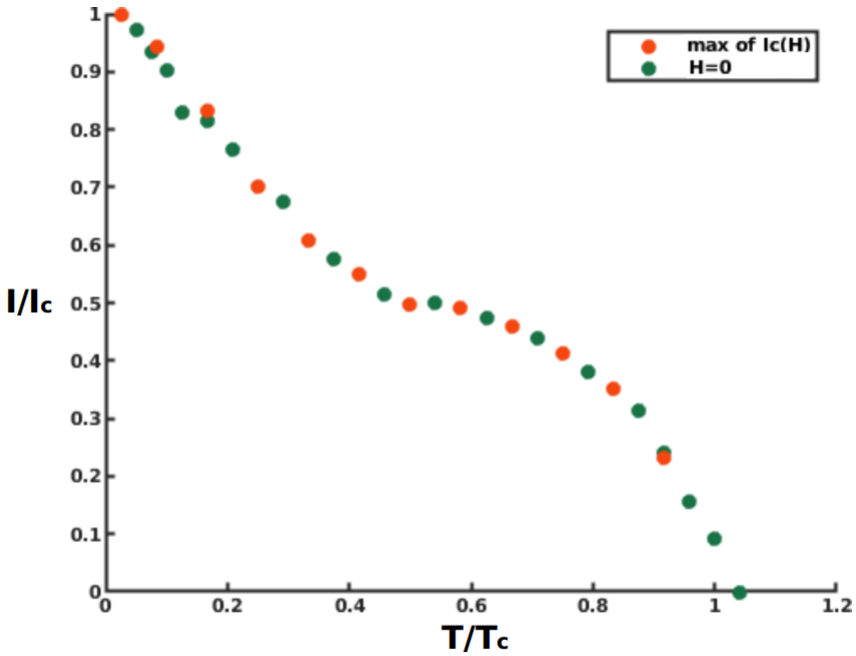

Figure 4.6: Comparison between I_c(T) curves obtained from IV characteristics at zero field (green points) and from the maxima of I_c(H) (orange points). The error is of the size of points

Monte Carlo simulations allows us to determine the electrodynamics parameters of the system. In fig. 4.7 we show the experimental switching current distributions at different temperatures. The moments of this curves can be calculated starting from the statistical analysis of the histograms [75]. The I_m values have been obtained from the equation:

$$I_m = \sum_i^N p_i I_i = \sum_i^N \frac{n_i}{N} I_i \tag{4.3}$$

where N is the number of switching current events, while $p_i = n_i/N$ and I_i are the frequency and current value of the i-th bin respectively, being n_i the number of counts in the i-th bin.
The statistical errors on I_m have been calculated from the expression:

$$\Delta I_m = \sqrt{\sum_i^N (I_i \Delta p_i)^2 + \sum_i^N (p_i \Delta I_i)^2} \tag{4.4}$$

Here ΔI is the error on the measured value of the current and Δp_i is the error on the number of counts recorded in the i-th bin. We estimated Δp_i

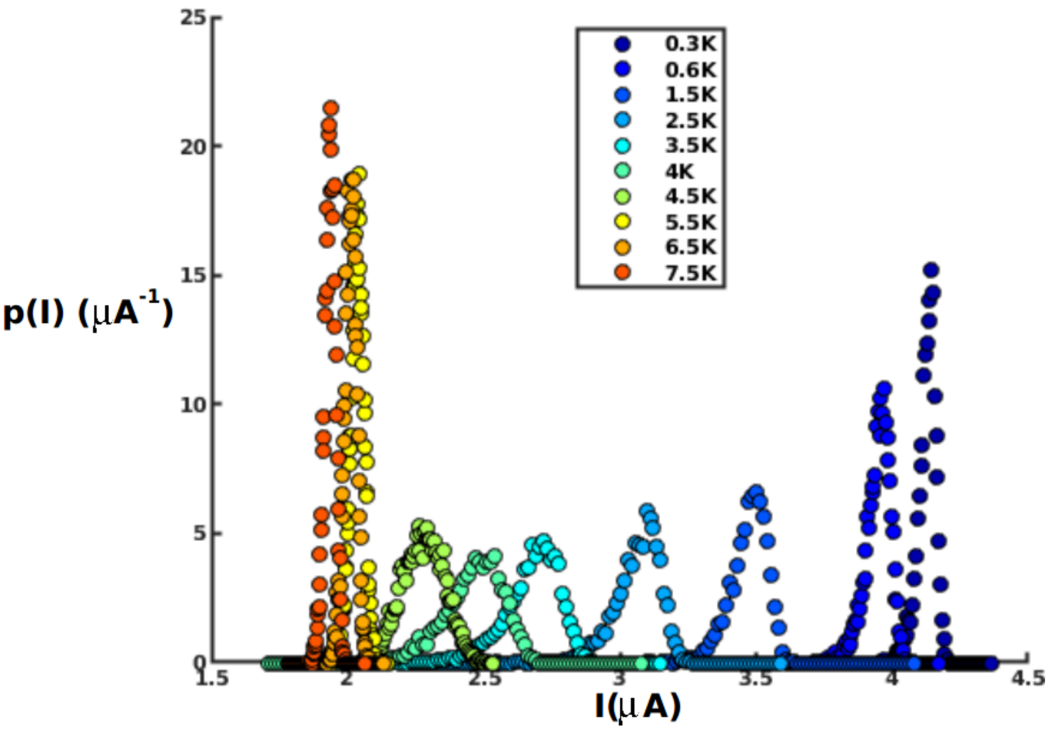

Figure 4.7: Experimental switching current distributions

considering the Poisson error on counts:

$$\Delta p_i = \frac{\sqrt{n_i}}{N} \tag{4.5}$$

Because in our discussion $\Delta p_i \gg \Delta I_i$, we have neglected the second term in the square root in the eq. 4.4. The statistical errors are of the order of 1 %. The $I_m(T)$ curves obtained from the switching current distributions follow the behaviour showed in fig. 4.4, confirming the presence of unconventional processes in the dynamics of the junction.
To study the properties of the junction we have to consider also are the σ values of the switching current distributions. These have been obtained from the equation [75]:

$$\sigma = \sqrt{\sum_i^N p_i (I_i - I_m)^2} \tag{4.6}$$

and their errors have been estimated following the equation:

$$\Delta\sigma = \frac{1}{2\Delta I_m}\sqrt{\sum_i^N [(I_i - I_m)^2 \Delta p_i]^2} \tag{4.7}$$

and are of the order of 5 %. The results are shown in fig. 4.8.

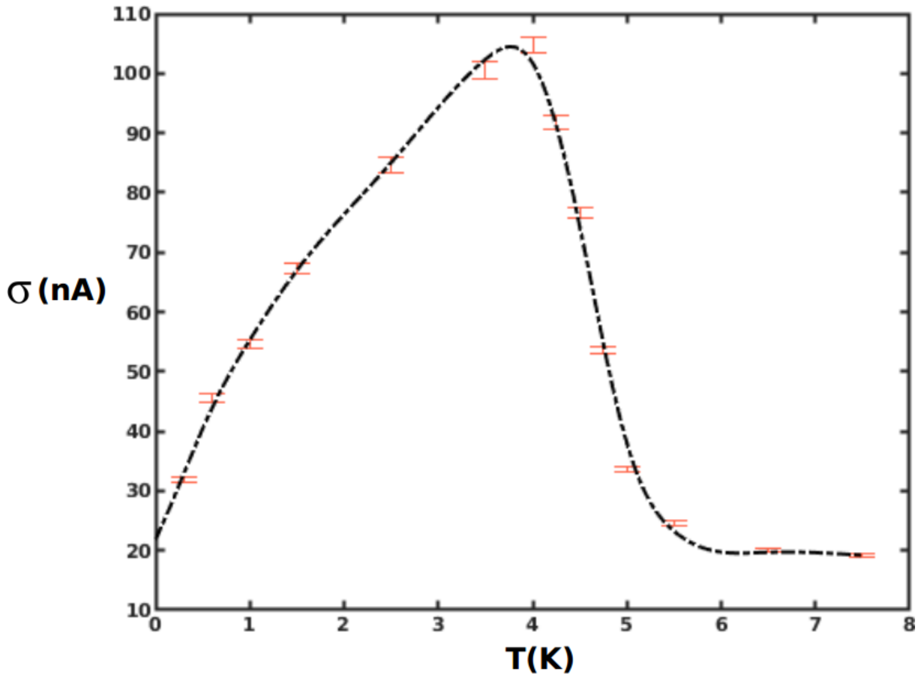

Figure 4.8: $\sigma(T)$ of the experimental switching current distributions for the NbN-GdN-NbN junction. The errors have been calculated using the eq. 4.7. The black line has been obtained with spline interpolation and is a guide for the eyes.

As we have already pointed in the Chapter 2, $\sigma(T)$ shows the typical behaviour of moderately damping Josephson junctions: $\sigma(T)$ increases up to $T^* \simeq 3.8K$ as $T^{2/3}$. Then the curve starts to fall and tends to saturate above $T \simeq 5.5K$.
The transition between different regimes can be analyzed also considering the third moment of a distribution, the *skewness*, defined as [75]:

$$\mu = \frac{1}{\sigma^3} \sum_i^N p_i (I_i - I_m)^3 \tag{4.8}$$

that describes the asymmetry of the curve.
In fig. 4.9 we show the behaviour of $\mu(T)$ calculated starting from the experimental switching distributions. As we can see in the *thermal regime*, below T^*, μ is around -1, as expected from considerations reported in Chapter 2. Around T^*, μ becomes less negative, reaching the maximum value for $T \simeq 4.5K$. This indicates the presence of phase diffusion, that occurs for temperatures above T^*. At highter temperatures the $\mu(T)$ reaches a constant value around -0.2.

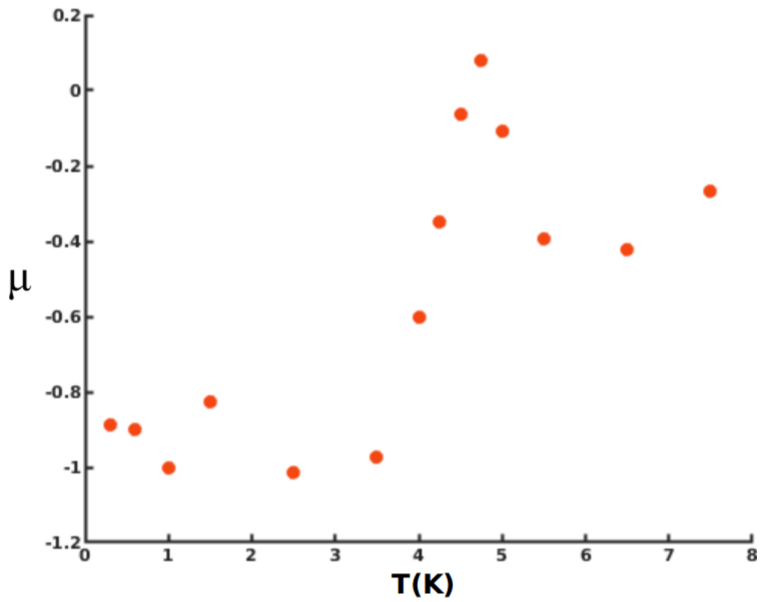

Figure 4.9: $\mu(T)$ of the experimental switching current distributions in NbN-GdN-NbN junction

4.5 Numerical Simulations

Monte Carlo simulations of phase dynamics have been performed starting from the *RCSJ* model in presence of thermal fluctuations:

$$i = \frac{d^2\phi}{d\tau^2} + \frac{1}{Q}\frac{d\phi}{d\tau} + sin(\phi) + i_n \tag{4.9}$$

The fitting of the switching current distributions as a function of T allows to determine the damping factor Q in order to have a good agreement with the experimental curves in fig. 4.7, 4.8 and 4.9. For this purpose we have realized a C-code, using a *Runge Kutta* integrator (see Appendix E) to solve numerically eq. 4.9 and the C function *RAND()* to simulate the noise currents i_n.
Simulations have been performed for a normalized time $N \equiv 1 \times 10^7$, that corresponds to about 10^6 plasma periods. To have a good resolution on the motion of the phase particle [55] we have fixed the time step to $dt = 0.1$.
Observation time for each point generated in the I-V characteristics is 2×10^4 time units, which is long enough to ensure that the average time spent in running/zero voltage state does not vary as a function of the observation time [55].
The multiplicity of switching modes between the running and the trapped states raises a problem of how to define an escape event. In our simulations,

the condition to define the switch is $V(i,T) \geq V(i,0)/2$, where V represents the average velocity of the phase particle in the washboard potential. In other words, the particle spends in the running state more than 50% of the observation time [76]. To obtain the switching distribution we have simulated 5000 escape events, which is similar to the number of counts experimentally measured. Simulations have been performed on the INFN machine *Keplero*. The code is reported in Appendix E.
We have run the simulations at the same temperature T of the experimental measurements, choosing as fitting parameters the damping factor Q and the critical current $I_{c0}(T)$ (defined as the current in absence of thermal fluctuations, such as in the Chapter 2) as we will discuss in the following paragraphs.

4.5.1 Q(T) in Monte Carlo simulations

The damping factor Q gives information on some important parameters that characterize the dynamics of the junction such as the resistance R , the capacitance C and the plasma frequency ω_p.
As we have anticipated in Chapter 2, Q may contain frequency-dependent contributions from the bias circuitry in addition to the intrinsic value of the junction [46]. This is confirmed by the work of Kautz and Martinis [55]: they showed that the phase dynamics of the junction is also determined by the external circuit that loads the junction. To include these effects they added to the $RCSJ$ circuit a shunt composed of a resistor R_s, its associated Johnson noise source I_{n2} and a capacitor C_b, as shown in fig. 4.10. In this

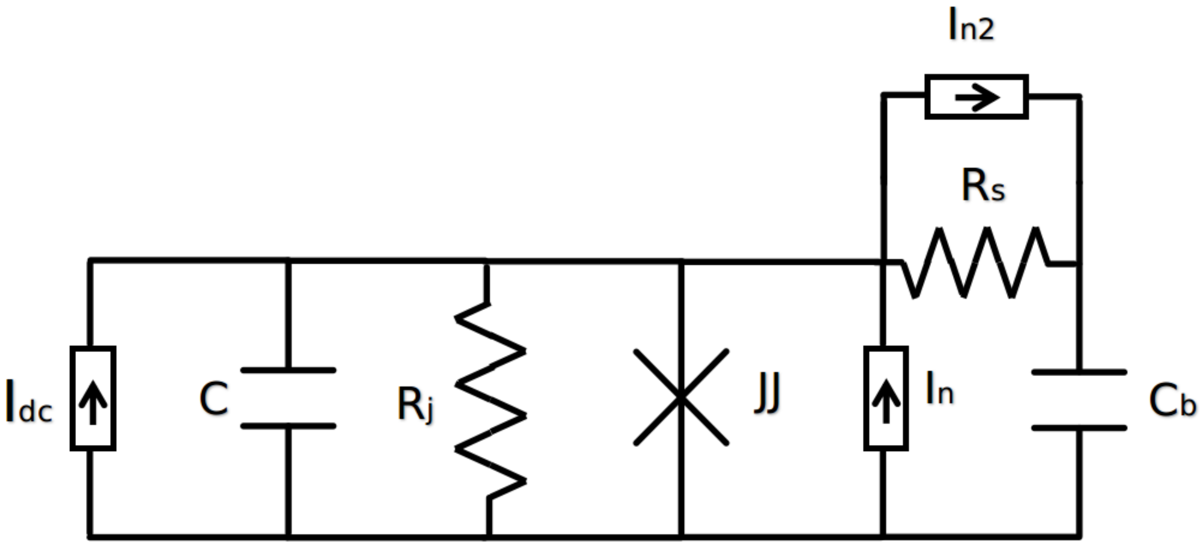

Figure 4.10: Kautz and Martinis junction model [55]

new scheme, the damping depends on the frequency of the phase particle oscillations as:

$$Q(\omega) = \left(\frac{2eIcC}{\hbar G^2(\omega)}\right)^{1/2} \tag{4.10}$$

where:

$$G(\omega) = \frac{1 + (R_j/R_{||})R_s^2 C_b^2 \omega^2}{R_j(1 + R_s^2 C_b^2 \omega^2} \tag{4.11}$$

is the real part of the admittance shunting the ideal Josephson element. Here $R_{||}$ is the parallel combination of R_J and R_S.
The behaviour of eq. 4.10 is shown in fig. 4.11 where we have introduced the factor $Q_0 \equiv \omega_p C R_j$ and $Q_1 = \omega_p C R_{||}$. We can see that for $\omega \sim \omega_p$ the

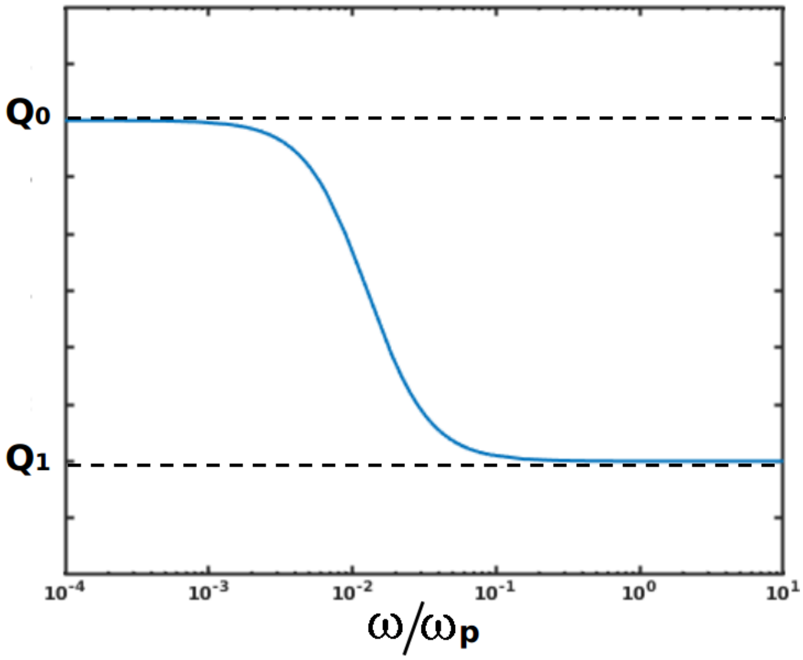

Figure 4.11: Behaviour of the eq. 4.10. The frequency ω is normalized to the plasma frequency $\omega_p = \sqrt{2eI_{c0}/\hbar C}$

damping is determined by Q_1, i.e. by $R_{||}$ while for $\omega \ll \omega_p$ $Q \simeq Q_0$. In the study of the switching events in the superconducting state the phase particle oscillates with a frequency $\omega \sim \omega_p$ [53]: the dynamics is determined by $Q1$, i.e. $R_{||}$.
Originally the Kautz and Martinis's model was introduced because several experimental studies revealed a new kind of I-V characteristic that exhibits both hysteresis and a small voltage associated with the nominal zero-voltage branch [55]. As pointed out by Ono et al. [80], this (I-V) characteristic

cannot be explain within the RCSJ model if frequency dependent damping is not taken into account. In our work we have performed simulation with

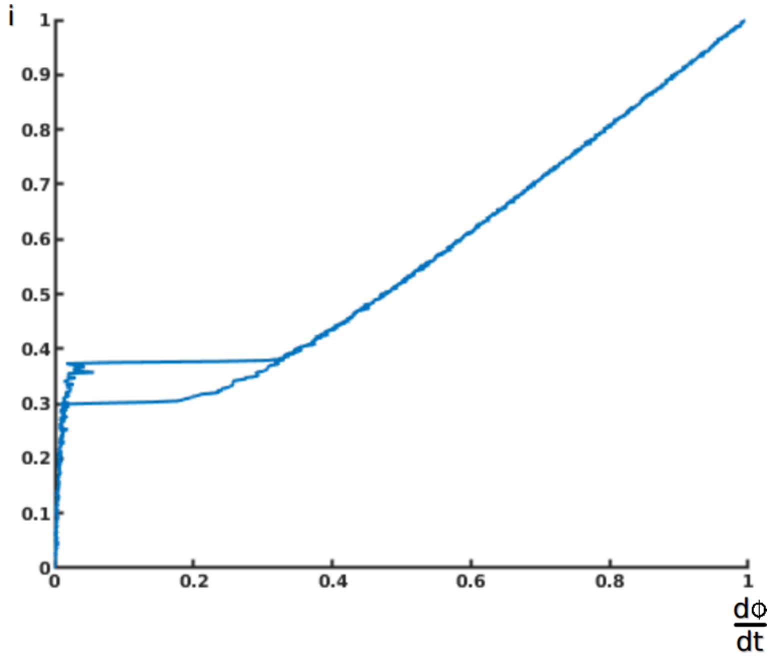

Figure 4.12: Numerical solution of the circuit in fig. 4.10 with $Q_0 = 7$, $Q_1 = 0.4$, $I_{c0} = 1\mu A$ and $T = 2K$. As we can see a finite voltage appears in the superconducting branch while the curve remains hysteretic

a single-Q model to fit the experimental switching current distributions histograms instead of using the complete Kautz and Martinis's model . This is a common procedure in moderately damping junctions and works well when the condition $E_j/(k_bT) > 1$ is satisfied, with $E_j = \hbar I_{c0}/2e$ and the quality factor is larger than 1, such as in our case [81].

4.5.2 I$_c$(T) in Monte Carlo simulations

As well as the damping factor Q, simulations have been performed choosing as parameters the critical currents $I_{c0}(T)$, which is the current at which the junction pass to the resistive state in the absence of current noise I_n. These parameters, with the temperature T, determines the noise width of i_n as discussed in Chapter 2.
Because there isn't a microscopic model that provides the unconventional experimental behaviour of the $I_{c0}(T)$ reported in Section 4.2, we have resorted the phenomenological model reported in ref. [76] [53].

The $I_{c0}(T)$ values influence the damping factor Q. By definition, in fact, Q depends on the critical current by the relation:

$$Q = RC\left(\frac{2e}{\hbar}\frac{I_{c0}}{C}\right)^{1/2} \equiv kI_{c0}^{1/2} \tag{4.12}$$

In our simulations, we have decided to consider the value of Q at $T = 4K$ to label the simulations, where the maximum width of the experimental switching distribution occurs; the values at the other temperatures can be obtained starting from the eq. 4.12.

4.6 Determination of the electrodynamic parameters of the junction

From the comparison between the simulated distributions and the experimental ones, the damping factor Q in better agreement with the experimental data is $Q = 3.5 \pm 0.1$. In fig.4.13 and in fig. 4.14 we have compared the $I_m(T)$ and $\sigma(T)$ behaviour in the experimental and simulated cases. The

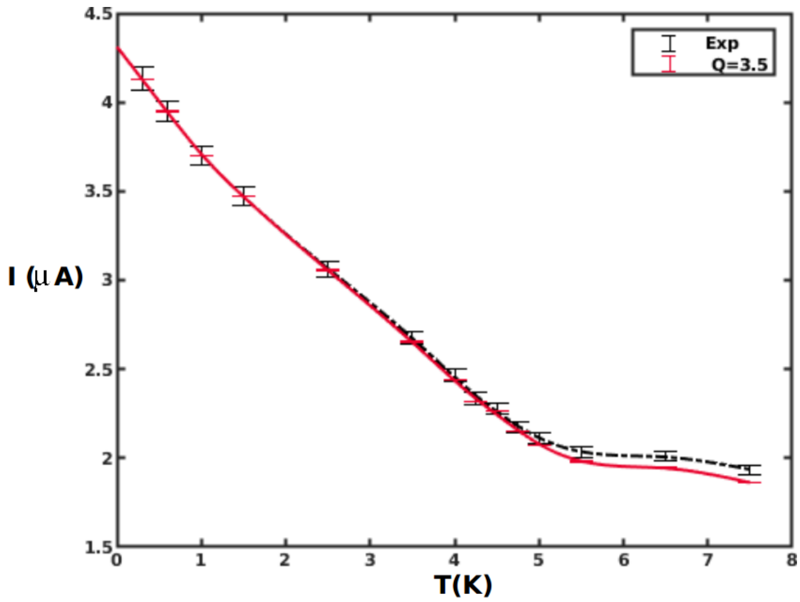

Figure 4.13: behaviour of $I_m^{exp}(T)$ and $I_m^{sim}(T)$. Bars represent the error of the points. The lines have been obtained with spline interpolation and is a guide for the eyes

method to determine $I_m^{sim}(T)$ allows us to obtain a good agreement with the experimental $I_m^{exp}(T)$, as we can see in fig. 4.13. The *RCSJ* model that we

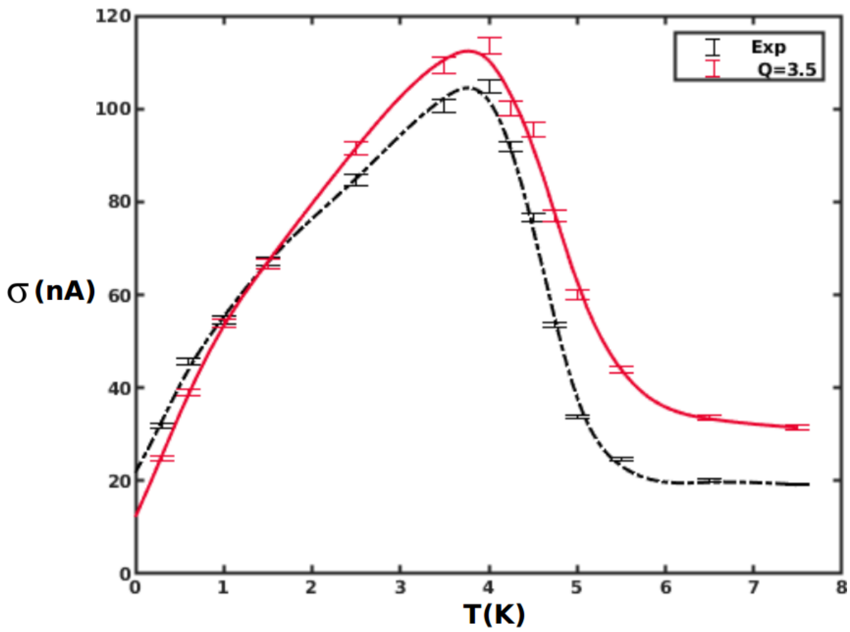

Figure 4.14: behaviour of $\sigma_{exp}(T)$ and $\sigma_{sim}(T)$. Bars represent the error of the points. The lines have been obtained with spline interpolation and is a guide for the eyes

have adopted in our simulations, doesn't include the magnetic effects of the barrier, but nevertheless, it provides a good agreement with some experimental key quantities such as the temperature T^* (see fig. 4.14).
The damping factor Q confirms that our junction is in moderately damping regime.
We have compared the experimental distributions with the simulated one as shown in fig 4.15. The curves are in good agreement at low temperatures while they have some differences above $T \simeq 5K$, due to the simplest model that we have used to perform simulations. If we consider the junction as a parallel plate condenser, we can calculate the capacitance starting from the equation :

$$C = \epsilon \frac{A}{d} \tag{4.13}$$

Here A is the area of the junction, d is its thickness and $\epsilon = 2.3410^{-10} F/m$ is the absolute permittivity of the GdN barrier [78]. We obtain:

$$C = (3.8 \pm 0.6)pF \tag{4.14}$$

and considering the eq. 4.12 for the damping factor Q we can calculate the resistance R:

$$R = (16 \pm 2)\Omega \tag{4.15}$$

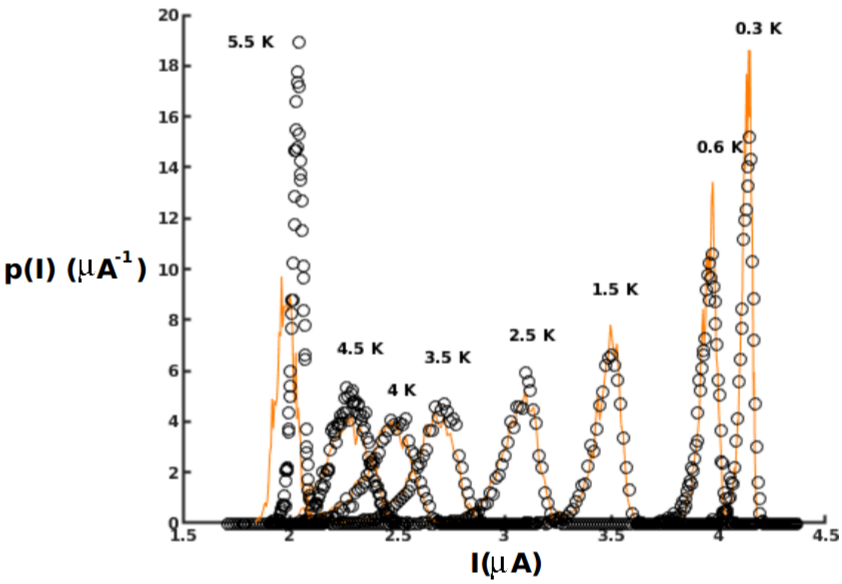

Figure 4.15: Comparison between the switching current distributions simulated (orange line) and experimetal (black dot points) at different temperature

This value is consistent with the order of magnitude of the external circuity resistance, i.e. some tens of Ohm, and it is similar to what reported in previous works in which junctions with similar electrodynamic properties have been analyzed [58] [53] [79]. We can conclude that dissipation in NbN-GdN-NbN junction at high frequency is determined by the environment in which the junction is embedded, while in common *SFS* device the damping strictly depends on the parameters [55] of the intrinsic junction. The clear advantage is that, for possible applications in superconducting electronics, spintronics and quantum circuits, the dissipation can be tuned by adjusting the overall circuity while in *SFS* junction Q is fixed by the intrinsic characteristics of the devices.
The capacitance C and the damping factor Q determine the value of the plasma frequency ω_p, which describes the motion of the phase particle in a minimum of the washboard potential. We have found that ω_p is around 32 GHz, a typical value in a moderately damping junctions [6] [55] [53]. The plasma frequency characterizes the behaviour of the junction in the quantum regime. It brings information on the energy scale of the system and on the different role that the charge and Josephson energy have in the transport characteristics [52]. Considering the expression [53]:

$$T_{cross} = \frac{\hbar\omega_p}{2\pi k_B}\left\{\left[1+\left(\frac{1}{4Q^2}\right)\right]^{1/2} - \frac{1}{2Q}\right\} \tag{4.16}$$

we can calculate the transition temperature between the quantum and thermal regime:

$$T_{cross} = (50 \pm 10)mK \tag{4.17}$$

which is in good agreement with the experimental value of $T_{cross} \simeq 70mK$ [6]. The result is remarkable since T_{cross} has been determined by using two independent measurements, thus confirming the self-consistency of the whole approach.

Conclusions

In this work we have investigated the properties of unconventional Josephson junctions composed of two NbN superconducting electrodes separated by an insulating ferromagnetic barrier of GdN. These junctions fall in the very interesting family of junctions combining the potentials of superconductivity and magnetism. These junctions offer the additional advantage of being tunnel devices, and also they have been suggested as potential candidates to observe triplet supercurrents [7] [8].
I have fully characterized the transport properties of the junction with the barrier thickness of 3 nm. I have studied the unconventional features introduced by the ferromagnet starting from the exotic dependence of the critical current on the temperature and on the magnetic field. The presence of an intrinsic magnetization determines hysteresis in the Fraunhofer patter and a spin-polarized current with an efficiency around the 95%, below the Curie temperature of the ferromagnet, i.e $\simeq 35K$.
In particular, I have investigated the effects of thermal noise on the NbN-GdN-NbN junction in the thermal regime. Comparing the experimental switching current distributions and Monte Carlo simulations, I have determined the fundamentals electrodynamic parameters of the junction, which define the transport characteristics of the system. These parameters are not accessible by using direct measurements, therefore reliable methods and analysis to estimate quality factor Q, capacitance C and resistance R associated to the junction circuit represent a fundamental step to engineering such unconventional junctions. This is one of the very first studies on the electrodynamics of junctions using ferromagnetic or ferro-insulator barrier in which, differently from SFS structures, the conduction is mostly determined by the circuit loading the device.
The junctions I have analyzed are of great interest for technological applications. The presence of hysteresis in the Fraunhofer pattern provides a method to develop cryogenic memory, taking advantage of the presence of two possible I_c value at a fixed magnetic field $\vec{H}$.
The junction with the barrier thickness of 3 nm shows MQT (Macroscopic

Quantum Tunneling) at low temperatures [6] with interesting magnetic features and low dissipation contributing to set its potential for applications in superconducting electronics. For this aim, the study I have performed provides also information on the interaction with the external environment and can be used to characterize similar junctions for the development of new devices.

Appendix A

The London model

In an ordinary conductor with n electrons per unit volume with effective mass m, the motion of the electrons in presence of an electric field $\vec{E}$ is described in the Drude's theory by the dynamic equation:

$$m\frac{d\vec{v}}{dt} = -m\frac{\vec{v}}{\tau} + q\vec{E} \tag{A.1}$$

where $q = (-e)$ is the charge of the electrons and τ is a relaxation time, related to the scattering of this particles with impurities, phonons, and other defects [13].
If we imagine a superconductor as an ideally pure metal, with $\tau \to \infty$, the eq A.2 becomes :

$$m\frac{d\vec{v}}{dt} = +q\vec{E} \tag{A.2}$$

In terms of the current density $\vec{J}$:

$$\vec{J} = nq\vec{v} \tag{A.3}$$

the eq. A.2 can be written as:

$$\frac{\partial\vec{J}}{\partial t} = \frac{nq^2}{m}\vec{E} \tag{A.4}$$

known as the *first London equation.* This classical equation describes the dynamics of collisionless electrons and is simply a modification of the Ohm law [11].
To derive the *second London equation*, let's apply the curl-operator to both members of A.4:

$$\frac{\partial}{\partial t}\left(\nabla \times \vec{J}\right) = \frac{nq^2}{m}\nabla \times \vec{E} \tag{A.5}$$

Considering the third Maxwell's equation:

$$\nabla \times \vec{E} = -\frac{1}{c}\frac{\partial \vec{B}}{\partial t} \tag{A.6}$$

the eq. A.5 could be written as:

$$\frac{\partial}{\partial t}\left(\nabla \times \vec{J}\right) = -\frac{nq^2}{mc}\frac{\partial \vec{B}}{\partial t} \Longrightarrow \frac{\partial}{\partial t}\left(\nabla \times \vec{J} + \frac{nq^2}{mc}\vec{B}\right) = 0 \tag{A.7}$$

This is a general equation valid for any *ideal conductor*, because it has been obtained starting from the eq. A.4; but alone does not account for the *Meissner effect*. In fact A.5 shows that the vectorial field

$$\vec{V} = \nabla \times \vec{J} + \frac{nq^2}{mc}\vec{B} \tag{A.8}$$

is constant in time, but this argument is not sufficient to establish whether fields and currents can penetrate or not in the interior of the sample.
It has been pointed out by the London brothers that, if the quantity in A.8 is not only time-independent but actually vanishes identically, then the ideal perfect conductor also exhibits the *Meissner effect*.
The equation:

$$\nabla \times \vec{J} + \frac{nq^2}{mc}\vec{B} = 0 \tag{A.9}$$

is called *second London equation*.
The eq. A.9 implies that a superconductor in stationary condition cannot sustain a magnetic field in its interior, except for a thin surface layer [11]. This can be obtained as follow: in *stationary conditions*, the magnetic field is related to the current density by the *fourth Maxwell equation*:

$$\nabla \times \vec{B} = \frac{4\pi}{c}\vec{J} \tag{A.10}$$

We can apply the curl-operator to both sides of eq. A.10:

$$\nabla \times \left(\nabla \times \vec{B}\right) = \frac{4\pi}{c}\left(\nabla \times \vec{J}\right) = -\frac{4\pi n_s e^2}{mc^2}\vec{B} \tag{A.11}$$

where the last equality in eq. A.11 is obtained using the eq. A.9
Because :

$$\nabla \times \left(\nabla \times \vec{B}\right) = \nabla\left(\nabla \cdot \vec{B}\right) - \nabla^2\vec{B} \tag{A.12}$$

and:

$$\nabla \cdot \vec{B} = 0 \tag{A.13}$$

for the *second Maxwell equation*, the eq. A.11 reduces to:

$$\nabla^2 \vec{B} = -\frac{4\pi n_s e^2}{mc^2}\vec{B} \equiv -\frac{1}{\lambda_L^2}\vec{B} \tag{A.14}$$

where we have defined the *London penetration length* λ_L as :

$$\lambda_L = \sqrt{\frac{mc^2}{4\pi n_s e^2}} \tag{A.15}$$

The solution of the eq. A.14 is an exponential decay of $\vec{B}$ from the surface towards the interior, over the characteristic distance λ_L.

Appendix B

Bogoliubov-de Gennes equations in BCS theory

The *BCS theory* is based essentially on two assumptions: (i) attractive electron–electron interaction in a conductor leads to (Cooper) pairing and (ii) this pairing can be described in a mean-field theory. In the language of second-quantized field operators, the attractive electron–electron interaction can be described with a Hamiltonian of the form [2]:

$$\hat{H} = \sum_{\sigma} \int d\vec{r}\; \hat{\Psi}^{\dagger}_{\sigma}(\vec{r}) H_0 \hat{\Psi}_{\sigma}(\vec{r}) + \sum_{\sigma\sigma'} \int d\vec{r} d\vec{r}'\; \lambda_{\sigma,\sigma'}(\vec{r},\vec{r}') \hat{\Psi}^{\dagger}_{\sigma}(\vec{r}) \hat{\Psi}^{\dagger}_{\sigma'}(\vec{r}') \hat{\Psi}_{\sigma'}(\vec{r}') \hat{\Psi}_{\sigma}(\vec{r}) \tag{B.1}$$

where:

$$H_0 = \frac{1}{2m}\left(\frac{\hbar}{i}\vec{\nabla} - e\vec{A}\right)^2 + U(\vec{r}) - \mu \tag{B.2}$$

is the single-particle Hamiltonian of the system and $\hat{\Psi}_{\sigma}(\vec{r})$ and $\hat{\Psi}^{\dagger}_{\sigma}(\vec{r})$ are the many-body operator that annihilates and creates respectively an electron in the position $\vec{r}$ with spin σ. The factor $\lambda_{\sigma,\sigma'}(\vec{r},\vec{r}')$ is the term of interaction between the electrons.
In the BCS approximation the electrons that form the Cooper pairs are in the singlet state,i.e the interaction is established between electrons with the same spin:

$$\lambda_{\sigma,\bar{\sigma}}(\vec{r},\vec{r}') = \lambda(\vec{r})\delta_{\sigma,\bar{\sigma}} \tag{B.3}$$

In the same way we consider the *free electron approximation*, i.e H_0 is in the form :

$$H_0 = \frac{\hbar^2 \nabla^2_{\vec{r}}}{2m} \tag{B.4}$$

that is the simplest way to describe charge carriers in a metallic solid [13]. We can make the substitution in the Hamiltonian B.1 :

$$\begin{aligned}\hat{\Psi}_{\bar{\sigma}}(\vec{r}')\hat{\Psi}_{\sigma}(\vec{r}) &= F(\vec{r}) + \hat{\delta}_{\bar{\sigma}\sigma}(\vec{r})\\ \hat{\Psi}^{\dagger}_{\bar{\sigma}}(\vec{r}')\hat{\Psi}^{\dagger}_{\sigma}(\vec{r}) &= F^{*}(\vec{r}) + \hat{\delta}^{\dagger}_{\bar{\sigma}\sigma}(\vec{r})\end{aligned} \tag{B.5}$$

where :

- $F(\vec{r}) \equiv < \hat{\Psi}_{\bar{\sigma}}(\vec{r}')\hat{\Psi}_{\sigma}(\vec{r}) >$ is the statistical average [1] of $\hat{\Psi}_{\bar{\sigma}}(\vec{r}')\hat{\Psi}_{\sigma}(\vec{r})$. It' s important to note that $F(\vec{r})$ measures the correlations between the pairs of electrons.
  Gork'ov showed that $F(\vec{r})$ is proportional to the order parameter ψ introduced in the Gizburg Landau's theory [16].
- $\hat{\delta}_{\bar{\sigma}\sigma}(\vec{r})$ describes the fluctuations around the mean value and satisfies $< \hat{\delta}_{\bar{\sigma}\sigma}(\vec{r}) >= 0$.

Assuming that these fluctuations are small, one can expand the equation B.1 into the fist order in $\hat{\delta}$:

$$\hat{H} \simeq \sum_{\sigma} \int d\vec{r}\, \hat{\Psi}^{\dagger}_{\sigma}(\vec{r}) H_0 \hat{\Psi}_{\sigma}(\vec{r}) + \int d\vec{r}\, \Delta(\vec{r})\Psi^{\dagger}_{\sigma}(\vec{r})\hat{\Psi}^{\dagger}_{\bar{\sigma}}(\vec{r}) + \Delta(\vec{r})^{*}\hat{\Psi}_{\sigma}(\vec{r})\hat{\Psi}_{\bar{\sigma}}(\vec{r}) - E_0 \tag{B.7}$$

where $\Delta(\vec{r}) \equiv \lambda(\vec{r})F(\vec{r})$.
To diagonalize this one can introduce the *Bogoliubov transformation* [9]:

$$\begin{aligned}\hat{\Psi}_{\uparrow}(\vec{r}) &= \sum_{n} \hat{\gamma}_{n\uparrow}u_n(\vec{r}) - \hat{\gamma}^{\dagger}_{n\downarrow}v^{*}_{n}(\vec{r})\\ \hat{\Psi}_{\downarrow}(\vec{r}) &= \sum_{n} \hat{\gamma}_{n\downarrow}u_n(\vec{r}) + \hat{\gamma}^{\dagger}_{n\uparrow}v^{*}_{n}(\vec{r})\end{aligned} \tag{B.8}$$

where u_n and v_n are position-dependent eigenfunctions to be determined so as to diagonalize the Hamiltonian [2]. The fermion operators $\hat{\gamma}_{n\alpha}$ and $\hat{\gamma}^{\dagger}_{n\alpha}$ are called *Bogoliubon operators*: they annihilate and create excitations

[1] In the second-quantized field the statistical average of $\hat{A}$ is defined by

$$< \hat{A} >\equiv tr\Big(\hat{\rho}\hat{A}\Big) \tag{B.6}$$

where tr is the trace operator and $\hat{\rho}$ is the Boltzmann operator from the superconducting state respectively. In this way one can obtain the diagonalized Hamiltonian :

$$\hat{H} = E_G + \sum_{\alpha,n} \epsilon_n \hat{\gamma}^\dagger_{n\alpha} \hat{\gamma}_{n\alpha} \tag{B.9}$$

where E_g is the energy of the ground states, while ϵ_n is an energy of the excitation in the state n.
One can calculate the commutators $[\hat{H}, \hat{\Psi}_\uparrow(\vec{r})]$ and $[\hat{H}, \hat{\Psi}_\downarrow(\vec{r})]$ using the relations:

$$[\hat{\Psi}_\alpha(\vec{r}), \hat{\Psi}_\beta(\vec{r}')] = 0 \tag{B.10}$$

$$[\hat{\Psi}^\dagger_\alpha(\vec{r}), \hat{\Psi}^\dagger_\beta(\vec{r}')] = 0 \tag{B.11}$$

$$[\hat{\Psi}_\alpha(\vec{r}), \hat{\Psi}^\dagger_\beta(\vec{r}')] = \delta_{\alpha\beta}\delta(r - r') \tag{B.12}$$

and the properties (from equation B.9)

$$[\hat{H}, \hat{\gamma}_{n\alpha}] = -\epsilon_n \hat{\gamma}_{n\alpha} \tag{B.13}$$

$$[\hat{H}, \hat{\gamma}^\dagger_{n\alpha}] = \epsilon_n \hat{\gamma}^\dagger_{n\alpha} \tag{B.14}$$

and obtain the *Bogoliubov -de Gennes equations* (BdGE) for the eigenfunctions u_n and v_n:

$$\begin{aligned} (H_0 - \lambda(\vec{r}))u_n(\vec{r}) + \Delta(\vec{r})v_n(\vec{r}) &= \epsilon_n u_n(\vec{r}) \\ -(H_0^* - \lambda(\vec{r}))v_n(\vec{r}) + \Delta^*(\vec{r})u_n(\vec{r}) &= \epsilon_n v_n(\vec{r}) \end{aligned} \tag{B.15}$$

If $\Delta(\vec{r}) = 0$ the equations B.15 decouples in the form:

$$\begin{aligned} H_0 u_n(\vec{r}) &= \epsilon_n u_n(\vec{r}) \\ H_0^* v_n(\vec{r}) &= -\epsilon_n v_n(\vec{r}) \end{aligned} \tag{B.16}$$

so that u_n and v_n are the ordinary electron and hole eigenfunctions of the normal state, with energies $\pm\epsilon_n$ relative to the Fermi energy [2].
In the case where $\Delta = |\Delta|e^{i\chi}$ is constant in space and the magnetic field is absent, as in the case of a bulk superconductor, the BdGE have the form:

$$\begin{aligned} \left(-\frac{\hbar^2}{2m}\nabla^2 - \mu\right)u_n(\vec{r}) + \Delta v_n(\vec{r}) &= \epsilon_n u_n(\vec{r}) \\ -\left(-\frac{\hbar^2}{2m}\nabla^2 - \mu\right)v_n(\vec{r}) + \Delta^* u_n(\vec{r}) &= \epsilon_n v_n(\vec{r}) \end{aligned} \tag{B.17}$$

where $\mu = \hbar^2 k_F^2/2m$. In a bulk system the solutions can typically be written in terms of plain waves:

$$u_n(\vec{r}) = \frac{1}{\sqrt{V}} e^{i\chi} U_n e^{i\vec{n}\vec{r}} \,,\; v_n(\vec{r}) = V_n \frac{1}{\sqrt{V}} e^{i\vec{n}\vec{r}} \tag{B.18}$$

Replacing the eq. B.18 in B.17, one obtains:

$$\begin{aligned} \xi_n U_n + |\Delta| V_n &= \epsilon_n U_n \\ -\xi_n V_n + |\Delta| U_n &= \epsilon_n V_n \end{aligned} \tag{B.19}$$

where $\xi_n = \frac{\hbar^2}{2m}[n^2 - k_F^2]$. The condition of resolvability of B.19 gives:

$$\epsilon_n = \pm\sqrt{\xi_n^2 + |\Delta|^2} \tag{B.20}$$

and the solution is :

$$\begin{aligned} U_n &= \frac{1}{2}\left(1 + \frac{\xi_n}{\epsilon_n}\right)^{1/2} \\ V_n &= \frac{1}{2}\left(1 - \frac{\xi_n}{\epsilon_n}\right)^{1/2} \end{aligned} \tag{B.21}$$

The energy $|\Delta|$ is the lowest single-particle excitation energy in the superconducting state while $2|\Delta|$ corresponds to an energy which is needed to destroy a Copper pair.
By definition:

$$\Delta(\vec{r}) \equiv \lambda(\vec{r}) < \hat{\Psi}_{\bar{\sigma}}(\vec{r}')\hat{\Psi}_{\sigma}(\vec{r}) >= \lambda(\vec{r}) \sum_n (1 - 2f_n) u_n(\vec{r}) v_n^*(\vec{r}) \tag{B.22}$$

where f_n is the distribution function of the electrons. The last equality comes from the definitions B.8 and considering the statistical average of the *Bogoliubon operators* :

$$< \gamma_{n\alpha}^\dagger, \gamma_{m\beta} >= \delta_{nm}\delta_{\alpha\beta} f_n \tag{B.23}$$

$$< \gamma_{n\alpha}^\dagger, \gamma_{m\beta}^\dagger >=< \gamma_{n\alpha}, \gamma_{m\beta} >= 0 \tag{B.24}$$

where f_n is the *Fermi-Dirac distribution.*
In this way one can self-consistently calculate $\Delta(\vec{r})$ using the eqs. B.22 and B.18:

$$u_n(\vec{r}) v_n^*(\vec{r}) = \frac{\Delta}{2\epsilon_n} \tag{B.25}$$

In particular Δ is T-dependent and for $T \to T_c$ (and $T < T_c$) the form of $\Delta(T)$ is found to be [11]:

$$\Delta(T) = 3.06 k_b T_c \left(1 - \frac{T}{T_c}\right)^{1/2} \tag{B.26}$$

In the case of $\Delta(\vec{r}) = const$, because u_n and v_n are plane waves, one can rewrite the field operators as:

$$\hat{\Psi}_\uparrow = \sum_n \frac{1}{\sqrt{V}} e^{i\vec{n}\vec{r}} \hat{c}_{n\uparrow} \tag{B.27}$$

$$\hat{\Psi}_\downarrow = \sum_n \frac{1}{\sqrt{V}} e^{i\vec{n}\vec{r}} \hat{c}_{n\downarrow} \tag{B.28}$$

and likewise for $\hat{\Psi}^\dagger_\uparrow$ and $\hat{\Psi}^\dagger_\downarrow$. Comparing eq. B.8 with B.27 one can obtain the following relations [2]:

$$\hat{c}_{n\uparrow} = u^*_n \hat{\gamma}_{n\downarrow} + v_n \hat{\gamma}^\dagger_{n\uparrow} \tag{B.29}$$

$$\hat{c}^\dagger_{-n\uparrow} = -v^*_n \hat{\gamma}_{n\downarrow} + u_n \hat{\gamma}^\dagger_{n\uparrow} \tag{B.30}$$

where the operators $\hat{c}^\dagger_{n\uparrow}$ and $\hat{c}_{n\uparrow}$ create and annihilate an electron with momentum $\hbar k$ respectively [11]. In the new base, the state of the superconductor can be written:

$$|\psi_\phi\rangle_{BCS} = \prod_n (|u_n| + |v_n| e^{i\phi} c^\dagger_{n\uparrow} c^\dagger_{-n\downarrow})|0\rangle \tag{B.31}$$

where $|0\rangle$ is the vacuum state with no particles present. Evidently, this expression can be expressed as a sum:

$$|\psi_\theta\rangle = \sum_m \lambda_m |\psi_m\rangle \tag{B.32}$$

where each term represent the part of the expansion of the product form B.31 containing $N/2$ pairs [2]. We can project out this $|\psi_m\rangle$ by simply multiply by $e^{-iN\theta/2}$ and integrating on θ over 2π because the members of the $|\psi_m\rangle$ are identified by a common phase factor $e^{iN\theta/2}$. by integrating over all values of θ, i.e, by making θ completely uncertain, we have enforced a precise specification of the number N. On the other hand, with θ fixed as in B.31, there is a indetermination on the number of particles.
These results illustrate the uncertainty [21]:

$$\Delta N \Delta\theta \leq 2\pi \tag{B.33}$$

Appendix C

Anderson description of a Josephson junction

In order to diagonalize the Hamiltonian B.1, one can calculate using 1.24 the element $\langle N_L - p', N_R + p' | H | \psi \rangle$. The result is:

$$Ec_{p'} = 2c_{p'}E_0 - tc_{p'+1} - tc_{p'-1} \tag{C.1}$$

where E is the energy of the whole system and for simplicity $E_0 \equiv E_R \equiv E_L$. Making the position $c_{p'} = e^{ip'\phi}$, the eq. C.1 becomes:

$$E = 2(E_0 - tcos(\phi)) \tag{C.2}$$

Substituting in 1.22 $c_p = e^{ip\phi}$ the state of the system becomes:

$$|\psi\rangle = \sum_p e^{ip\phi} |N_L - p\rangle |N_R + p\rangle \tag{C.3}$$

One can define $N_L - p \to N'_L$ and $N_R + p \to N'_R$ with:

$$N'_L + N'_R = N \tag{C.4}$$

$$N'_R - N'_L = 2p \tag{C.5}$$

and obtain:

$$|\psi\rangle = \sum_{N'_R, N'_L} \delta_{N'_R + N'_L, N} \, e^{i\frac{N'_R - N'_L}{2}\phi} |N'_L\rangle |N_R\rangle \tag{C.6}$$

Now two properties we have to consider. The first is that in a superconductor N and ϕ are conjugate variables (with $\alpha \equiv R, L$):

$$|N_\alpha\rangle = \int_0^{2\pi} \frac{d\theta_\alpha}{2\pi} e^{-i\frac{N_\alpha}{2}\theta_\alpha} |\theta_\alpha\rangle \Longleftrightarrow |\theta_\alpha\rangle = \sum_n e^{i\frac{N_\alpha}{2}\theta_\alpha} |N_\alpha\rangle \tag{C.7}$$

The second is that the δ-function can be expressed in the form:

$$\delta_{N,N'} = \int_0^{2\pi} \frac{d\theta}{2\pi} e^{i(N-N')\theta} \tag{C.8}$$

Substituting in the eq. C.6 we have :

$$\begin{aligned} |\psi\rangle &= \sum_{N'_R,N'_L} \int_0^{2\pi} \frac{d\theta}{2\pi} e^{i(N'_R+N'_L-N)\theta}\ e^{i\frac{N'_R-N'_L}{2}\phi} |N'_L\rangle|N'_R\rangle \\ &= \sum_{N'_R,N'_L} \int_0^{2\pi} \frac{d\theta}{2\pi} e^{iN\theta}\ e^{iN'_R(\theta_R+\frac{\phi}{2})} e^{iN'_L(\theta_L-\frac{\phi}{2})} |N'_L\rangle|N'_R\rangle \\ &= |\psi\rangle = \int_0^{2\pi} e^{-iN\phi} \frac{d\theta}{2\pi} |\theta_L - \frac{\phi}{2}\rangle|\theta_R - \frac{\phi}{2}\rangle \end{aligned} \tag{C.9}$$

Appendix D

Microscopic model of a Josephson junction

For finite voltage situations involving the ac Josephson effect, a more complete description is required respect to the one used in Section .
From a quantum mechanical point of view, in BCS approximation, a tunneling junction is usually described by the Hamiltonian 1.23:

$$\hat{H} = \hat{H}_R + \hat{H}_L + \hat{H}_T \tag{D.1}$$

Now we use the expression for $\hat{H}_T$ introduced by Cohen et al. [23]:

$$\hat{H}_T = \sum_{kq\sigma} \left(T_{kq\sigma} \hat{c}^{\dagger}_{k\sigma} \hat{d}_{q\sigma} + T^{*}_{kq\sigma} \hat{c}_{k\sigma} \hat{d}^{\dagger}_{q\sigma} \right) \tag{D.2}$$

where $\hat{c}^{\dagger}_{k\sigma}(\hat{c}_{k\sigma})$ create (destroys) one electron with momentum k and spin σ in the left electrode and vice-versa $\hat{d}^{\dagger}_{k\sigma}(\hat{d}_{k\sigma})$ creates (destroys) one electron with momentum q and spin σ in the right electrode.
The tunnel current $I(V,T)$ can be obtained from the expectation value of the rate of change of the electron number of operator $\hat{N}_R = \sum_{k\sigma} = \hat{c}^{\dagger}_{k\sigma}\hat{c}_{k\sigma}$ [4]:

$$I(V,T) = -e < \frac{d\hat{N}_R}{dt} > \tag{D.3}$$

In many-body formalism, the expectation value is defined as:

$$< \dot{N}_R >= \frac{Tr\{e^{-H/k_bT}\}\dot{N}_R}{Tr\{e^{-H/k_bT}\}} \tag{D.4}$$

and can be evaluated using the perturbation theory. In eq D.4 H is the the total Hamiltonian of the system, k_b is the Boltzman costant and the $Tr\{\}$

denotes the trace operator inside the brackets.
In the case in which the electrodes are at the same potential V, as shown by Anderson [21], at the first order in H_T one can obtain the eq. s1.20.
Otherwise, if $\Delta V \neq 0$, there is another channel of transmission characterized by a current:

$$I_{tunnel} = \frac{2\pi}{\hbar}|T|^2 \int_{-\infty}^{\infty} D_L(E) D_R(E) \Big(f_L(E) - f_R(E) \Big) dE \tag{D.5}$$

due to tunnel of quasiparticles [47] .
In eq. D.5 T is the tunneling matrix $T_{k\sigma}$ supposed to be energy-independent; $f_L(f_R)$ is the Fermi factor and $D_L(D_R\ )$ is the density of states in the left (right) metal.
In the hypothesis that D_L and D_R are constant and equal to the density of states at the Fermi energy level and $V \rightarrow 0$, eq. D.5 can be written:

$$I_{tunnel} = \sigma V \tag{D.6}$$

σ can be regarded as a normal conductance: for low applied voltage, the tunnel behaves as an ohmic element [4].
In the case in which $V(t) = V_0$, the eq. D.4 at the first order in H_T gives the following expression for the total current:

$$I_{dc}(V, T, t) = I_{critical}(V, T) sin(\phi(t)) + \sigma V \tag{D.7}$$

Appendix E

Runge-Kutta algorithm

The Runge Kutta algorithm is an efficient method to calculate the solution of differential equations [82] .
A differential equation can be always written in general in the form [77]:

$$\frac{d\vec{y}}{dt} = \vec{f}(\vec{y}, t) \tag{E.1}$$

where $\vec{y}$ is the dynamical variable vector and $\vec{f}$ is the generalized velocity vector, a term borrowed from the definition of the velocity. For semplicity we consider an unidimensional problem where f and y are scalar function
Let an initial value problem be specified as follows:

$$y' = f(t, y),\ y(t_0) = y_0,\ t \in [t_0, t_f] \tag{E.2}$$

Now we can divide the interval of integration with step of size h. In each subintervals, we can write:

$$y_{n+1} = y_n + \frac{1}{6}(k_1 + 2k_2 + 2k_3 + k_4)$$
$$t_{n+1} = t_n + h$$

where $y_n \equiv y(t_0 + nh)$. The k_i coefficients are defined in the following way:

$$k_1 = hf\Bigg(t_n, y_n\Bigg), \tag{E.3}$$

$$k_2 = hf\Bigg(t_n + \frac{h}{2}, y_n + \frac{k_1}{2}\Bigg), \tag{E.4}$$

$$k_3 = hf\Bigg(t_n + \frac{h}{2}, y_n + \frac{k_2}{2}\Bigg), \tag{E.5}$$

$$k_4 = hf\Bigg(t_n + h, y_n + k_3\Bigg). \tag{E.6}$$

Here y_{n+1} is the RK4 approximation of $y(t_{n+1})$, and the next value y_{n+1} is determined by the present value y_n plus the weighted average of four increments, where each increment is the product of the size of the interval, h, and an estimated slope specified by function f on the right-hand side of the differential equation.
We have [77]:

- k_1 is the increment based on the slope at the beginning of the interval, using y (Euler's method);
- k_2 is the increment based on the slope at the midpoint of the interval, using y and k_1;
- k_3 is again the increment based on the slope at the midpoint, but now using y and k_2;
- k_4 is the increment based on the slope at the end of the interval, using y and k_3.

In averaging the four increments, greater weight is given to the increments at the midpoint.
The RK4 method is a fourth-order method, meaning that the local truncation error is on the order of $O(h^5)$ while the total accumulated error is on the order of $O(h^4)$ [82].

Appendix F

Simulations code

In this Appendix we have reported the code used in Monte Carlo simulations.

```
#include<stdio.h>
#include<stdlib.h>
#include<math.h>
#include <time.h>


//funzione per calcolare con i numeri casuali uniformememnte
   distribuiti
double sampleNormal (void) {
  double v1,v2,s;

  do {
    v1 = 2.0 * ((double) rand()/RAND_MAX)   1;
    v2 = 2.0 * ((double) rand()/RAND_MAX)   1;

    s = v1*v1 + v2*v2;
  } while ( s >= 1.0 );

  if (s == 0.0)
    return 0.0;
  else
    return (v1*sqrt( 2.0 * log(s) / s));
}


//calcolo media
double media (double **valori,int period, int index ){
int i;
double m=0;
for(i=0;i<period;i++)
{m=m+valori[index][i];}

```

```
return m/period;

}


// Funzione per runge kutta

double g1 (double v){
double g=v;
return g;
}

double g2 (double x,double v, double Q, double i){
double f= (1/(Q))*v+(i  sin(x));
return f;
}



double min (double *a, int size){
int i;

          double   m=100000;
          for (i=0; i<size; i++) {
               if (m>a[i])
               {
                   m=a[i];
               }




     }
     return m;

}


//
int main () {

int j,l,m=0,period=2000,media_l=100,delta_t;
double dt,Ic,d1,c1,c2,d2,d3,c3,Q,c4,d4,rampa,istart,iend,N,i,v,x,
    T,gamma,N_integrazione,in,soglia_V,i_period,v_period;
double **valori=malloc(3*sizeof(double*));
double *valori2=malloc(media_l*sizeof(double));
for (j=0;j<3;j++){
valori[j]=malloc(period*sizeof(double));

```

```
}
FILE* file2 = fopen("switch.dat", "w");



// CONDIZIONI INIZIALI

FILE* file3 = fopen("parametri.dat", "r");


char s1[7], s2[7], s3[7], s4[7];
char line[50];
while (fgets(line, sizeof line, file3)!=NULL) {
    if (*line == '#') continue; /* ignore comment line */
    else {sscanf(line, "%7s%7s%7s%7s", s1, s2, s3, s4);}


}

Ic=atof(s1);
T=atof(s2);
Q=atof(s3);
delta_t=1;
N_integrazione=atof(s4);
//printf("%lf %lf %lf %lf",Ic,T,Q,N_integrazione);
fclose(file3);
//



//Calcolo dei parametri
gamma=0.083902971508398*(1/Q)*T/Ic; //gamma=2*Gamma_maiusc, per
    la varianza della distribuzione gaussiana
rampa=1/1e+7;
iend=1;
istart=0;
dt=0.1;
rampa=rampa*(iend  istart)/fabs(iend  istart);
N=(iend  istart)/(dt*rampa);
 //numero generato casualmnente per in al tempo t=0
srand(time(NULL));
soglia_V=0.5*Q;
in=sampleNormal()*sqrt(gamma/dt);
//

for(l=0;l<N_integrazione;l++){
x=0;
v=0;
```

```
for(j=0;j<N;j++){
if(j % delta_t==0){
in=sampleNormal()*sqrt(gamma/((double)(delta_t)*dt));}
i=istart+rampa*j*dt;
c1=dt*g1(v);
d1=dt*g2(x,v,Q,i+in);
c2=dt*g1(v+d1/2);
d2=dt*g2(x+c1/2,v+d1/2,Q,i+rampa*0.5*dt+(in));
c3=dt*g1(v+d2/2);
d3=dt*g2(x+c2/2,v+d2/2,Q,i+rampa*0.5*dt+(in));
c4=dt*g1(v+d3);
d4=dt*g2(x+c3,v+d3,Q,i+rampa*dt+in);

x=x+(0.1666666666)*(c1+2*c2+2*c3+c4);
v=v+(0.1666666666)*(d1+2*d2+2*d3+d4);


if(m==period){
i_period=media(valori,period,0);
v_period=media(valori,period,2);
m=0;
if(v_period>soglia_V){fprintf(file2,"\n %d %.8e ",l+1,i_period);
if(l<media_l){valori2[l]=i_period;}
if(l==media_l){istart=min(valori2,media_l) 0.15;}
break;}}


else{
valori[0][m]=i;
valori[1][m]=x;
valori[2][m]=v;
m=m+1;}

}


}



fclose(file2);
return 0;
}
```

Bibliography

[1] B.D Josephson (1962), *Possible new effect in superconductive tunneling*, Physics letters, Vol **1**, number 7.

[2] M. Tinkham (2004),*Introduction to Superconductivity*, Vol.1, Second edition, Dover Books on Physics.

[3] K.Fossheim and A.Sudbø(2004), *Superconductivity:Physics and Applications*, John Wiley & Sons, Inc., United States of America

[4] A. Barone, G. Paternò (1982), *Physics and application of the Josephson effect* John Wiley & Sons, Inc., United States of America

[5] K.K. Likharev (1979), *Superconducting weak links*, Rev. Mod. Phys., Vol **51**, No. 1.

[6] D. Massarotti et al. (2015), *Macroscopic quantum tunnelling in spin filter ferromagnetic Josephson junctions*, Nature Communications **6**, 7376

[7] R.Caruso et al. (2019), *Tuning of Magnetic Activity in Spin-Filter Josephson Junctions Towards Spin-Triplet Transport*, Phy.Rev.Let **122**,047002

[8] Kartik Senapati, Mark G. Blamire and Zoe H. Barber (2011),*Spin-filter Josephson junctions*,Nature Materials, Letters, Macmillan Publisher Limited

[9] Ter T. Heikkilä (2013), *The Physics of Nanoelectronics: Transport and Fluctuation Phenomena at Low Temperatures*, Oxford Master Series in Physics

[10] J.File and R.G. Mills (1963), *Observation of Persistent Current in a Superconducting Solenoid*, Phys. Rev. Lett. **10**, 93

[11] G. Grosso, G. Pastori Parravicini (2014), *Solid State Physics*,Second edition, 2000 Elsevier Ltd.

[12] Dirk van Delft and Peter Kes (2010), *The discovery of superconductivity*, Physics today **38**, Semptember 2010.

[13] N. Ashcroft and D. Mermin N (2003), *Solid State Physics*, Cengage Learning, Inc

[14] V.L. Ginzburg and L.D.Landau (1950), J. Exptl. Theoret. Phys **20**, 1064

[15] M Cyrot,*Ginzburg-Landau theory for superconductors*, Reports on Progress in Physics, Vol **36**, number 2

[16] L.P. Gor'kov (1959), *Microscopic derivation of the Ginzburg-Landau equations in the theory of superconductivity*, Soviet Phys. JETP *9* , 4.

[17] J. Bardeen, L.N. Cooper, and J. R. Schrieffer (1957),*Microscopic theory of Superconductivity*,Phys. Rev. **106**, 162 - 164.

[18] H. Frohlich (1952), *Interaction of electrons with lattice vibrations*, Pro.R.Soc.A, **215**,191

[19] L.N.Copper (1956),*Bound Electron Pairs in a Degenerate Fermi Gas* , Phys. Rev. **104**, 1189

[20] L. D. Landau (1941), *The theory of superfluidity of helium II.* J. Phys. USSR, **5:71**

[21] P. W. Anderson (1963), *Special effects in sperconductivity*, In *Lectures on the Manybody Problem*, Ravello, 1963 (E.R. Caianiello, Ed.) Vol. **2**, academic, 1964 pp.113-115.

[22] P. W. Anderson and J. M. Rowell (1963) *Probable Observation of the Josephson Superconducting Tunneling Effect* Phys. Rev. Lett. **10**, 230

[23] Cohen M.H, L.M Falicon and J.C Phillips (1962), *Superconductive tunneling*, Phys. Rev. Lett. **8**, 316-318

[24] V. Ambegaokar, A. Baratoff (1963), *Tunneling between Superconductors*, Physical Review Letter **10**, 11.

[25] R.P. Feynman et al. , *The Feynman's lectures on physics Addison Wesley*, (1965) Vol. **3**

[26] Rowell J. M. (1963), *Magnetic field dependence of the Josephson tunnel current* Phys.Rev.Letter,**11** ,200-202

[27] R. S. Keizer, S. T. B. Goennenwein, T. M. Klapwijk, G. Miao, G. Xiao, and A. Gupta (2006), *A spin triplet supercurrent through the half-metallic ferromagnet CrO2*, Nature **439**, 825

[28] T. S. Khaire, M. A. Khasawneh, W. P. Pratt, and N. O. Birge (2010),,*Observation of spin-triplet superconductivity in Co-based Josephson junctions.*,Phys. Rev. Lett. **104**, 137002

[29] TJ. W. A. Robinson, J. Witt, and M. Blamire (2010),*Controlled Injection of Spin-Triplet Supercurrents into a Strong Ferromagnet*, Science **329**, 59.

[30] A. F. Andreev (1964), *The termal conductivity of the intermediate state in superconductor* ,Sov. Phys. JETP **19**, 1228 (1964).

[31] Beenakker, C. W. J. (1991), *Universal limit of critical-current fluctuations in mesoscopic Josephson junctions.* Phys. Rev. Lett., **67**, 3836–3839.

[32] P.Dubos 2001, *Josephson critical current in a long mesoscopic SNS junction*, Phys. Rev. B, **63**,064502

[33] R.G.Seed, C.Vittoria, A. Widon 1994, *Excess current in shunted Josephson weak links*, Journal of Applied Physics , **75**, 8195

[34] P. Weiss, *L'hypothèse du champ moléculaire et la propriété ferromagnétique*,J. Phys. Theor. Appl., **6**, 661-690

[35] K.H.J. Bushow, F.R. De Boer (2004), *Physics of Magnetism and Magnetic Materials*, Kluver Academic Publisher, New York.

[36] T.I. Larkin (2012), *Ferromagnetic Josephson switching device with high characteristic voltage*, Applied Physics Letters, **100**, 222601.

[37] Matthias Eschring (2011), *Spin-polarized supercurrents for spintronics*,Phys. Today **64**,63

[38] Jian-Xin Zhu (2016), *Bogoliubov-de Gennes Method and its Applications*, Springer Volume **924**

[39] P. Fulde, R. A. Ferrell, *Superconductivity in a Strong Spin-Exchange Field*,Phys. Rev. **135**, A550 (1964);

[40] A. I. Larkin, Y. N., *Nonuniform State of Superconductors*, Ovchinnikov, Sov. Phys. JETP **20**, 762 (1965).

[41] V. V. Ryazanov et al.(2001),*Coupling of Two Superconductors through a Ferromagnet: Evidence for a π Junction*, Phys. Rev. Lett. **86**, 2427

[42] T. Kontos et al., *Josephson Junction through a Thin Ferromagnetic Layer: Negative Coupling*, Phys. Rev. Lett. **89**, 137007 (2002)

[43] D. Massarotti et al. (2016), *Low temperature properties of spin filter NbN/GdN/NbN Josephson junctions*, Physica C. Superconductivity and its applications, 000, 1-6.

[44] R. Meservey and P.M. Tedrow (1994), *Spin-polarized electron tunneling.* Phys. Rep. **238**, 173–243

[45] F. Sebastian Bergeret, Alvise Verso and Anatoly F. Volkov (2012), *Spin-polarized Josephson and quasiparticle currents in superconducting spin-filter tunnel junctions*, Phy.Rev. B **86**, 060506(R)

[46] Devoret et. al (1984), *Resonant Activation from the Zero-Voltage State of a Current-Biased Josephson Junction*,Phys. Rev. Lett., Vol **53**, 13

[47] Giaever I. and K. Mergerle (1961), *Study of superconductors by electron tunneling*,Phys.Rev.Letter,**122**, 1101-1111

[48] Johnson W.J. (1968), *Nonlinear wave propagation on superconducting tunneling junctions*, Ph.D Thesis, Unversity of Wisconsin, Madison

[49] W.C. Stewart (1968), *current-voltage characterristics of josephson junctions*, Appl. Phys. Lett. **12**, 277 (1968)

[50] Zappe H.H. (1973),*Minimum current and related topics in Josephson tunnel junction devices*, Appl.Phys.Lett., **44**,1371-1377

[51] Schlup W.(1974),*I-V characteristics and stationary dynamics of a Josephson junction including the interference term in the current phase relation*, J.Phys.C.Solid State Phys., **7**,736-748

[52] J.Clarke and F. K.Wilhelm (2008), *Superconducting quantum bits*, Nat. Vol **453**, 1031-1042

[53] D. Massarotti (2013), *Macroscopic quantum phenomena in superconductors: study of phase dynamics and dissipation in moderately damped Josephson junctions*, Doctoral dissertation

[54] V. Ambegaorkar and B Halperin (1969), *Voltage due to thermal noise in the dc Josephson effect*, Phy. Rev. Let. **22**, 25

[55] R. L. Kautz and J. M. Martinis (1990), *Noise-affected I V curves in small hysteretic Josephson junctions,* Phys. Rev. B **42**, 9903 ;

[56] P.M.Chaikin (2012), *Principles of Condensed Matter Physics*, Cambridge University Press

[57] D.J. Scalapino (1967), *Current fluctuation in superconducting tunnel junction*, SPSD, G1 -G19

[58] Luigi Longobardi et al. (2011), *Thermal hopping and retrapping of a Brownian particle in the tilted periodic potential of a NbN/MgO/NbN Josephson junction*, Phys. Rev. B **84**, 184504

[59] H.A.Kramers (1940), *Brownian motion in a field of force and the diffusion model of chemical reactions*, Physica vol. **7**, Issue 4.

[60] Krasnov, T. Golod, T. Bauch, and P. Delsing (2007),*Anticorrelation between temperature and fluctuations of the switching current in moderately damped Josephson junctions* ,Phys. Rev. B, **76**, 224517

[61] E. Ben-Jacob et al., *Lifetime of oscillatory steady states*, Phys.Rev.A **26**,2805

[62] J.C.Fenton and P.A. Warburton, *Monte Carlo simulations of thermal fluctuations in moderately damped Josephson junctions:Multiple escape and retrapping, switching- and return-current distributions, and hysteresis*, Phy. Rev. B, **78**, 0542526

[63] J. T. Anderson and A. M. Goldman (1969), *Thermal fluctuations and the josephson supercurrent*, Phy.Rev.Let. vol **23**, 3

[64] M. Simmonds and W. H. Parkerg (1970), *Thermal fluctuations in superconducting weak links*, Phy.Rev.Let. vol **24**, 16

[65] Franz et al. (2004) , *Thermal fluctuations in ultrasmall intrinsic Josephson junctions*,Phy.Rev.B **69**, 014506

[66] *WKB Approximation Applied to Tunneling* (2006), `https://ocw.mit.edu/courses/electrical-engineering-and-computer-science/6-728-applied-quantum-and-statistical-physics-fall-2006/study-materials/wkb_tunneling2.pdf`

[67] A.O.Caldeira and A.J.Leggett(1983),*Quantum tunnelling in a dissipative system*,Annals of Physics **149**,2

[68] M.Martinis, H.Devoret and J.Clarke (1987), *Experimental tests for the quantum behaviour of a mascroscopic degree of freedom: The phase difference across a Josephson junction*, Phy.Rev.B vol. **35**, 10

[69] L.J. van der Pauw (1958),*A method of measuring specific resistivity and Hall effect of discs of arbitrary shape*, Philips Research Reports, **13**.

[70] ©Copyright Agilent Technologies (2002) - *Agilent 33120A,15MHz Function, Arbitrary Waveform Generator, Agilent User's guide*, Publication Number 33120-90006.

[71] ©R Keithley: A techtronik Company -*Source meter SMU instruments:Series 2400.*

[72] ©Ametek advanced measurements technology, Inc (2002)-*Model 5210 Dual Phase Lock-in Amplifier, Instruction Manual*

[73] F. Leuenberger, A. Parge W. Felsch,1 K. Fauth, and M. Hessler (2005), *GdN thin films: Bulk and local electronic and magnetic properties*,Phys.Rev.B **72**,014427

[74] A. Pal , K. Senapati , Z.H. Barber , M.G. Blamire (2013), *Electric field dependent spin polarization in GdN spin filter tunnel junctions*, Adv. Mater. **25**, 5581–5585

[75] John R. Taylor (1999), *Introduzione all'analisi degli errori. Lo studio delle incertezze nelle misure fisiche*, Zanichelli

[76] G.Rotoli et al. (2007) *Clssical resonant activation of a Josephson junction embedded in an LC circuit*,Phys. Rev.B **75**, 144501

[77] Tao Pang (2006), *An introduction to computational physics*, Cambridge University Press

[78] , C. Bonnelle, N. Spector (2015), *Rare-Earths and Actinides in High Energy Spectroscopy* , Springer, Science+Business Media Dordrecht.

[79] J. Männik et al. (2005), *Crossover from Kramers to phase-diffusion switching in moderately damped Josephson junctions*, Phy. Rev B **71**, 220509R

[80] R.H.Ono et al. (1987), *Current-voltgae characteristics of nanoampere Josephson junction*, IEEE Transactions on Magnetics, Vol. **23**

[81] D. Stornaiuolo et al. (2013), *Resolving the effects of frequency-dependent damping and quantum phase diffusion in* $YBa_2Cu_3O_{7-x}$ *Josephson junctions*,Phy, Rev. B **87**, 134517

[82] R.H.Landau et al. (2012), *Computational physics*, pp. 178-190